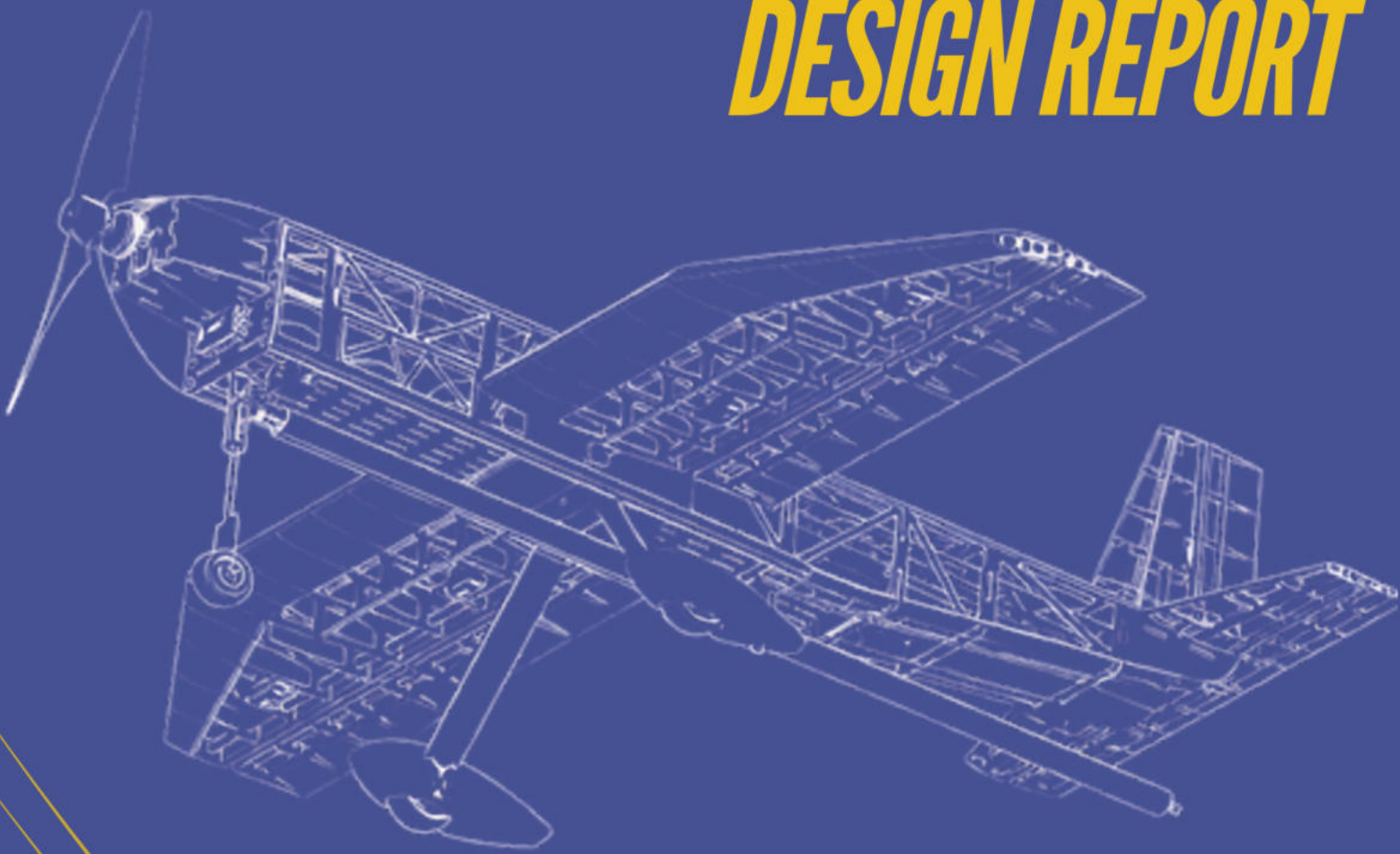


# PUSHPAK

**AIAA DBF 2025 - 2026  
DESIGN REPORT**



Indian Institute of  
Technology Kharagpur



**Table of Contents**

	Page No.
<b>1. Executive Summary.....</b>	<b>4</b>
<b>2. Management Summary.....</b>	<b>5</b>
2.1 Team Organization.....	5
2.2 Milestones.....	6
<b>3. Conceptual Design.....</b>	<b>7</b>
3.1 Mission Requirements.....	7
3.2 Scoring Sensitivity.....	9
3.3 Subsystems Requirements.....	11
3.4 Configuration Selection.....	13
3.5 Final Conceptual Design.....	16
<b>4. Preliminary Design.....</b>	<b>16</b>
4.1 Design Methodology.....	16
4.2 Design Trade Studies.....	17
4.3 Aerodynamics.....	20
4.4 Stability and Control.....	26
4.5 CFD Analysis.....	28
4.6 Estimated Aircraft Mission Performance.....	30
<b>5. Detailed Design.....</b>	<b>31</b>
5.1 Dimensional Parameters.....	31
5.2 Structural Characteristics.....	32
5.3 System and Subsystem Design Implications.....	32
5.4 Weight and Mass Balance.....	42
5.5 Performance.....	43
5.6 Drawing Package.....	44
<b>6. Manufacturing Plan.....</b>	<b>49</b>
6.1 Available Manufacturing Processes.....	49
6.2 Composite Material Selection.....	50
6.3 Selected Manufacturing Processes.....	51
6.4 Manufacturing Timeline.....	52
<b>7. Testing Plan.....</b>	<b>53</b>
7.1 Banner Drag - Wind Tunnel Testing.....	53
7.2 Banner Deployment and Release Mechanism Feasibility.....	54
7.3 Propulsion System Testing.....	55
7.4 Wing and Fuselage Structural Testing.....	55
7.5 Checklist.....	56
<b>8. Performance Results.....</b>	<b>57</b>
8.1 Aerodynamics of Banner.....	57
8.2 Banner Deployment and Feasibility Tests.....	57
8.3 Propulsion System.....	58
8.4 Structural Testing.....	59
<b>9. Bibliography.....</b>	<b>60</b>

## Abbreviations, Acronyms and Symbols

<b>A</b>	Fixed Score Component (Mission 2 metric)	<b>PLA</b>	Polylactic Acid
<b>AIAA</b>	American Institute of Aeronautics and Astronautics	<b>PVC</b>	Polyvinyl Chloride
<b>AR</b>	Aspect Ratio	<b>Q</b>	Interference Factor
<b>ARK</b>	Aerial Robotics Kharagpur	<b>q</b>	Dynamic Pressure
<b>AVL</b>	Athena Vortex Lattice	<b>RAC</b>	RatedAirplane Cost
<b>B</b>	Marginal Per-Lap Reward (Mission 2 metric)	<b>R/C</b>	Radio-Controlled / Rate of Climb
<b>b</b>	Wingspan	<b>RPM</b>	Revolutions Per Minute
<b>BEC</b>	Battery Eliminator Circuit	<b>Rx</b>	Receiver
<b>BLDC</b>	Brushless Direct Current Motor	<b>S</b>	Planform Area (Wing by default)
<b>C</b>	Coefficient	<b>T</b>	Thrust (by default) / Required Torque
<b>c</b>	Chord Length	<b>W</b>	Weight
<b>CA</b>	Cyanoacrylate	<b>V</b>	Velocity (by default) / Volume Coefficient
<b>CAD</b>	Computer-Aided Design	<b>x</b>	Location
<b>CF</b>	Carbon Fiber	<b>α</b>	Angleof Attack
<b>CFD</b>	Computational Fluid Dynamics	<b>β</b>	Sideslip Angle
<b>CG</b>	Center of Gravity	<b>δ</b>	Deflection Angle
<b>CNC</b>	Computer Numerical Control	<b>η</b>	TaperStart Location / Efficiency
<b>COTS</b>	Commercial-Off-The-Shelf	<b>λ</b>	TaperRatio
<b>D</b>	Drag Force	<b>μ</b>	Dynamic Viscosity
<b>d</b>	Number of ducks	<b>ρ</b>	AirDensity (Sea Level)
<b>DBF</b>	Design, Build, Fly	<b>ζ</b>	Damping Ratio
<b>e</b>	Oswald/Span Efficiency Factor	<b>ω</b>	Frequency of the System
<b>EF</b>	Efficiency Factor		
<b>ESC</b>	Electronic Speed Controller		
<b>FAAAC</b>	Federal Aviation Administration Advisory Circular		
<b>FEA</b>	Finite Element Analysis		
<b>FF</b>	Form Factor		
<b>FoS</b>	Factor of Safety		
<b>FRP</b>	Fiber-Reinforced Polymer		
<b>g</b>	Acceleration due to gravity		
<b>GM</b>	Ground Mission		
<b>GPS</b>	Global Positioning System		
<b>H</b>	Aerodynamic Hinge Moment		
<b>IIT</b>	Indian Institute of Technology Kharagpur		
<b>KV</b>	Motor Velocity Constant (RPM per Volt)		
<b>L</b>	Lift		
<b>I</b>	length		
<b>LiPo</b>	Lithium Polymer		
<b>Li+</b>	Lithium-Ion		
<b>M1</b>	Mission 1		
<b>M2</b>	Mission 2		
<b>M3</b>	Mission 3		
<b>MAC</b>	Mean Aerodynamic Chord		
<b>MTOW</b>	Maximum Take-Off Weight		
<b>N</b>	Net Income		
<b>n</b>	Number of Laps/Propeller Rotational Speed/Structural Load Factor (context-based)		
<b>NiCAD</b>	Nickel-Cadmium Battery		
<b>NiMH</b>	Nickel-Metal Hydride Battery		
<b>NP</b>	Neutral Point		
<b>OML</b>	Outer Mold Line		
<b>p</b>	Number of pucks		
<b>PETG</b>	Polyethylene Terephthalate Glycol		

### Subscripts:

<b>0</b>	Zero-Lift
<b>a</b>	Aileron
<b>arm</b>	Arm
<b>c</b>	Control Surface
<b>cg</b>	Center of Gravity
<b>cruise</b>	Cruise Condition
<b>D</b>	Drag
<b>e</b>	Elevator
<b>f</b>	Fuselage / Skin Friction
<b>H</b>	Horizontal Tail
<b>h</b>	HingeMoment
<b>horn</b>	Horn
<b>i</b>	Induced
<b>L</b>	Lift
<b>linkage</b>	Linkage
<b>m</b>	Pitching Moment
<b>max</b>	Maximum
<b>n</b>	Natural
<b>np</b>	Neutral Point
<b>p</b>	Pressure
<b>r</b>	Rudder
<b>ref</b>	Reference
<b>stall</b>	Stall
<b>T</b>	Thrust
<b>t</b>	tail
<b>tr</b>	FlowTransition
<b>turn</b>	Turn
<b>V</b>	VerticalTail
<b>Y</b>	Side-force derivative
<b>α</b>	Longitudinal
<b>β</b>	Directional
<b>δ</b>	ControlDeflection

## 1. Executive Summary

This report presents Pushpak, Team IIT Kharagpur's aircraft developed for the 2026 American Institute of Aeronautics and Astronautics (AIAA) Design, Build, Fly (DBF) competition. The objective this year is to design, build, and flight-test an electric, radio-controlled banner-towing bush plane, capable of completing three flight missions and one ground mission while satisfying the specified safety, payload, and operational constraints. Mission 1 is a no-payload test flight requiring the aircraft to complete three laps within the allotted flight window. Mission 2 requires a charter flight that evaluates the aircraft's ability to transport passenger ducks and cargo pucks in a manner that maximizes net operational income during the mission time. In Mission 3, the plane is required to deploy, tow, and release an externally stowed banner in flight while maintaining competitive lap performance. During the Ground Mission, the crew must rapidly configure the aircraft for M2, then for M3 in the minimum time possible in a parking space of 10 ft x 10 ft. All this was achieved with the combined efforts of all the 10 subsystems under the lead of the Project Manager and the Chief Engineer, and the insightful advises by the academic and industrial advisors.

The Pushpak (see Figure 1.1) is a mid-wing monoplane with tricycle landing gear and conventional tail configuration powered by a single powerful nose propeller to meet the endurance goals. The conventional tail optimizes stability and manoeuvrability. The wing shape is selected for reducing drag while generating sufficient lift to carry high payload in M2, and also sustain high wing loading during turns. The scoring and sensitivity analysis was very vital to find the various design parameters of the aircraft, such as the dimensions, flight velocity, battery capacity, passenger and cargo carrying capacity, etc. This analysis are expected to lead to competitive scores in each mission.

Pushpak has a semi-tapered wing of wingspan 5 ft and mean aerodynamic chord of 13.71 in. The wing is capable of producing 17.05 lb of lift at take-off and 17.63 lb in cruise. The fuselage cross-sectional area is almost square in shape to maximize the payload capacity inside the fuselage, and also allowing for double-deck interior. The tail stabilizes the aircraft with an optimized moment arm of 37.40 in. and the horizontal and vertical stabilizers have areas of 186.70 sq.in. and 80.85 sq.in respectively. The carbon fibre based landing gear provides a safe landing on the roughest grounds. The large nose propeller generates enough thrust to accelerate the heavy aircraft to competitive velocities. To bear the aerodynamic loading at high velocities, the wing's leading edge is reinforced with 0.06 in. thick balsa and designed with strong carbon-fibre spars. The fuselage bulkheads are made using birchply to bear the distributed impact on landing and the skin of the aircraft is made out of Monocote. The team has already developed strict manufacturing and testing plans for the perfect outcome of Pushpak's engineering. The Pushpak V1 prototype is shown in Figure 1.1 and its performance capabilities are shown in Table 1.1.

**Table 1.1:** Pushpak Performance Capabilities

Parameter	Value
Empty Weight	8.88 lb
Maximum Take-Off Weight (MTOW)	14.00 lb
Mission 2 Top Speed	53 mph
Mission 3 Top Speed	37 mph
Number of Passengers (Rubber Ducks)	30
Number of Cargo (Hockey Pucks)	10
Banner Length (Mission 3)	17.33 ft
Thrust-to-Weight Ratio (Mission 2)	1.13
Thrust-to-Weight Ratio (Mission 3)	1.49



**Figure 1.1:** Pushpak V1

## 2. Management Summary

### 2.1 Team Organization

The team operates under the guidance of academic and industry advisors who provide technical direction, design feedback, and oversight throughout the competition cycle. Direct leadership of the project is shared between the Chief Engineer and the Project Manager in a co-lead structure, which is shown in Figure 2.1.

The team of 21 members is led by two executives. The Chief Engineer is responsible for overall technical authority, including aircraft configuration decisions, multidisciplinary design integration, and verification of subsystem compatibility across design, manufacturing, and testing phases. The Project Manager oversees team administration, schedule development and tracking, documentation coordination, operational planning, and flight-test execution, while also serving as the primary pilot for competition activities. Together, these roles ensure alignment between technical progress and programmatic milestones.

Beneath executive leadership, the team is organized into specialized functional sub-teams, each responsible for a critical aspect of aircraft development. The Aerodynamics team performs wing sizing, aerodynamic analysis, and overall performance prediction. The Propulsion team selects and integrates the motor, propeller, battery, and associated power system components. The Structures team designs the airframe and evaluates structural integrity under expected loading conditions. The Stability and Control team sizes the tail surfaces and ensures adequate controllability and flight stability across all mission profiles.

The Computer-Aided Design (CAD) team generates detailed digital models and engineering drawings that support analysis, manufacturing, and system integration. The Manufacturing team determines fabrication methods, produces aircraft components, and manages final assembly. The Composites team develops and fabricates composite structures to achieve the required strength-to-weight performance. The Banner subsystem team designs and integrates the banner deployment and release mechanism required for Mission 3. The Payload subsystem team develops passenger and payload accommodation systems in accordance with competition constraints. Finally, the Configuration Analysis team evaluates overall aircraft layout, performs trade studies, and ensures consistency between subsystem requirements and the final integrated design.

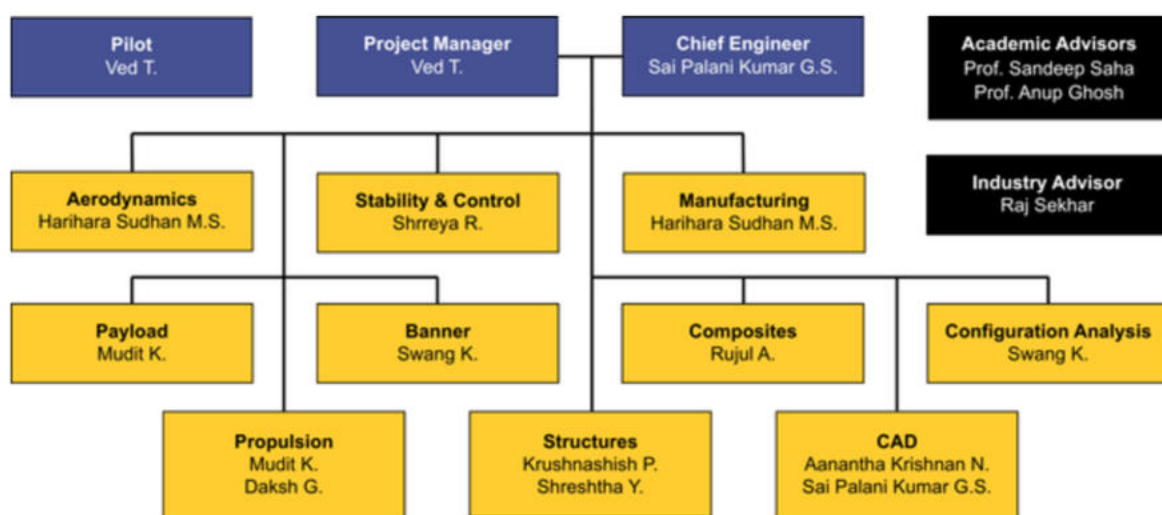


Figure 2.1: Pushpak Team Organization Chart

This collaborative structure enables clear responsibility ownership, efficient communication between disciplines, and coordinated progress toward a flight-ready competition aircraft.

## 2.2 Milestones

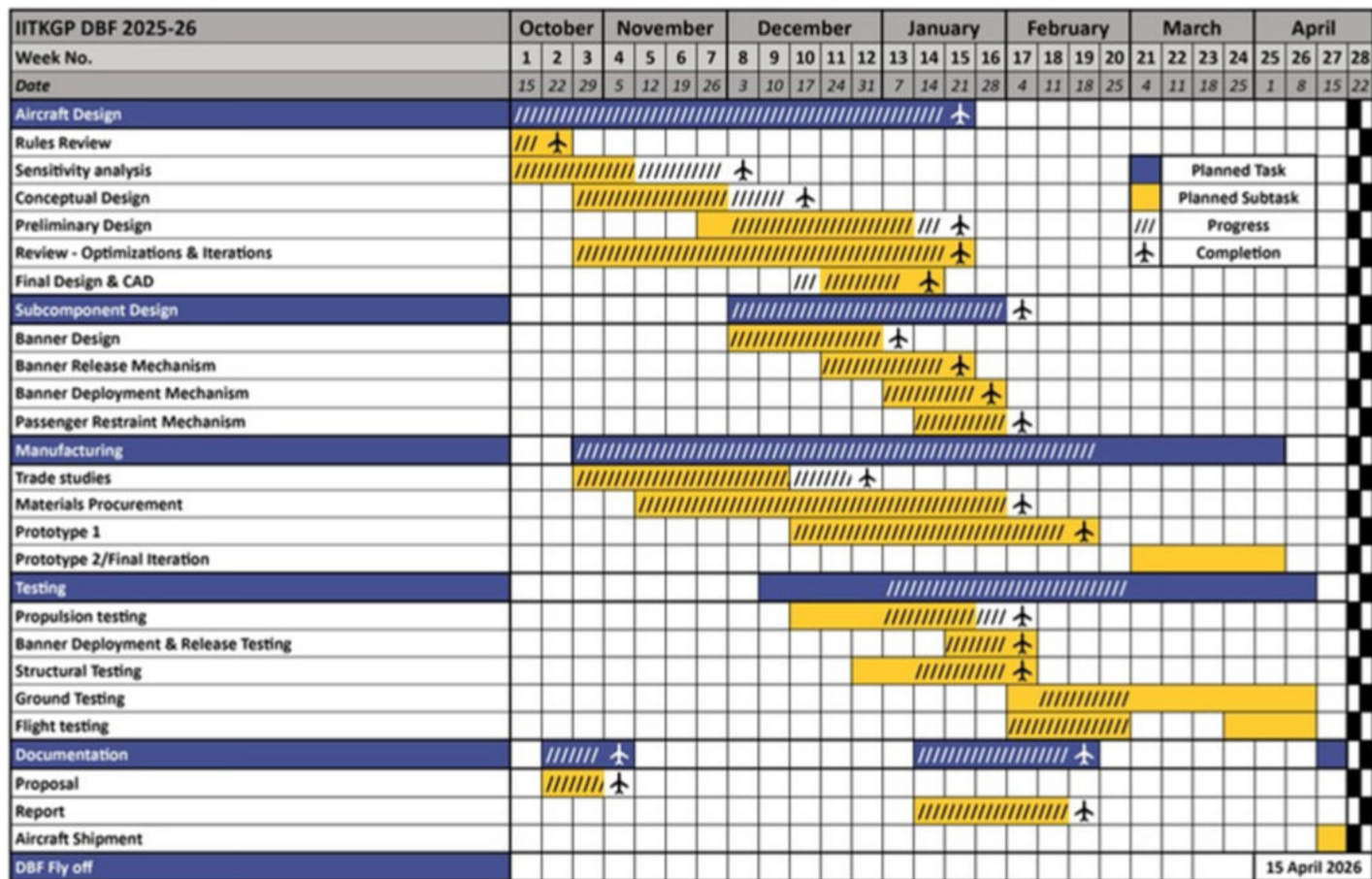
A detailed project schedule was established at the beginning of the design cycle to coordinate analysis, manufacturing, and testing activities, as illustrated in Figure 2.1. The Gantt chart outlines progression through conceptual, preliminary, and detailed design phases, followed by prototype fabrication, subsystem validation, and integrated flight testing, while tracking major review milestones and report deliverables.

The development approach is based on a two-prototype build sequence to incrementally mature the aircraft configuration and reduce technical risk. The first prototype has completed fabrication and is currently in the flight-testing phase, where aerodynamic performance, stability characteristics, propulsion integration, and payload functionality are being evaluated. Test results from this stage guide configuration refinements and structural updates for subsequent builds.

The second prototype is scheduled for near-term construction and will incorporate improvements identified during initial testing, serving as the primary platform for verification of repeatable flight performance and mission-relevant functionality. The final competition aircraft, produced as the third prototype, is planned to begin manufacturing in the second week of March and will integrate validated geometry, finalized structures, and fully qualified subsystems for system-level testing and flight-readiness verification.

Continuous schedule updates and parallel subsystem development maintain alignment between technical progress and program milestones.

**Table 2.1: Timeline and Milestones Chart**



### 3. Conceptual Design

In the conceptual design phase, the team began with a detailed study of the 2025-2026 Design-Build-Fly (DBF) rules, focusing on mission scoring equations and governing constraints. These rules formed the basis for identifying key performance drivers. Through scoring sensitivity analyses and configuration-level trade studies, constraint-driven trends were identified. Based on these insights, a conceptual configuration was selected and is summarised in Section 3.5.

#### 3.1 Mission Requirements

The rules for the 2025-2026 American Institute of Aeronautics and Astronautics (AIAA) Design-Build-Fly (DBF) competition simulate the design of an electrically powered, propeller-driven banner-towing bush aircraft capable of carrying passengers and cargo. The aircraft must complete three flight missions and one ground mission under geometric, propulsion, and operational constraints. This section summarizes the mission objectives, scoring logic, and governing constraints that define the conceptual design space.

##### 3.1.1 Staging

The aircraft must already be in its final staging configuration when it enters the staging area without the batteries, payload and arming fuse. Teams have five minutes to assemble the aircraft for the subsequent flight mission, install batteries and payloads, and check flight control. No configuration changes or repositioning of the aircraft is allowed. The aircraft must be upright and on its landing gear during assembly, payload installation and flight controls checks. After the staging time expires, no further changes are allowed except installation of the arming fuse and final checks before takeoff. The flight attempt is forfeited if staging is not finished in the allocated time.

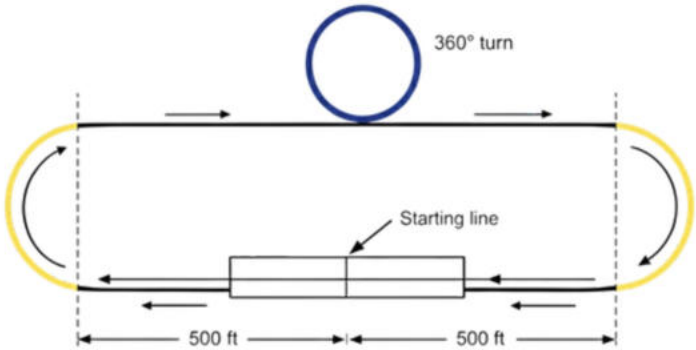


**Figure 3.1:** Competition Lap

##### 3.1.2 Flight Course

A full competition lap consists of two 1000 ft straights connected by an upwind and downwind turn along with a 360 degree turn as outlined in Figure 3.1. The completion of a lap is defined by crossing the finish line, either airborne or on the ground. A successful landing is required to receive a mission completion score.

##### 3.1.3 Test Flight (M1)

In the first of the four missions, this mission tests the plane's airworthiness. In this mission, the plane is to be flown unloaded (no passengers, cargo, or banner). The scoring is done in a binary fashion, and for a full point, the aircraft must complete three laps within a 5-minute flight time window. A successful mission requires completion of the 3 laps along with a safe landing on the runway.

$$M1 = 1.0 \text{ (for successful completion)}$$

##### 3.1.4 Charter Flight (M2)

In the second of the four missions the aircraft must carry passengers and cargo (rubber ducks and hockey pucks) in this mission. The score is a combined function of parameters like number of passengers and cargo, number of laps

laps flown in a time window of 5 minutes and the propulsion battery capacity. The scoring matrix is as below:

$$M2 = 1 + \frac{N_{NetIncome}}{\text{Max Net Income}} \quad \text{--- Equation 3.1}$$

$$\begin{aligned} \text{Income} &= (\# \text{passengers} \times (6 + 6 \# \text{laps})) + (\# \text{cargo} \times (10 + 8 \# \text{laps})) \\ \text{Cost} &= \# \text{laps} \times (10 + (0.5 \times 0.5) + (\# \text{cargo} \times 2)) \times \text{EF} \end{aligned} \quad \text{--- Equation 3.2(a) \& 3.2(b)}$$

Mission 2 rewards payload throughout the time window while penalizing excessive energy storage through the efficiency factor (EF). This creates a coupled tradeoff between payload mass, achievable lap count, and propulsion efficiency, which is explored quantitatively in the sensitivity analysis as scoring weightage of both are compared.

### 3.1.5 Banner Flight - Mission 3

The penultimate mission involves towing a banner, and as a consequence, the total drag is increased which depletes the excess thrust margin, limiting the aircraft's performance. The scoring matrix is as mentioned below:

$$M3 = 2 + \frac{N_{(\# \text{laps} \times \text{Banner Length} / \text{RAC})}}{\max(\# \text{laps} \times \text{Banner Length} / \text{RAC})} \quad \text{--- Equation 3.3}$$

**RAC** = Rated Airplane Cost, which is penalty on increased wingspan

$$\text{RAC} = 0.05 \times \text{Wingspan (ft)} + 0.75 \quad \text{--- Equation 3.4}$$

The score is based on the number of laps completed with the banner deployed, banner length and RAC, which is normalized with the best team score. From the formula, the scheme rewards lap completion over high speed, emphasizing endurance under high drag rather than peak thrust, this impose constraints on propulsion sizing, tail sizing and controllability, which are evaluated through configuration selection and guides the conceptual design.

### 3.1.6 Ground Mission (GM)

In this ground mission which may be done anytime throughout the competition it tests the aircraft's ability to rapidly transition between mission configurations. This includes payload loading, unloading, and banner stowage, deployment and release. The scoring formula is as below:

$$GM = \frac{\min(\text{Mission Time})}{\text{Team Mission Time}} \quad \text{--- Equation 3.5}$$

where, Team Mission Time = total time taken by the team to complete the ground mission sequence

$\min(\text{Mission Time})$  = shortest mission time achieved among all teams

From a conceptual design perspective GM score is based on payload bay accessibility, requiring quick and unobstructed access to passenger and cargo compartments, along with simple restraint mechanisms that are secure yet fast to operate and efficient banner stowage, deployment, and release systems with minimal assembly steps.

### 3.1.7 Scoring Summary

Each team's overall score will be computed from their Total Report Score, Total Mission Score, using the following equation below.

$$\text{Total Report Score} = 0.15 \times \text{Proposal Score} + 0.85 \times \text{Design Report Score} \quad \text{--- Equation 3.6}$$

The total mission score is given below:

$$\text{Total Mission Score} = M1 + M2 + M3 + GM \quad \text{--- Equation 3.7}$$

### 3.2 Scoring Sensitivity

Optimal aircraft design selection requires some basic guidelines regarding design parameters. Based on the requirements for each mission discussed in 3.1. Relationship between design parameters, can all be mathematically described and is done in the below subsection.

#### 3.2.1 Sensitivity Analysis for M2

The Mission 2 scoring formulation can be decomposed for interpretive analysis as:

$$\text{Score} = A + B \cdot n \quad \text{--- Equation 3.8}$$

Within this model,  $n$  was defined as the number of laps, while  $d$  and  $p$  represented the counts of ducks and pucks, respectively. The total score was derived from a Fixed Score Component,  $A$  (calculated as  $6*d + 10*p$ ), and a Marginal Per-Lap Reward,  $B$  (expressed as  $d*(2 - 0.5*EF) + p*(8 - 2*EF) - 10$ ), which incorporated the efficiency factor (EF) to determine the variable reward per lap.

The gradient topology in Figure 3.2 confirms that score maximization is heavily payload-dependent, as the coefficient  $B$  scales aggressively with payload mass.

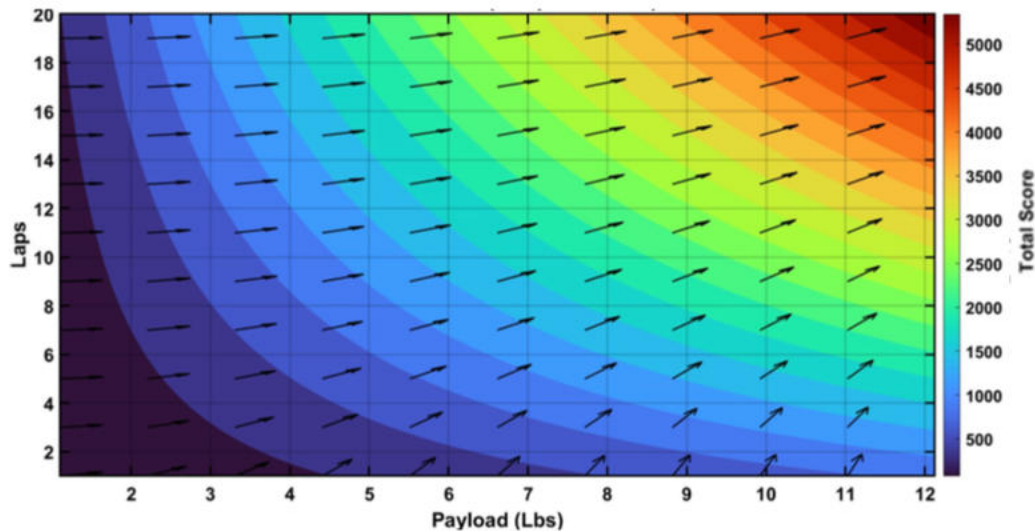


**Figure 3.2:** Mission 2 Score Gradient: Influence of Payload and Lap Count

Crucially, the analysis identified that the mandated 3:1 Passenger-to-Cargo ratio (ducks  $\geq$  3 pucks) acts as a dominant driver and maximizing this specific ratio leads to the high fixed income of passengers. The trade-off mathematics identified a non-linear penalty: a reduction in payload mass requires a disproportionately large increase in achievable lap count to maintain score parity, which rapidly becomes infeasible within the fixed 5-minute mission window. To quantify this trade-off, the scoring formulation was evaluated across the feasible ranges of payload mass and completed lap count within the fixed mission window. Mapping score as a function of payload and laps allowed the non-linear interaction between these parameters to be visualized directly. This representation highlighted how payload growth increased score within each lap tier, while discrete lap transitions introduced sharp performance discontinuities. The resulting sensitivity topology is presented on the following page and formed the basis for selecting the Mission 2 design point.

To operationalize this high-payload strategy, the performance heatmap overlaid the scoring topology with the aircraft's 5-minute power-speed feasibility boundary. An energy budget analysis was conducted considering available battery capacity and efficiency factor penalties. Initial sizing considered a 4500 mAh 6S battery; however, scoring sensitivity showed that the efficiency factor penalized larger battery capacities. Subsequent analysis demonstrated that the aircraft could complete the required 6 laps with a 3800 mAh 6S battery while achieving a slightly higher net score due to improved efficiency factor.

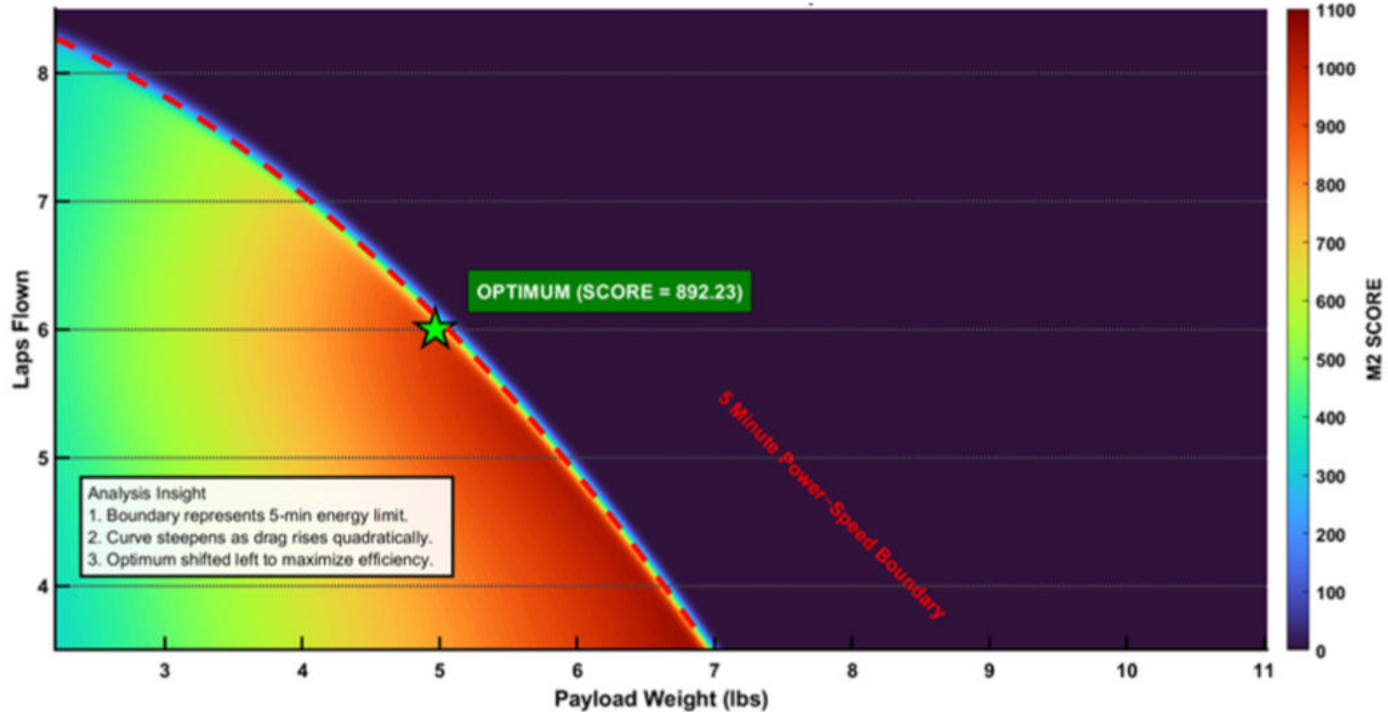


**Figure 3.3:** Mission 2 Performance Heatmap with 5-Minute Power-Speed Feasibility Boundary

The interpretation of the scoring sensitivity was that carrying maximum payload on 5 laps scored significantly higher than completing 6 laps with minimum payload. This pattern revealed that prioritizing payload mass over lap count was preferable to a high-speed, low-payload profile. The grey region represented theoretical scores achievable with unlimited power, but the actual performance (Blue Ridge) was limited by aerodynamic drag. As payload increased, the score climbed linearly within each lap tier, observed along the 6-lap ridge because heavier payloads directly increased the scoring coefficient ( $A$ ).

**Table 3.1:** Mission 2 Performance Estimate at the Selected Operating Point

Quantity	Estimation
Cruise Speed	53 mph
Lap Length	3000 ft
Lap Time	40 - 50 s
Max Laps	6
Net Weight of aircraft	9.36 lbs
EF	0.843
Net Income	892.23

However, this steady increase hits Performance Discontinuities (Red Drops) at critical weight thresholds. As the aircraft nears the 4.96 lb limit, induced drag ( $D \propto W^2$ ) consumes all available propulsive power. Pushing beyond this threshold triggers a regime change: the aircraft no longer has enough thrust-to-weight ratio to maintain the speed needed for 6 laps, causing an immediate drop to the 5-lap tier.

### 3.2.2 Sensitivity Analysis for M3

Mission 3 scoring was governed by the coupled interaction between banner length and completed lap count within the fixed 5-minute mission window. The scoring sensitivity analysis was carried out using the complete official Mission 3 scoring formulation to determine the optimal banner length. The optimisation was implemented in MATLAB using aircraft performance constraints including an estimated static thrust of 15.7 lbf, wing area of 6.1 ft<sup>2</sup>, aircraft weight of 11 lb, a conservative banner drag coefficient of  $C_d = 0.03$  from literature [1], and a representative wind speed of 19 mph.

As banner length increased, the score initially increased due to the direct proportionality between score and banner size. However, the additional drag reduced aircraft cruise speed under the available fixed thrust. Since lap count was discretised, small reductions in speed caused abrupt losses of entire laps, producing the step-like drops visible in Figure 3.4. This behaviour demonstrated the over-constrained nature of Mission 3 performance. The results identified a banner length of approximately 17.33 ft as the optimal configuration, corresponding to 4 completed laps and the maximum achievable mission score under the assumed conditions. Increasing the banner length beyond this point produced a net score reduction due to lap loss despite the larger banner size.

**Table 3.2: Mission 3 Optimised Banner Configuration and Estimated Score**

Parameter	Value
Banner Length	17.33 ft
Banner Aspect Ratio	5:1
Cruise Airspeed	37 mph
Laps Completed (5 min)	4
Rated Aircraft Cost (RAC)	1
Estimated Mission 3 Score	68

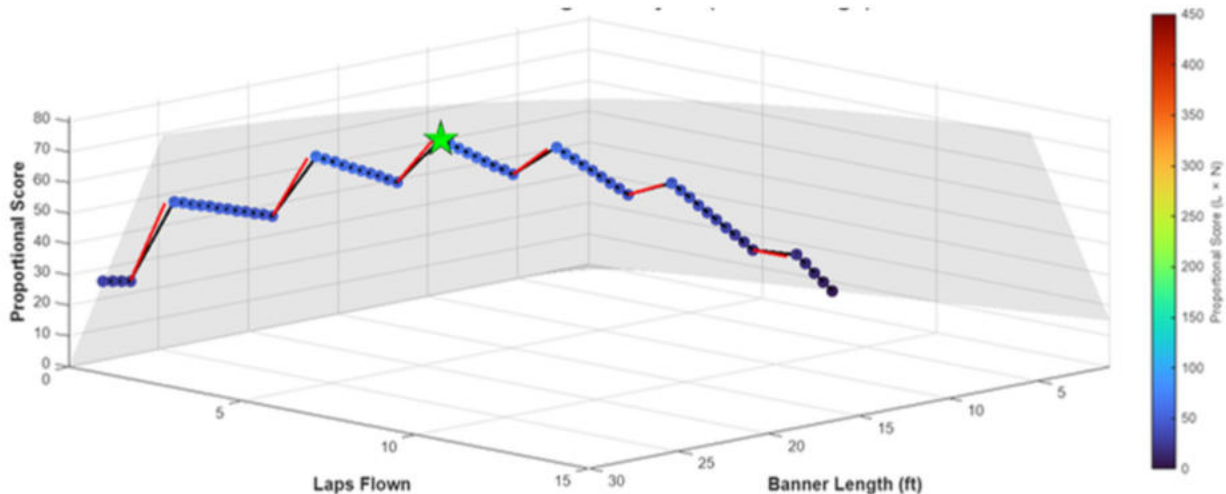


**Figure 3.4: Mission 3 Scoring Sensitivity - Banner Length Optimisation**

### 3.3 Subsystem Requirements

The mission objectives and competition constraints defined in Section 3.1 were translated into subsystem-level requirements to guide the conceptual design process. This mapping enables objective evaluation of aerodynamic, structural, propulsion, and integration choices while ensuring that all major subsystems contribute directly to mission performance and rule compliance.

**Table 3.3: Mission Requirements and Constraints**

Component	Label	Requirement
General Requirements	<b>GR.1</b>	The airplane's wingspan must be less than or equal to 5 feet
	<b>GR.2</b>	The minimum allowable RAC=0.9(RAC=0.05*WS+0.75)
	<b>GR.3</b>	The loaded and empty CG locations must be marked on the exterior of the airplane.
	<b>GR.4</b>	The airplane TOGW (take-off gross weight with payload) must be less than 55-lbs.
	<b>GR.5</b>	The aircraft must be propeller-driven and powered by a standard, unmodified, commercially available brushed or brushless electric motor.
	<b>GR.6</b>	The airplane must be manually flown using radio control. Autopilots, flight controllers, and onboard GPS are prohibited, but stabilization systems and rate gyros are allowed.
	<b>GR.7</b>	The radio-control transmitter and receiver must be commercially available, fail-safe capable, and operate on approved US frequencies (72 MHz, 900 MHz, or 2.4 GHz).
	<b>GR.8</b>	A successful landing is required to receive a score.
	<b>GR.9</b>	No form of externally assisted take-off is allowed. All energy for take-off must come from the on-board propulsion battery pack(s).
	<b>GR.10</b>	Aircraft shall maintain acceptable longitudinal and lateral stability across all payload and banner configurations
Mission 1	<b>M1.1</b>	The team must complete 3 laps within the 5 minute flight window.
Mission 2	<b>M2.1</b>	Aircraft must carry greater or equal than three passengers (rubber ducks) and one cargo (standard hockey puck).
	<b>M2.2</b>	Passengers must be accommodated within a single cabin compartment and cannot be fully isolated (or enclosed) from one another, located on one plane that remains parallel to the horizontal plane during flight.
	<b>M2.3</b>	The door or hatch shall provide access exclusively to the passenger compartment and not to any other internal section.
	<b>M2.4</b>	Passengers must board individually and be secured in an upright vertical position.
	<b>M2.5</b>	Cargo must be carried in separate, isolated cargo bays divided by solid bulkheads or floor. Each bay must have its own door or hatch that allows access only to that cargo bay.
	<b>M2.6</b>	Passengers may touch each other and the compartment walls. Teams may design any restraint system, including multiple mechanisms, and individual passengers are not required to have individual restraints.
Mission 3	<b>M3.1</b>	The banner must be at least 10 inches long and have a maximum aspect ratio of 5:1.
	<b>M3.2</b>	The banner must have the team's university name or logo on both sides and the logo must be clearly distinguishable from the original fabric color.
	<b>M3.2</b>	The banner fabric must not be altered to increase stiffness.
	<b>M3.4</b>	The banner must remain in the vertical orientation during flight.
	<b>M3.5</b>	The banner must be remotely deployed and released during flight.
	<b>M3.6</b>	The banner must be securely stowed outside the airplane during take-off without affecting flight or control functions
	<b>M3.7</b>	The banner must be rectangular with a solid border and made of solid fabric (no mesh). Enclosed weight pockets are allowed, but no rigid structures, extra holes, or extensions are permitted; slits are allowed if the logo remains legible.
Ground Mission	<b>GM.1</b>	All assembly inside the mission box must be done with the airplane upright on its landing gear; No repositioning during assembly, payload handling, or control checks..
	<b>GM.2</b>	Both the assembly crew member and the pilot may take part in the Ground Mission, only the assembly crew member is permitted to touch the airplane.

**Table 3.4: Derived Subsystem Requirements**

Subsystem	Parent Requirements	Subsystem Design Goal
Aerodynamics	<b>GR.1,GR.2,GR.10</b>	Select wing planform and airfoil to ensure stable, efficient flight across payload and banner configurations
	<b>GR.4,M2.1,M3.1</b>	The aircraft must generate sufficient lift in all flight missions
Stability & Control	<b>GR.10, M3.5</b>	Ensure sufficient tail volume and control authority to counter banner-induced moments
Mechanisms	<b>M3.4,M3.4,M3.5</b>	Design banner stowage, deployment, and release mechanisms that minimize transient loads and CG shift
Propulsion Systems	<b>M1.1,M2.1,M3.1</b>	The propulsion system must provide sufficient thrust to overcome drag in all flight missions.
Structures	<b>GR.10,M3.3,M3.5</b>	Reinforce banner tow-point and surrounding structure to safely transmit loads
Payload Integration	<b>M2.2,M2.3,M2.5</b>	Configure passenger and cargo bays to maintain CG within allowable limits
Operations	<b>GM.1,GM.2</b>	Enable rapid, repeatable mission configuration for the Ground Mission

### 3.4 Configuration Selection

A series of configuration-level trade studies were conducted to identify an aircraft architecture capable of supporting the demands of Mission 2 payload carriage, Mission 3 banner towing, and rapid ground operations. These trade studies were qualitative and semi quantitative in nature, focusing on mission compatibility rather than final sizing or optimization.

#### 3.4.1 Propulsion

Power consumption and weight optimization were assigned the highest weights because total aircraft energy consumptions directly affected achievable lap count in Mission 2 and thrust margin during high-drag banner towing in Mission 3. System reliability was weighted second highest to account for the increased operational risk with multi-motor synchronization, asymmetric thrust, and additional electronic failure points under sustained flight conditions. Aerodynamic efficiency was weighted. Ease of maintenance was similarly weighted as aerodynamic efficiency.

From the trade studies for the selection of the propulsion system, three configurations were compared across multiple parameters. Our studies indicated that a single tractor outperformed other options; a single tractor configuration reduced structural interfaces and alignment tolerances. The other configuration was prone to parasitic weight, which was absent for a single tractor. Additionally, from the aerodynamic front, a single tractor benefited from undisturbed laminar inflow compared to the turbulent wake issues of pushers.

**Table 3.5:** Propulsion Configuration Decision Matrix

Selection Criteria Power	Weighting	Single Tractor	Twin Motor	Push-Pull
Consumption	25%	5	2	3
Weight Optimization	25%	5	2	3
System Reliability (Sync)	20%	5	2	3
Aerodynamic Efficiency	15%	4	3	4
Ease of Maintenance	15%	5	2	2
Weighted Score	100%	4.85	2.15	3

#### 3.4.2 Banner Material

The selection of ripstop nylon was superior as it prevented excessive elongation and maintained consistent aerodynamic trim under high-speed air loads. During the deployment phase, when abrupt tension could otherwise result in material failure, its exceptional tear resistance was crucial. Although Kevlar had a high tensile strength, its suitability was limited by its decreased aerodynamic stability and excess fluttering, while Nylon-66 offered a lower tear resistance, its flutter and aerodynamic stability were on par to ripstop. Furthermore, by strictly omitting streamers and modifications, this material ensured the manufacturability remained simple, and the flight characteristics remained predictable.

**Table 3.6:** Banner Material Decision Matrix


Selection Criteria	Weighting	Ripstop Nylon	Nylon 66	Kevlar
Tensile Strength	25%	5	4	4
Weight Efficiency	25%	4	5	4
Tear Resistance	20%	5	3	4
Aerodynamic Stability	15%	5	5	3
Manufacturability	15%	4	4	3
Weighted Total	100%	4.6	4.2	3.7

### 3.4.3 Tail Configuration

For the selection of tail configuration, the team compared the conventional, T-tail and V-tail configurations. The primary function of the tail is to provide stability, hence it was weighted highest. Control and aerodynamic efficiency were given the next highest priority as easy handling and strong performance across all missions was crucial. Manufacturability and structural simplicity were considered next, as the empennage had to be simple to build and easy to integrate with the aircraft.

The T-tail configuration provided good control, but it was ruled out because of high structural and manufacturing complexity. The V tail configuration offered improved aerodynamic efficiency, but it was difficult to control and had high structural complexity. Although the conventional tail did not offer the highest aerodynamic efficiency, it was selected due to its simple structure, ease of manufacture, and reliable stability and control characteristics across all mission phases.

**Table 3.7:** Tail Configuration Decision Matrix


Selection Criteria	Weighting	Conventional	T-tail	V-tail
Stability	30%	5	4	3
Control	20%	5	4	2
Manufacturability	15%	5	2	3
Structural Simplicity	15%	4	2	3
Aerodynamic Efficiency	20%	2	3	5
Weighted Total	100%	4.25	3.2	3.2

### 3.4.4 Wing Placement

Wing placement configurations studied were high wing, mid wing, and low wing and were compared based on parameters relevant to mission performance and competition requirements. Payload access was given the highest weightage due to its direct impact on ground mission scoring by reducing payload loading and unloading time. Manufacturability and payload volume were given the next highest importance, as it should be easy to build and should be able to carry large payload volume.

Although the high-wing and low-wing configurations offered good payload volume and less manufacturing complexity, it was difficult to access the fuselage due to wing obstruction. The mid-wing configuration allowed easy access to the fuselage, provided good stability and control. Based on the weighted scores, the mid-wing configuration achieved the highest total score and was selected.

**Table 3.8:** Aircraft Configuration Decision Matrix

				
Selection Criteria	Weighting	High-wing	Mid-wing	Low-wing
<b>Payload Access</b>	35%	3	5	3
<b>Stability and Control</b>	15%	3	5	3
<b>Manufacturability</b>	20%	5	3	4
<b>Payload Volume</b>	20%	5	3	5
<b>Takeoff Field Length</b>	10%	3	4	4
<b>Weighted Total</b>	<b>100%</b>	<b>3.8</b>	<b>4.1</b>	<b>3.7</b>

### 3.4.5 Landing Gear

For the selection of tail configuration, the team compared the tail-dragger, tricycle, and quad-gear. Drag and landing characteristics were given the highest weightage, as they directly affect takeoff performance and landing safety. Simplicity was given the next highest importance to ensure the landing gear is easy to build, reliable, and easy to integrate. As propeller clearance affects safe operation during takeoff and landing, it was also taken into consideration.

The tail-dragger offers high propeller clearance but has less favourable landing behaviour, while the quad-gear provides good ground stability but offers high drag and design complexity. The tricycle configuration offers a good balance of low drag, simplicity, and stable landing characteristics. Based on the weighted scores, the tricycle landing gear configuration achieved the highest score and was selected.

**Table 3.9:** Landing Gear Configuration Decision Matrix

				
Selection Criteria	Weighting	Taildragger	Tricycle	Quadgear
<b>Drag</b>	25%	3	4	2
<b>Propeller Clearance</b>	15%	5	4	4
<b>Design Simplicity</b>	20%	4	5	2
<b>Landing Characteristics</b>	25%	3	4	5
<b>Weight</b>	15%	4	4	3
<b>Weighted Total</b>	<b>100%</b>	<b>3.65</b>	<b>4.2</b>	<b>3.2</b>

### 3.5 Final Conceptual Design

Based on the mission requirements, scoring sensitivity analyses, and configuration trade studies, multiple conceptual aircraft configurations were evaluated for a suitable baseline for further development. The results indicated that a single-tractor propulsion layout combined with a conventional tail, mid wing configuration, and tricycle landing gear provided the best balance of aerodynamic efficiency, stability, structural simplicity, and operational reliability. The conceptual configuration shown in Figure 3.5 was therefore selected as the baseline for subsequent preliminary and detailed design refinement.



Figure 3.5: Final Conceptual Design

## 4.Preliminary Design

### 4.1 Design Methodology

The design methodology followed an iterative process based of competition rules. A scoring sensitivity analysis in MATLAB identified the parameters with the greatest influence on mission score, guiding configuration selection and preliminary aircraft sizing, including aerodynamics, propulsion, weight estimation, and center of gravity placement.

Software-based verification was then used to refine the design and ensure aerodynamic and stability requirements were met, including airfoil selection and wing taper ratio optimization. AVL [2] and XFLR5 [3] were the tools used to assess stability derivatives, trim, and static margin. CFD simulations in ANSYS provided higher-fidelity aerodynamic analysis. Detailed design was completed in Onshape, integrating structures, payload systems, and wiring constraints. Structural integrity was validated through ANSYS FEA to confirm the airframe could absorb the expected flight and landing loads.

Following design freeze, manufacturing was carried out using laser-cut plywood, 3D-printed components, and composite layups. The aircraft then underwent static thrust tests, ground mission trials, wind tunnel test and full flight testing to validate performance predictions. Test data were processed in Tecplot and compared against mission-level models, enabling final refinements. This closed-loop workflow ensured alignment between analysis, design, and testing, resulting in a reliable and competition-ready final aircraft.

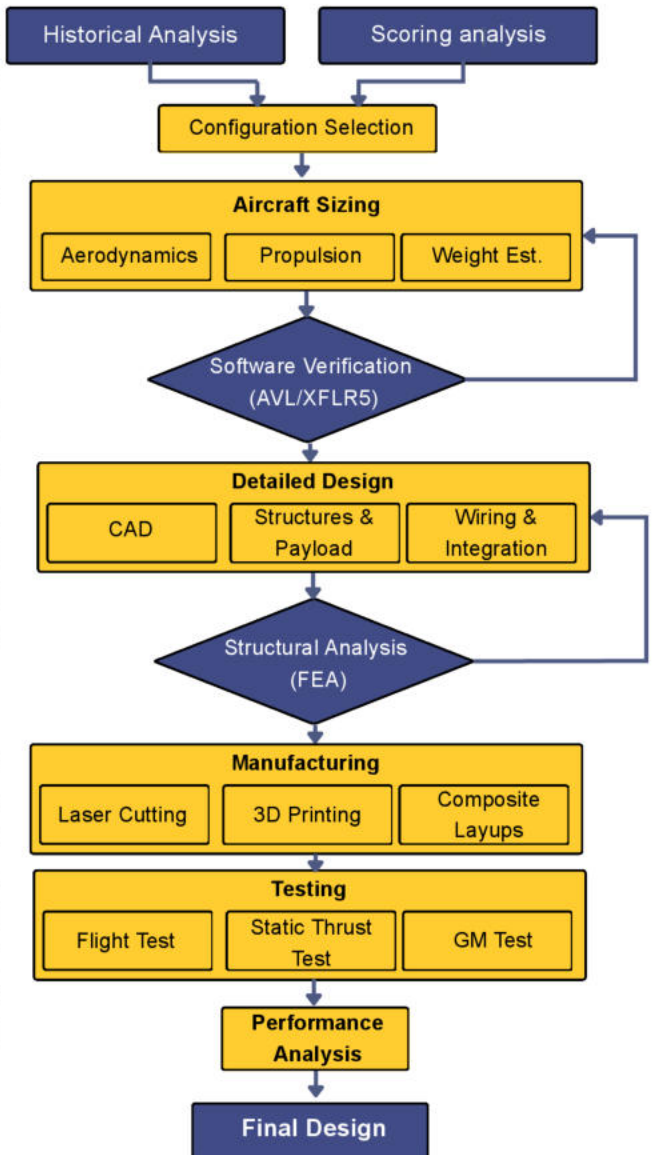


Figure 4.1: Design Process

## 4.2. Design Trade Studies

### 4.2.1 Banner Sizing

Banner drag testing was conducted in a wind tunnel using a suspended, pre-calibrated, hook-type load cell with a measurement uncertainty of  $\pm 0.01$  lb. Banners with an aspect ratio (AR) of 5, the maximum permitted by competition rules [4], were tested to represent the best case drag scenario, as drag force scales proportionally with surface area.

Ripstop nylon was selected for this application primarily due to its superior performance at high Reynolds numbers ( $R_e$ ), which was a critical requirement for maintaining aerodynamic stability. The experimental configuration used to evaluate this material is detailed in Section 7.1. A comprehensive discussion of the resulting data and plots, is provided in Section 8.1.

**Table 4.1:** Optimal banner for wind conditions

Windspeed (mph)	Optimal banner Length (ft)	No of laps
0	20	5
8	18	5
19	16	5
22	14	5
28	11.5	5
33	8.5	5

By applying the M3 optimization function to the experimental mean  $C_d$  value 0.03, the optimal banner length was calculated to be 20ft in still air.

### 4.2.2 Propulsion System

#### 4.2.2.1 Constraint Analysis

**Table 4.2:** Propulsion System Constraint Analysis

Constraint No.	Requirements
<b>Constraint - 0</b>	Aircraft must be propeller-driven and electric powered.
<b>Constraint - 1</b>	Must use an unmodified, over-the-counter brushed or brushless electric motor.
<b>Constraint - 2</b>	Aircraft must have an externally accessible switch to turn on the radio control system. It cannot be internal, under a hatch, or a panel. An arming plug is not acceptable. The RC switch must be separate from the propulsion arming/fuse system.
<b>Constraint - 3</b>	Propulsion batteries may be NiCAD, NiMH, or lithium-based chemistries.
<b>Constraint - 4</b>	A separate battery is required for the Rx/Servo system. No restriction on Rx/Servo or transmitter battery type.
<b>Constraint - 5</b>	Total propulsion energy onboard must not exceed 100 Wh (sum of all propulsion batteries).
<b>Constraint - 6</b>	Maximum arming fuse current rating equals the battery's maximum continuous discharge rating (Capacity $\times$ C-rating), capped at 100 A.

#### 4.2.2.2 Propulsion Selection

The design choices for Pushpak's propulsion system were based on the requirements of meeting high efficiency in M2 and high maximum power in M3. The main constraint which limits the aircraft's performance is presented in terms of using battery energy effectively (Constraint-5 and Constraint-6) while also providing the static thrust requirements. The constraints require optimizing the propulsion system for maximum performance across M3, while optimizing M2 score simultaneously. Pushpak's propulsion system design began with the motor, as it was identified as the most limiting component in terms of achieving the necessary thrust output and maintaining minimal power consumption. The next step was to make a choice for a propeller. Ultimately, the choice for the battery was made to provide the required power within the fuse limits per Constraint-6. Analysis of previous DBF aircrafts' propulsion systems provided a starting point.

#### 4.2.2.2.1 Motor Selection

The aim here was to determine a motor which would achieve the desired thrust requirements for take-off, climb and turns. The propulsion system was designed to produce a thrust-to-weight ratio of 1.4 for M3 and a thrust-to-weight ratio of 0.8 while keeping power consumption to under 100Wh per Constraint-5. Further, based on the score optimization analysis, cruise power efficiency was to be optimized to maximize endurance.

Propulsion Selection Requirements are as follows:

Table 4.3: Motor Requirements

Parameter	Requirement
Power	Complete mission requirements in 80 Wh (at 80% discharge) of battery energy.
Static Thrust	Satisfy the minimum lower bound static thrust limit of 12.35 lbf.
M2	Most efficient operation at the throttle setting which gives a flight time of 5 minutes (at 80% discharge).
M3	Achieves high dynamic thrust through motor RPM.
Product Availability	Have to be available in India. Stock is limited compared to North-America and Europe.

Based on these requirements, over 300 propeller-motor-battery configurations were analysed in QPROP [5] using a python script and the top 10 combinations from the script were then evaluated through eCalc to obtain data for predicting M2 and M3 scores. The top 5 propulsion configurations were considered for mission analysis and were compared based on their predicted scores. From the above analysis, it was identified that the T-Motor AM670 520KV motor with a 18 inch propeller resulted in the highest total mission score and individual M2 and M3 scores compared to the other combinations.

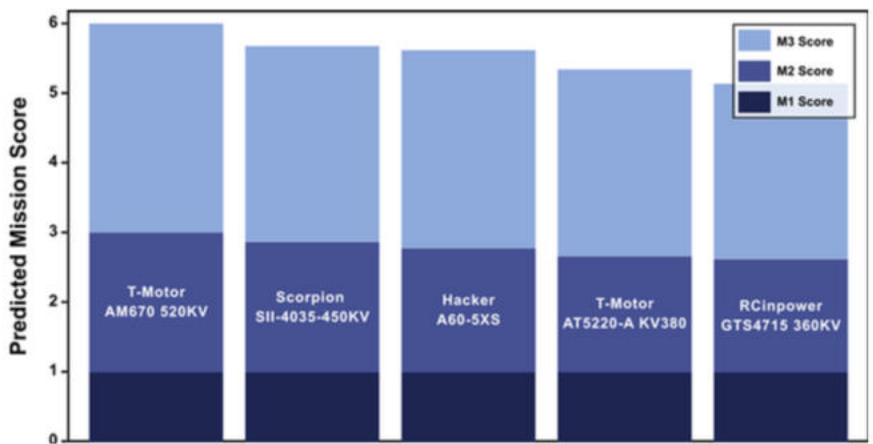


Figure 4.2: Predicted Mission Score for Motor Combinations

#### 4.2.2.2.2 Propeller Selection

The next selection choice was to select the optimal material, diameter and pitch for the T-Motor AM670 520KV. Equation 1 was used to calculate the suggested diameter of props for the selected electric motor, see Ref [6].

$$T = C_T \cdot \rho \cdot n^2 \cdot D^4 \quad \text{--- Equation 4.1}$$

$C_T$  was taken as 0.1 based on generic prop manufacturing. Using required values of thrust and general air density of Wichita, Kansas, an estimated prop size of 18 inch was obtained from the given equation. This diameter also directly validates the recommended prop diameter of T-Motor AM670 520KV of 18 inch. The 18 inch diameter became a valid base for evaluating propellers of various materials, diameters and pitches. 3 materials for the props were selected:

Table 4.4: Propeller Material Selection

Propeller Material	Characteristics	Advantages
Carbon Fiber (CF)	Extremely rigid with minimal flex at high RPM	High efficiency, strong thrust performance, lightweight (high strength-to-weight ratio), ideal for high-thrust applications.
Fiberglass	Good balance of strength and flexibility	Less brittle than CF, better damage tolerance, more cost-effective.
Wooden	Natural airfoil-like blade shape	Good RPM efficiency, smoother motor compatibility, lightweight.

Static propulsion testing was carried out on props of these materials for similar diameter and pitch. Based on the results obtained in the test, the propellers were optimized to generate the maximum thrust possible while maintaining the desired power consumption.

#### 4.2.2.3 Battery Selection

With the initial motor and propeller selected, the last component of the propulsion system to be selected was the battery. The total energy capacity of a battery was calculated using:

$$\text{Energy (Wh)} = 1000 \cdot \text{mAh} \cdot V_{\text{nominal}} \quad \text{--- Equation 4.2}$$

Based on T-Motor AM670 520KV's recommended battery and battery charging constraints, 6S Li-chemistry were identified as viable options. For 6S batteries, which have a nominal rating of 22.2 V, remain under the 100 Wh, a highest rating of 4500 mAh can be used. An actual value of 99.9 Wh is rated for a 4500 mAh 6S Lithium-Polymer (LiPo) battery, which is under the 100 Wh limit. The primary trade-off in battery selection involved balancing current drawn and capacity while ensuring compliance with Constraint-5. Two battery chemistries were selected and tested to prioritise high current output to ensure power delivery and banner deployment performance for M3, and prioritizing endurance for M2:

**Table 4.5:** Battery Type Selection

Battery Type	Characteristics	Advantages and Mission Suitability
LiPo (Lithium-Polymer)	High discharge rate, capable of delivering large	Superior power-to-weight ratio, improved climb performance and thrust response; suitable for Mission 3 (high power demand)
Li+ (Lithium-Ion)	Higher energy density, moderate discharge	Longer endurance for the same weight, improved flight duration; suitable for Mission 2 (endurance-focused)

#### 4.2.2.3 Performance

MotoCalc [7] flight simulation was conducted on Pushpak's propulsion system.

**Table 4.6:** Pushpak Propulsion System Performance Analysis

Flight Stage	Performance
Takeoff	<ul style="list-style-type: none"> <li>Exceptional initial acceleration performance allows Pushpak to take off quickly with minimum energy consumption.</li> <li>Very short take-off runs and high climb-outs with no problem in taking off from grass runways.</li> <li>The chosen 18x8 carbon fiber propeller can withstand high RPMs without flexing.</li> </ul>
Rate of Climb	<ul style="list-style-type: none"> <li>A continuous climb rate of 17.85 ft/s at a 13.4° angle is achieved.</li> <li>At the best lift-to-drag ratio airspeed, Pushpak has strong climb and acceleration characteristics, essential for recovering altitude after aggressive turn maneuvers in Mission 3.</li> <li>Energy delivery from the 6S LiPo battery remains highly efficient during these climb phases.</li> </ul>
Cruise	<ul style="list-style-type: none"> <li>The airframe features a wing loading of 0.49 oz/in² due to which, Pushpak benefits from good penetration in strong winds and requires a high flying speed.</li> <li>The optimum best lift-to-drag flight speed is 77.09 ft/s at 87% throttle.</li> <li>The propulsion system inherently generates excess thrust allowing Pushpak to overcome the sudden and massive increase in parasitic drag due to deployment of the banner in M3.</li> </ul>
Turns	<ul style="list-style-type: none"> <li>Turn maneuvers induce significant drag because the aircraft's stall speed is relatively high.</li> <li>Additional parasitic drag is induced by the deployed banner which induces drag on the turn.</li> <li>The high power-on thrust translates directly into the propulsion system maintaining a sufficient thrust margin to power through turns even with drag forces of the turn and the deployed banner.</li> </ul>

## 4.3 Aerodynamics

### 4.3.1 Airfoil Selection

The airfoil selection for Pushpak was performed using a mission focused, quantitative trade study that balanced aerodynamic efficiency, gust tolerant handling, structural integration and manufacturability. The selection process was explicitly divided into two sets of analysis: Aerodynamic Classification, and Structural and Manufacturability Classification which are given as below:

#### 4.3.1.1 Aerodynamic Classification

Aerodynamic performance was evaluated in XFLR5 using the XFOIL solver (3) at  $Re = 6.0 \times 10^5$ , representative of cruise at 20–23 m/s. The analysis was done for four candidate airfoils: E423, S1223M, SD7062 and FX63-137, all candidates exhibited similar linear lift slopes of approximately 0.1/deg, significant differences appeared near stall and in drag performance. S1223 achieved the highest  $C_{L,\max} \approx 1.9$  but stalled abruptly at  $\alpha \approx 11^\circ$ . In contrast, SD7062 reached  $C_{L,\max} \approx 1.55$  with delayed stall at 14–15° and the smoothest post-stall behavior, improving gust tolerance. In the cruise lift range ( $C_L = 0.5\text{--}0.7$ ), SD7062 demonstrated the lowest drag ( $C_D \approx 0.015\text{--}0.017$ ), yielding a  $(C_L/C_D)_{\max} \approx 85\text{--}90$ . It has a moderate pitching moment ( $C_{m0} \approx -0.06$ ) and it reduces trim drag compared to highly cambered sections such as S1223 with  $C_{m0} \approx -0.12$ . Overall, SD7062 provided the best aerodynamic efficiency and stability balance.

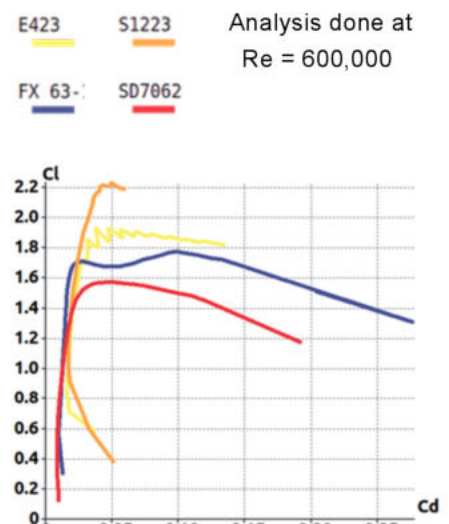


Figure 4.3:  $C_l$  vs  $C_d$

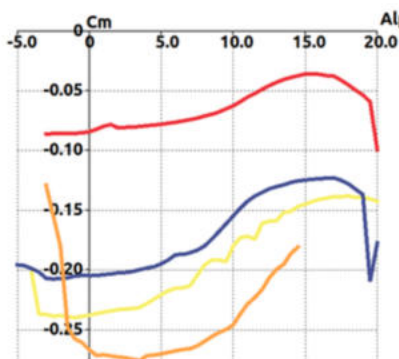


Figure 4.4 (a):  $C_d$  vs  $\alpha$

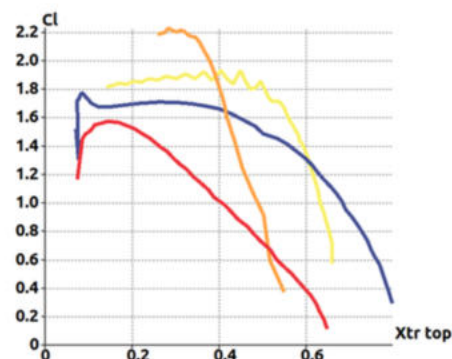


Figure 4.4 (b):  $C_l$  vs  $C_p$  location (Xtr)

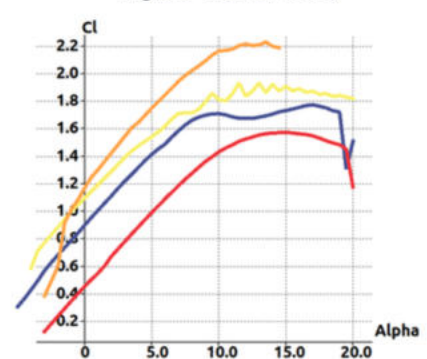


Figure 4.4 (c):  $C_l$  vs  $\alpha$

Figure 4.4: Comparison of Airfoil Characteristics

Table 4.7: Aerodynamic Performance Scoring\*

Parameter	$C_{d,\min}$	$C_{m0}$	$\alpha_s$	$\left(\frac{C_l}{C_d}\right)_{\max}$	$C_{l,\alpha=0}$	$C_{l,\max}$	Post Stall Slope	Final Score
Weight	20%	10%	20%	20%	10%	10%	10%	100%
E423	0.7176	0.3524	0.8389	1	0.9133	0.8653	0.5442	77.88
S1223	0.6238	0.3581	0.9463	0.8085	1	1	0.1836	72.99
SD7062	1	1	1	0.8117	0.384	0.7386	1	87.46
FX 63-137	0.9046	0.4097	0.8993	0.8535	0.768	0.8143	0.6622	79.69

\*Values in the Table 4.7 are scaled using the formula  $(\text{Current Value})/(\text{Maximum Value})$  for the parameters that were better with a higher magnitude, and the formula  $(\text{Minimum Value})/(\text{Current Value})$  for the opposite. The same formula will be followed in Section 4.3.1.2

#### 4.3.1.2 Structural and Manufacturability Classification

Structural analysis was conducted considering maximum thickness, thickness location relative to one-third chord spar position, and leading-edge radius. SD7062 achieved the highest structural score of 80.73 due to its 14% thickness, favorable thickness distribution of about 25% chord and a robust leading edge radius, improving both bending and torsional stiffness. Even though E423 was ranked highest in fabrication simplicity, SD7062 achieved a competitive score of 69.55 without any structural penalties. Location of maximum thickness was chosen to be at 33.3% of the chord for optimal spar placement and scaled with respect to the same. All parameters in the studies that follow have equal (33.3%) weightage.

**Table 4.8:** Structural Integrity Scoring

Parameter	Maximum Thickness (%)	Scaled Maximum Thickness	Location of Maximum Thickness (% chord)	Scaled Location of Maximum Thickness	Leading Edge Radius (% chord)	Scaled Leading Edge Radius	Final Score (in %)
E423	12.5	0.8929	23.7	0.2889	4.7	0.7833	65.5
S1223	12.1	0.8643	19.8	0	1.2	0.2	35.48
<b>SD7062</b>	<b>14</b>	<b>1</b>	<b>25.5</b>	<b>0.4222</b>	<b>6</b>	<b>1</b>	<b>80.73</b>
FX 63-137	13.7	0.9786	30.9	0.8222	2.8	0.4667	75.58

For manufacturability, thickness ratio, trailing edge bluntness and camber complexity was considered for evaluation. With mission weightings of 50% aerodynamic, 30% structural and 20% manufacturability, SD7062 attained the highest composite score of 81.86 and was therefore selected as the wing airfoil for Pushpak. All parameters in the studies that follow have equal (33.3%) weightage.

**Table 4.9:** Manufacturability Scoring

Parameter	Thickness to chord ratio (t/c ratio)	Scaled t/c ratio	Trailing Edge Sharpness	Scaled Trailing Edge Sharpness	Camber Complexity	Scaled Camber Complexity	Final Score
E423	12.5	0.8929	11.9	1	9.5	0.3684	75.37
S1223	12.1	0.8643	0.57	0.0479	8.1	0.4321	44.81
<b>SD7062</b>	<b>14</b>	<b>1</b>	<b>1.03</b>	<b>0.0866</b>	<b>3.5</b>	<b>1</b>	<b>69.55</b>
FX 63-137	13.7	0.9786	0.57	0.0479	6	0.5833	53.66

**Table 4.10:** Overall Scoring

Parameter	Aerodynamic Performance	Structural Integrity	Manufacturability	Final Composite Score (in %)
<b>Weight</b>	<b>50%</b>	<b>30%</b>	<b>20%</b>	<b>100%</b>
E423	77.88	65.5	75.37	73.66
S1223	72.99	35.48	44.81	56.1
<b>SD7062</b>	<b>87.46</b>	<b>80.73</b>	<b>69.55</b>	<b>81.86</b>
FX 63-137	79.69	75.58	53.66	73.25

#### 4.3.2 Aerodynamic Component Analysis

Following airfoil selection, the dimensional aerodynamic performance of the wing was evaluated using Athena Vortex Lattice (AVL) [2]. AVL models lifting surfaces as discrete vortex lattices and provides rapid, reliable estimates of lift distribution, induced drag, oswald efficiency and stability derivatives. A custom python-AVL automation pipeline was developed for generating geometries, executing trim cases and extracting coefficients of analysis.

#### 4.3.2.1 Wing Aerodynamic Analysis

A baseline rectangular wing was first analyzed to quantify the aerodynamic penalty of geometric simplicity. The lift curve exhibited a linear slope of approximately  $C_{L\alpha} \approx 0.067$  per degree with stable pitching-moment variation, confirming predictable trim behavior; however, induced drag and Oswald efficiency indicated non-optimal span-wise loading, with efficiency remaining below  $e \approx 0.96$ . To improve performance, the planform was parameterized by taper ratio ( $\lambda$ ) and taper start location ( $\eta$ ) while keeping a span of 5 ft and area of 812.3616 sq. in constant. Automated AVL [2] sweeps at  $\lambda = 0.5$  revealed clear trade-offs: near-rectangular wings increased induced drag, aggressive taper degraded root loading and trim angle, and improper taper onset distorted lift distribution. Figure 4.6 contours clearly shows a concentrated performance region rather than a broad spectrum, highlighting the sensitivity to taper placement.

The optimal region emerged near  $\lambda \approx 0.5$  and taper start  $\approx 0.4$  semi-span, where induced drag was minimized, Oswald efficiency increased to  $e \approx 0.995$ , and trim angle remained moderate. In this region, spanwise loading approached an elliptical distribution without excessive inboard concentration. Trefftz-plane analysis confirmed smoother circulation decay and visibly reduced tip loading compared to the baseline configuration. This tapered configuration was therefore selected for further aerodynamic evaluation.

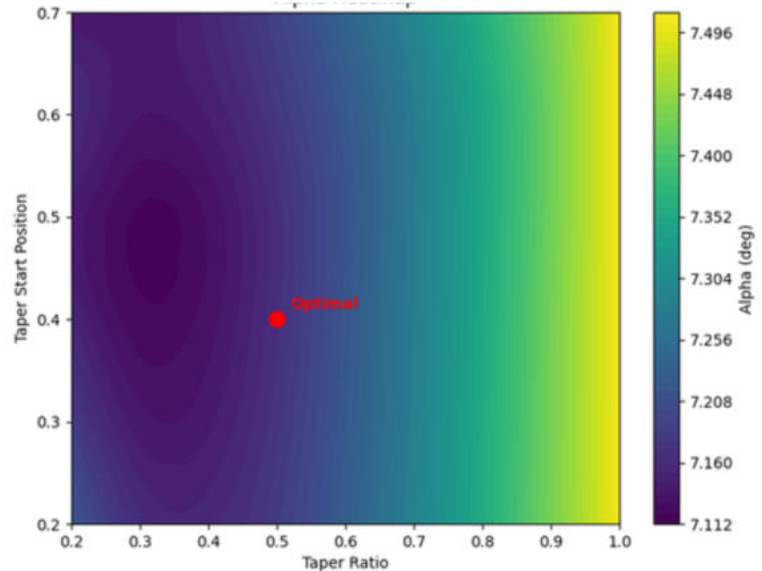


Figure 4.5:  $\alpha$  Contour ( $\lambda-\eta$ )

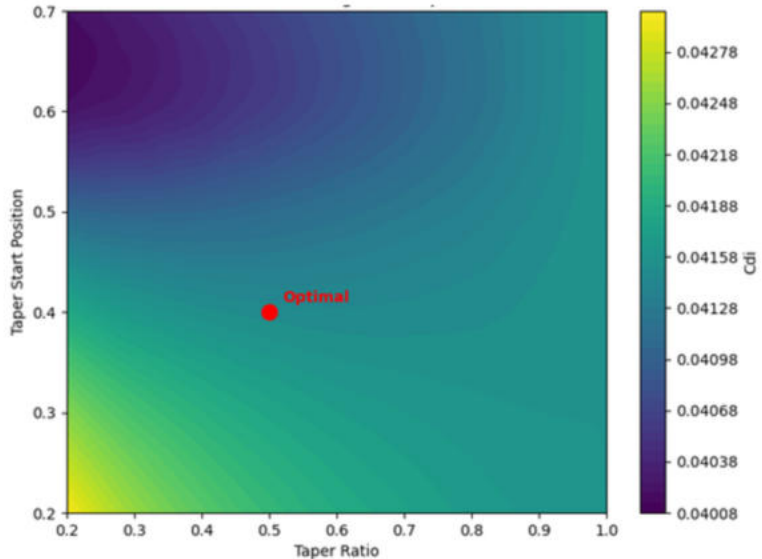


Figure 4.6:  $C_{d_i}$  Contour ( $\lambda-\eta$ )

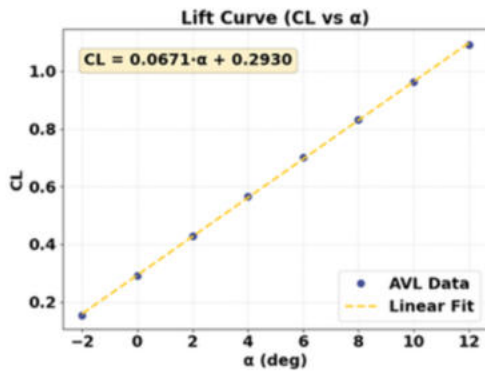


Figure 4.7: Baseline Rectangular Plots ( $C_L$  vs  $\alpha$ )

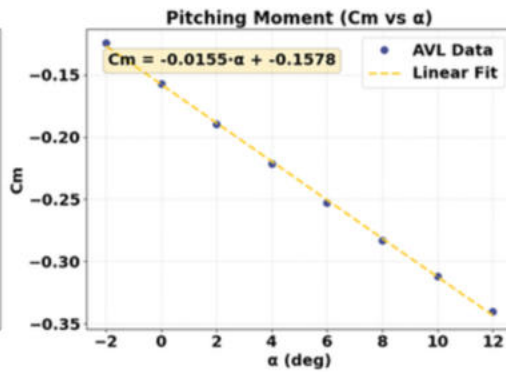


Figure 4.8: Baseline Rectangular Plots ( $C_m$  vs  $\alpha$ )

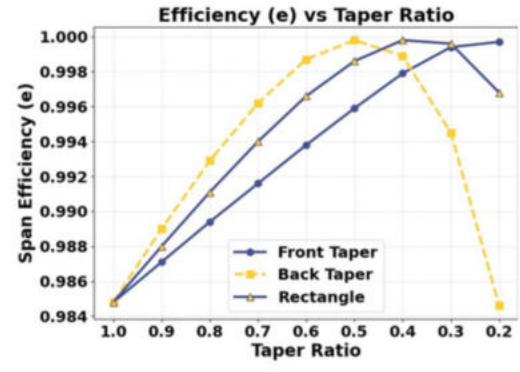


Figure 4.9: Efficiency ( $e$ ) vs Taper Ratio

#### 4.3.2.2 Flap Geometry Optimization

With the planform fixed, high-lift devices were optimized using AVL [2] within a Pareto framework varying flap span fraction and flap chord fraction. Each configuration was trimmed to extract  $\Delta C_L$ ,  $\Delta C_m$ , and  $\Delta C_{D_i}$ . The Pareto fronts show the expected aerodynamic coupling: increasing flap span or chord increases lift augmentation but introduces stronger nose-down pitching moments and higher induced drag. The optimal compromise region maximizes lift gain without disproportionate trim or drag penalties. A flap chord fraction of 0.30 and aileron chord fraction of 0.20 were selected, providing substantial takeoff lift augmentation while maintaining manageable pitching-moment shifts and acceptable cruise efficiency.

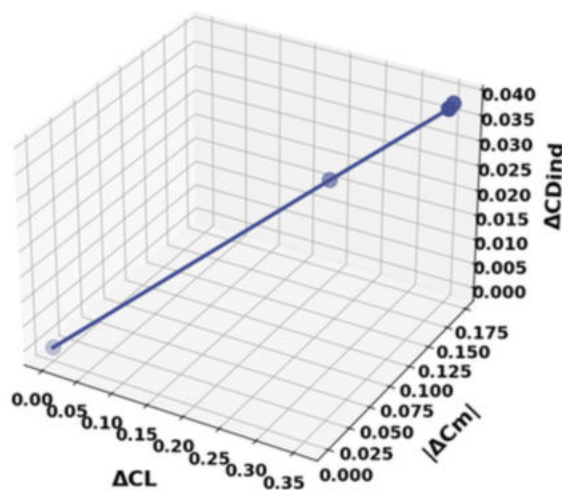


Figure 4.10: Aerodynamic Tradeoff ( $\Delta C_L$ – $\Delta C_m$ – $\Delta C_{D_i}$ )

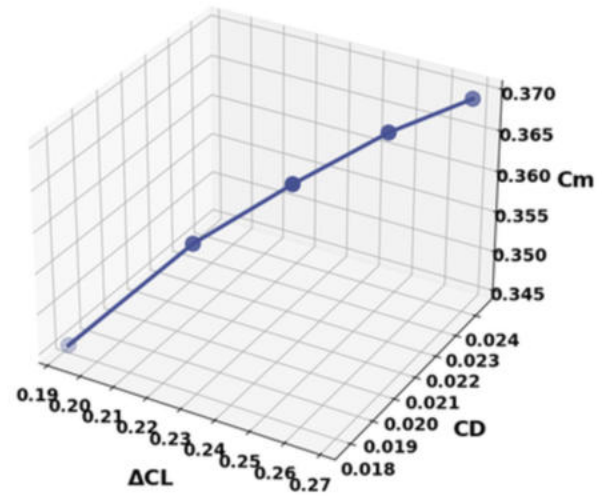


Figure 4.11: Performance Tradeoff ( $\Delta C_L$ – $CD$ – $\Delta C_m$ )

AVL [2] geometry visualization and Trefftz-plane analysis at  $C_{l_0} = 0.5$  confirm smooth spanwise loading and reduced tip vortex intensity for the finalized configuration.

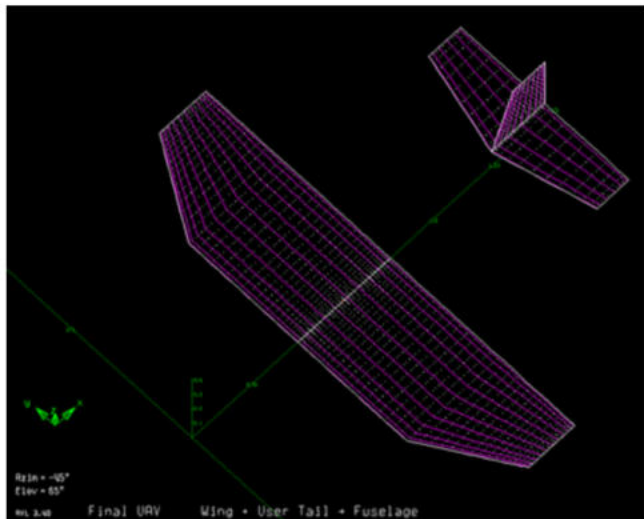


Figure 4.12: AVL Aircraft Model

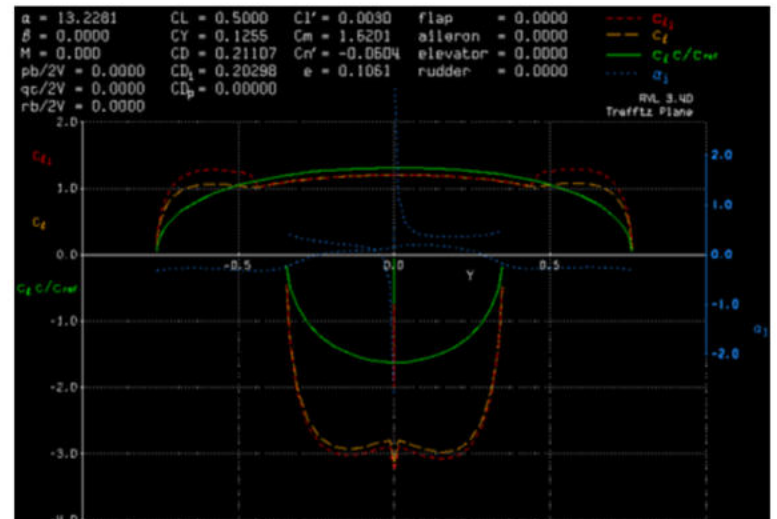


Figure 4.13: Trefftz Plane Analysis of the Aircraft at Cruise

#### 4.3.2.3 Tail Analysis

Tail sizing was carried out to ensure sufficient longitudinal and directional stability during heavy lift and banner towing. The horizontal and vertical tail volume coefficients were defined as (from Roskam [8]) :

$$V_h = \frac{l_t S_H}{\bar{c} S_w} \text{ --- Equation 4.3}$$

$$V_V = \frac{l_t S_V}{b S_w} \text{ --- Equation 4.4}$$

Where  $S_H$ ,  $S_V$ ,  $\bar{c}$ ,  $b$ ,  $S_w$ , and  $l_t$  represent the horizontal stabilizer area, vertical stabilizer area, mean aerodynamic chord, wingspan, wing area, and tail moment arm. These values were iterated to provide adequate restoring moments against banner-induced pitching and yawing loads.

The final design uses  $V_h = 0.761$  and  $V_V = 0.07$ , giving  $S_H = 186.69 \text{ in}^2$  and  $S_V = 80.85 \text{ in}^2$ . A brief parametric study shows that increasing  $V_h$  improves static margin and tail downforce but increases drag; the selected value represents a balanced compromise between stability and aerodynamic efficiency.

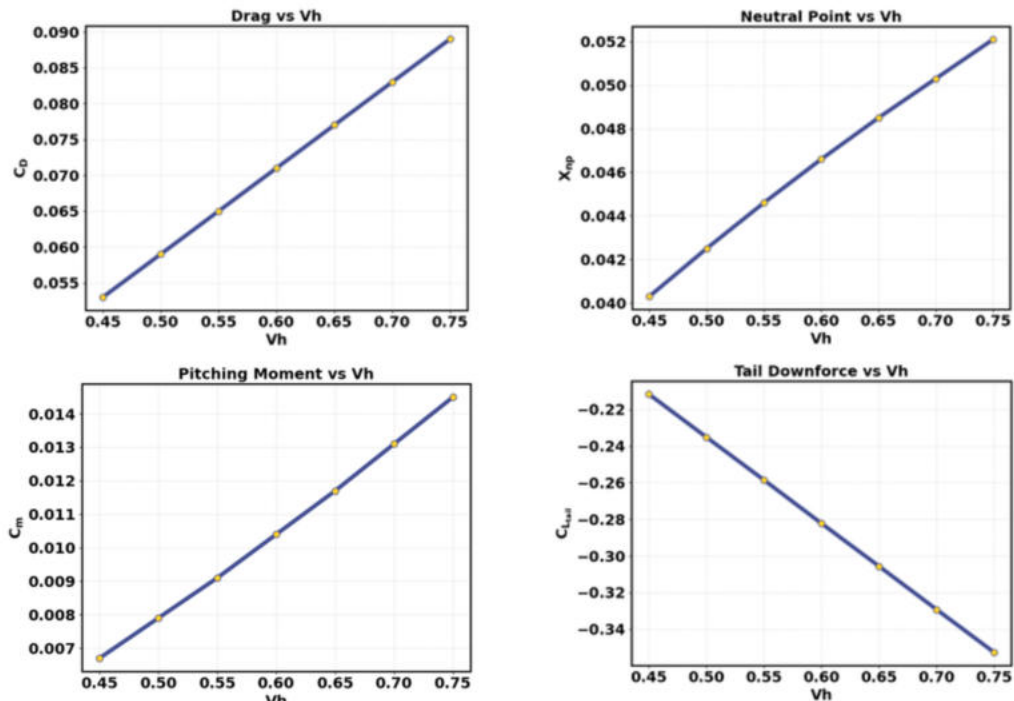


Figure 4.14: Longitudinal Characteristics vs  $V_h$

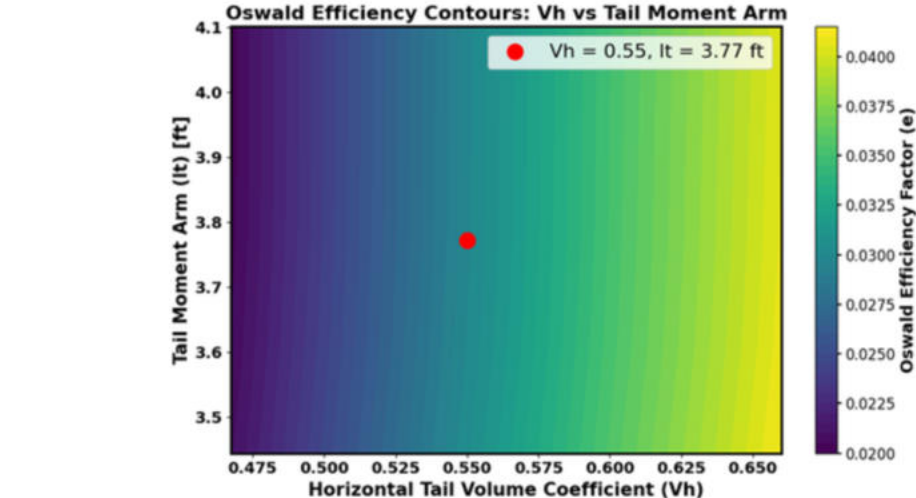


Figure 4.15: Oswald Efficiency Contour ( $V_h - l_t$ )

### 4.3.3 Drag Analysis

#### 4.3.3.1 Analytical Drag Calculations

Roskam [9] was used to analytically estimate the parasitic drag coefficient  $C_D$  using the component build up method. The primary equation for the component drag coefficient is defined as:

$$C_{D_0} = \frac{C_f \cdot FF \cdot Q \cdot S_{wet}}{S_{ref}} \quad \text{--- Equation 4.5}$$

Where  $C_f$  is the flat-plate skin friction coefficient,  $FF$  is the form factor,  $Q$  is the interference factor,  $S_{wet}$  is the wetted area of the component, and  $S_{ref} = 719.97 \text{ in}^2$  is the wing reference area.

For cruise conditions, the  $C_f$  was taken as 0.0039. For the fuselage, the form factor was determined using the ratio  $l_f/d_f = 7.84$ , corresponding to the fuselage length of 1.42122. The inference factor  $Q$  accounts for mutual flow interaction between components. The table summarizes the results obtained.

**Table 4.11:** Analytical Drag Analysis

Component	$S_{wet}$	$C_f$	Form Factor	$C_{d_0}$
Fuselage	1294.25	0.0039	1.06	0.009664
Wing	1490.33	0.0039	1.0697	0.0120685
Horizontal Tail	373.39	0.0039	1.0486	0.02337

The results confirm that drag is predominantly driven by lifting surface wetted area rather than slender body components.

#### 4.3.3.2 Numerical Drag Calculations

A detailed parasite drag analysis was performed in OpenVSP, and the resulting pie charts indicate that the wing is the dominant contributor to parasite drag, accounting for approximately 45–54% across missions. The fuselage contributes roughly 21–26%, while the horizontal and vertical stabilizers together contribute about 10–20%, depending on configuration. In Mission 3, the presence of payload and additional components increases the relative drag contribution beyond the primary lifting surfaces, as reflected in the bar chart where payload-related drag becomes significant. The bar graph further shows that while profile drag of the wing remains comparable between Missions 1 and 2, Mission 3 experiences a noticeable increase in total drag due to added payload and associated interference effects. Induced drag was calculated separately using AVL [2] at cruise lift conditions, confirming that Mission 3 exhibits higher induced drag due to increased lift loading.

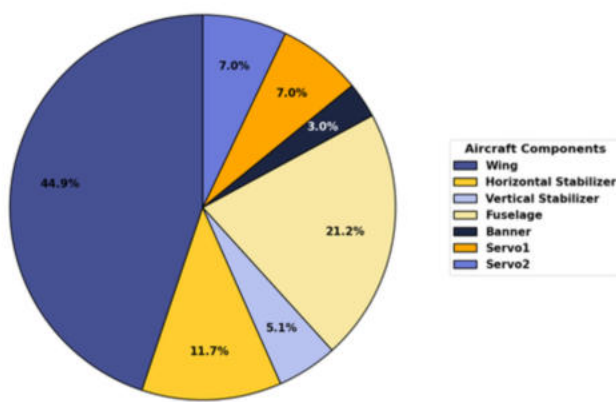


**Figure 4.16:** Mission 2 Drag Breakdown

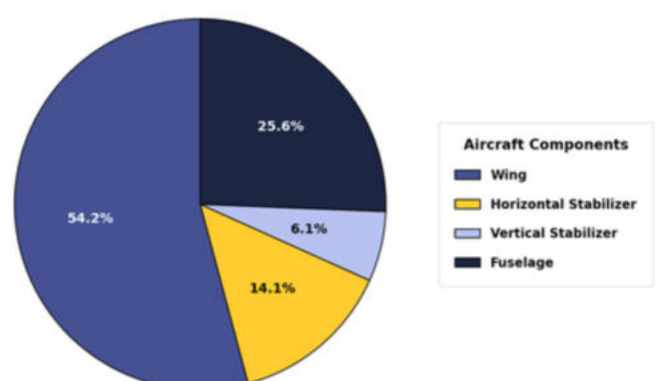


**Figure 4.17:** Mission 3 Drag Breakdown

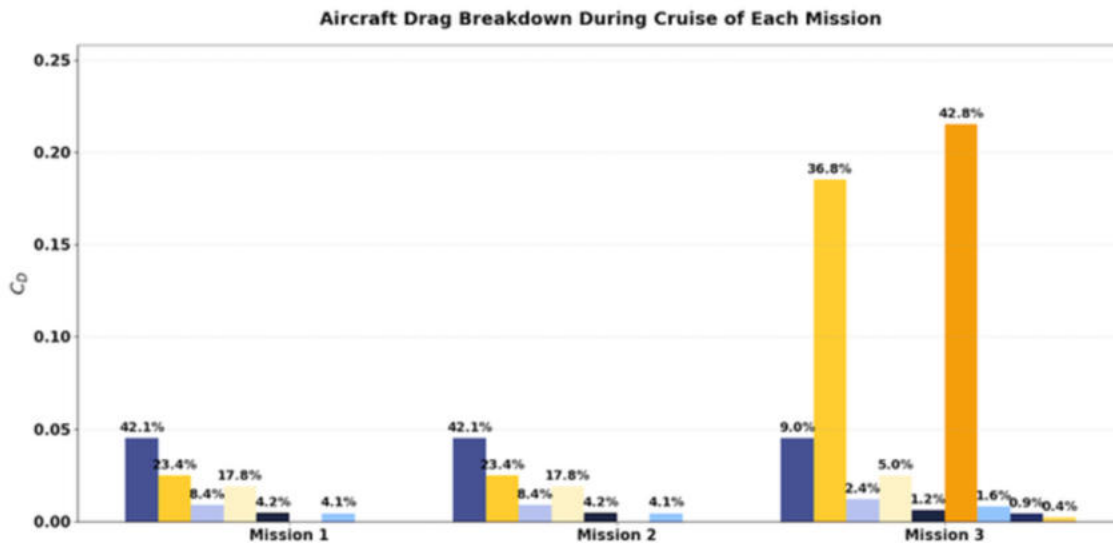


Figure 4.18: Mission-wise Cruise Drag Distribution

## 4.4 Stability and Control

### 4.4.1 Static Stability Analysis

Static stability refers to the initial tendency of an aircraft to return to its trimmed equilibrium state after experiencing a small disturbance. The static stability derivatives used here were obtained from AVL [2] analysis, and the table below compares the longitudinal and lateral-directional stability and control derivatives for Missions 1, 2, and 3. Longitudinally, all missions are statically stable with negative  $C_{m_a}$ , equal to -2.3266 (M1), -1.1625 (M2), and -2.0996 (M3) showing that high pitch stiffness is exhibited by M1 followed by M3 and then M2.

The lift-curve slope  $C_{L_a}$  remains nearly unchanged across missions (5.0948 – 5.1583), indicating consistent wing aerodynamic performance. Strong negative  $C_{m_q}$  values (-13 to -16) ensure well-damped short-period behavior in all cases. Laterally, similar  $C_{Y\beta}$ ,  $C_{I\beta}$ , and  $C_{n\beta}$  values indicate that dihedral and directional stability remain consistent, with M1 and M3 slightly more directionally stable than M2. The analytical findings were reflected in the flight performance of the aircraft, in which each mission exhibited control characteristics consistent with the AVL [2] analysis.

Table 4.12: Longitudinal Static Stability Derivatives

Longitudinal				
Control Derivative	Parameter	M1	M2	M3
$C_{L_a}$	Lift change with AoA	5.0948	5.1583	5.1074
$C_{m_a}$	Static pitch stability	-2.3266	-1.1625	-2.0996
$C_{m_q}$	Pitch damping	-15.9999	-13.2046	-15.3752
$C_{L_{\delta_e}}$	Elevator lift authority	0.01621	0.01597	0.01616
$C_{m_{\delta_e}}$	Elevator pitch authority	-0.03496	-0.03103	-0.03418

Table 4.13: Lateral Static Stability Derivatives

Lateral					
Control Derivative	Parameter	M1	M2	M3	
$C_{L_\beta}$	Dihedral stability	-0.1316	-0.1290	-0.1311	
$C_{n_\beta}$	Weathercock stability	0.1709	0.1557	0.1679	
$C_{L_p}$	Roll damping	-0.3784	-0.3825	-0.3792	
$C_{n_r}$	Yaw damping	-0.1785	-0.1519	-0.1731	
$C_{L_{\delta_a}}$	Aileron roll control	-0.00399	-0.00405	-0.00400	
$C_{n_{\delta_e}}$	Rudder yaw control	0.00173	0.00161	0.00171	

#### 4.4.2 Dynamic Stability Analysis

After analyzing the static stability, the dynamic modes were extracted from AVL [2] analysis and xz represented on a root locus plot in the complex plane as seen in figure. All 5 primary modes lie in the left half of the complex plane which indicate dynamic stability since negative real roots correspond to decaying responses. The roll and spiral modes appear as real poles in the negative real axis, while Phugoid, Dutch roll and short period appear as complex conjugate pairs with negative real parts, confirming oscillatory but dynamically stable behavior. Cruise points shift further left compared to takeoff, reflecting increased damping at higher dynamic pressure.

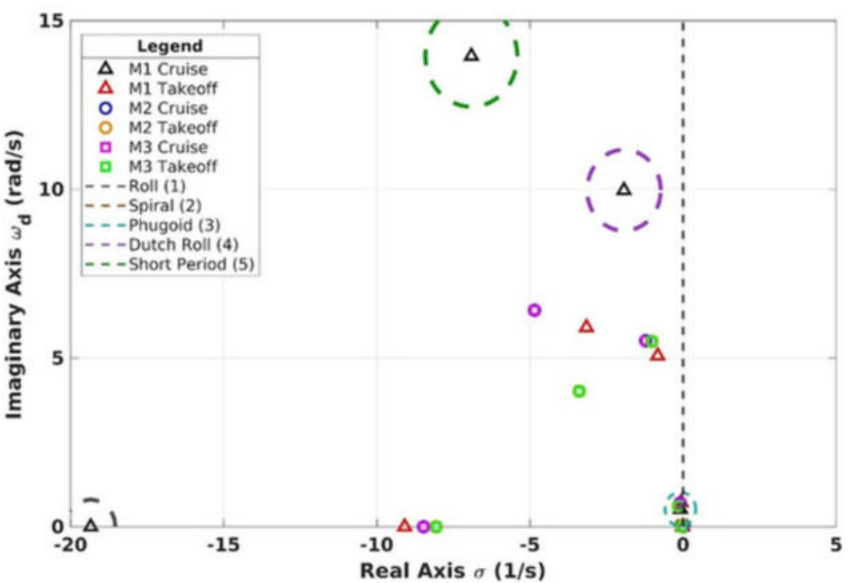


Figure 4.19: Root Locus for dynamic stability modes during takeoff and cruise

Table 4.14: Dynamic Stability Parameters during M2 (Cruise/Takeoff Values)

Mode		$\xi$	$\omega_n$	$\xi^* \omega_n$	Time to half amplitude [s]
1	Roll	-	9.1884 / 6.5884	9.1884 / 6.5884	0.0754 / 0.1052
2	Spiral	-	0.2503 / 0.3675	-0.2503 / -0.3675	2.7690 / 1.8857
3	Phugoid	0.0697 / 0.0299	0.9385 / 1.1146	0.0654 / 0.0334	10.5949 / 20.7637
4	Dutch Roll	0.0878 / 0.0486	5.3893 / 5.3009	0.4733 / 0.2577	1.4640 / 2.6891
5	Short Period	0.5821 / 0.5755	7.4448 / 5.9937	4.3339 / 3.4492	0.1599 / 0.2009

Table 4.15: Dynamic Stability Parameters during M3 (Cruise/Takeoff Values)

Mode		$\xi$	$\omega_n$	$\xi^* \omega_n$	Time to half amplitude [s]
1	Roll	-	7.7858 / 5.8470	7.7858 / 5.8470	0.0890 / 0.1185
2	Spiral	-	0.2945 / 0.4031	-0.2945 / -0.4031	2.3529 / 1.7192
3	Phugoid	0.0492 / 0.0230	1.1368 / 1.2250	0.0559 / 0.0282	12.3915 / 24.5901
4	Dutch Roll	0.0972 / 0.0488	5.0147 / 4.7182	0.4876 / 0.2301	1.4212 / 3.0116
5	Short Period	0.5675 / 0.6371	8.4102 / 5.5723	4.7732 / 3.5501	0.1452 / 0.1952

In the aforementioned table, the values are listed in the format cruise/takeoff allowing direct comparison between the conditions at velocity 846.46 in/s and 590.55 in/s respectively. The roll mode is the fastest and most stable with decay rates of 9.19/6.59 s<sup>-1</sup> for Mission 2 and 7.79/5.85 s<sup>-1</sup> for mission 3 resulting in very short half-amplitude times. The short period mode remains well damped with  $\zeta \approx 0.57\text{--}0.64$  and high frequencies of 5.6–8.4 rad/s, confirming strong pitch stiffness. Phugoid mode is lightly damped with  $\zeta = 0.02\text{--}0.07$ , frequency of about 1 rad/s and long decay times of 10–25 s. Dutch roll damping indicates acceptable lateral oscillatory stability. The Spiral mode has very small real parts (0.25–0.40 s<sup>-1</sup> magnitude), meaning it is extremely slow; even if marginally unstable in certain conditions, the long time constant (~2 s) makes it operationally manageable.

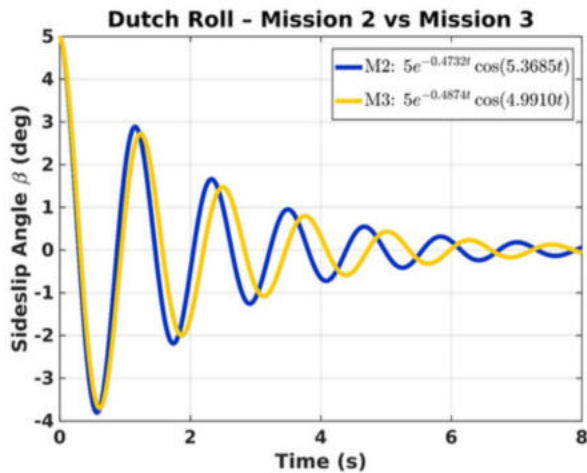


Figure 4.20: Dutch Roll Response (M2 vs M3)

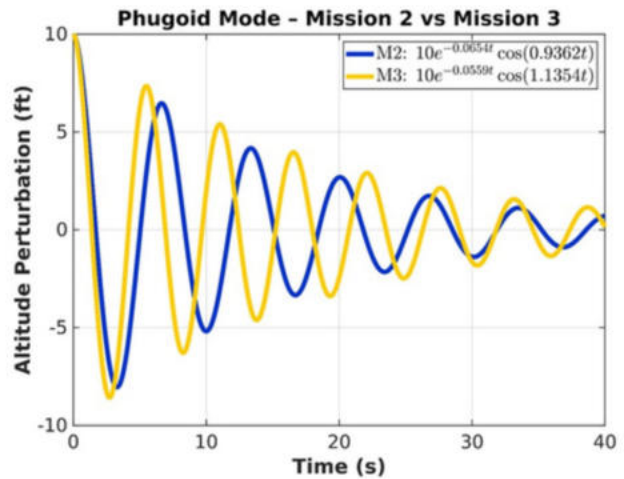


Figure 4.21: Phugoid Mode Response (M2 vs M3)

The phugoid is lightly damped ( $\zeta \approx 0.02\text{--}0.07$ ) with low decay rates ( $\zeta\omega_n \approx 0.03\text{--}0.07$  s<sup>-1</sup>) and a long time-to-half amplitude of ~10–21 s confirming slow energy dissipation. Dutch roll shows moderate damping ( $\zeta \approx 0.05\text{--}0.10$ ) with  $\zeta\omega_n \approx 0.23\text{--}0.49$  s<sup>-1</sup> and rapid convergence within ~1.4–3 s. Additionally, the spiral mode has a small positive ( $\sigma \approx 0.25\text{--}0.40$  s<sup>-1</sup>) real eigenvalue making it weakly unstable, but the time-to-double (~1.7–2.8 s) remains slow enough for the pilot's corrective input.

## 4.5 CFD Analysis

### 4.5.1 Fuselage

CFD analysis of the fuselage was performed in ANSYS Workbench 2024 R1 [10] to provide aerodynamic inputs for mission performance estimation. A C-type external flow domain was constructed to capture freestream development and wake behavior. Meshing was carried out using the Fluent watertight meshing workflow. A baseline global element size on the order of fuselage length/200 was selected, with local refinement and proximity sizing applied near the nose and aft taper where stronger velocity and pressure gradients were expected. Convergence was assessed through residual reduction and stabilization of force coefficients.

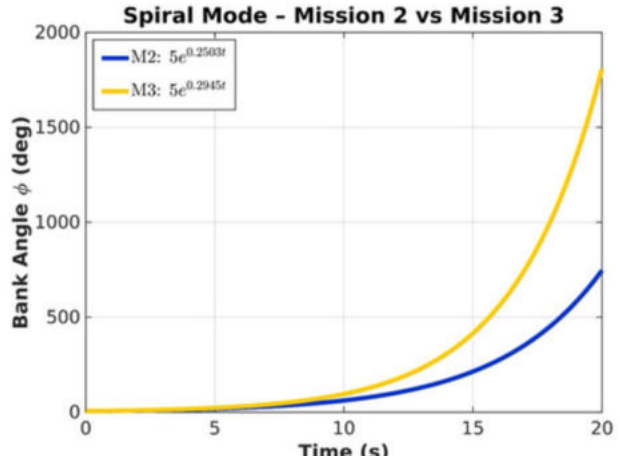
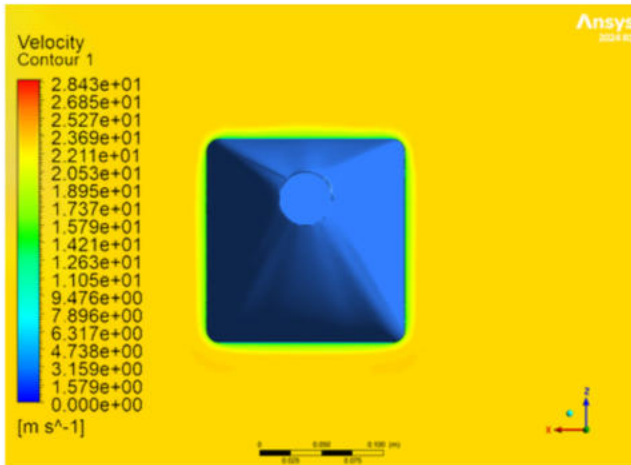
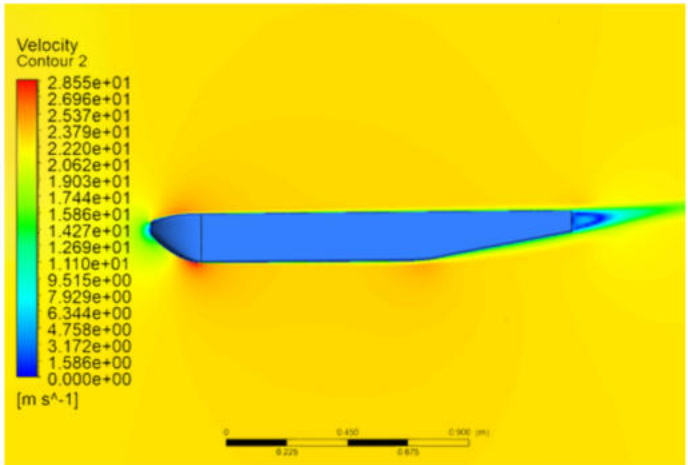


Figure 4.22: Spiral Mode Response (M2 vs M3)

Velocity contours (refer to figures 4.23 and 4.24) show a stagnation region at the nose, followed by smooth acceleration along the forebody and largely attached flow over the fuselage length. The gradual aft taper promotes controlled pressure recovery, producing a confined wake and limiting pressure drag. The front-view contours indicate near-uniform external flow with high gradients restricted to the near-wall region, confirming a thin attached boundary layer and absence of large separation zones.



**Figure 4.23:** Fuselage velocity contour (frontal view)



**Figure 4.24:** Fuselage velocity contour (lateral view)

The integrated forces yielded fuselage drag values on the order of 1 N and drag coefficients ranging from 0.13–0.18 across the evaluated mission conditions. The variation in  $C_d$  between missions is consistent with differences in operating speed and Reynolds number, which alter skin-friction contribution and pressure recovery behavior. Lift coefficients were small and negative, which is expected for an asymmetric fuselage aligned at zero angle of attack. The small negative lift arises from minor pressure asymmetries and is negligible.

**Table 4.16:** CFD based aerodynamic parameters of fuselage

Fuselage	Mission 1	Mission 2	Mission 3
$C_L$	-0.18	-0.255	-0.202
$C_D$	0.131	0.183	0.147
L (lbf)	-0.296	-0.419	-0.332
D (lbf)	0.216	0.301	0.241

The obtained coefficients fall within typical ranges for slender bodies at low Mach number and validate the adopted fuselage shaping strategy for drag minimization. These drag values were subsequently used in mission-level sizing and performance calculations, providing a consistent aerodynamic basis for configuration refinement.

#### 4.5.2 Wing

CFD analysis of the wing was performed to evaluate lift generation, drag characteristics, and tip-flow behavior under representative takeoff and cruise conditions.

A stagnation region is observed near the leading edge, followed by strong acceleration over the upper surface, producing a low-pressure region responsible for lift generation. The pressure differential between the upper and lower surfaces is clearly reflected in the velocity gradients. The smooth velocity recovery toward the trailing edge indicates a largely attached flow.

Frontal-view contours illustrate the formation and downstream evolution of the wingtip vortex. At approximately 0.75c, the onset of spanwise flow toward the tip is visible, driven by the pressure difference between the lower and upper surfaces. Further downstream, a concentrated vortex core is observed, confirming the roll-up of the tip vortex.

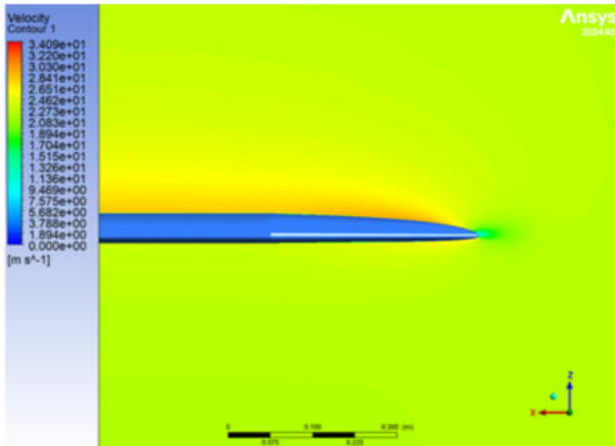


Figure 4.25: Wing velocity contour (frontal view)

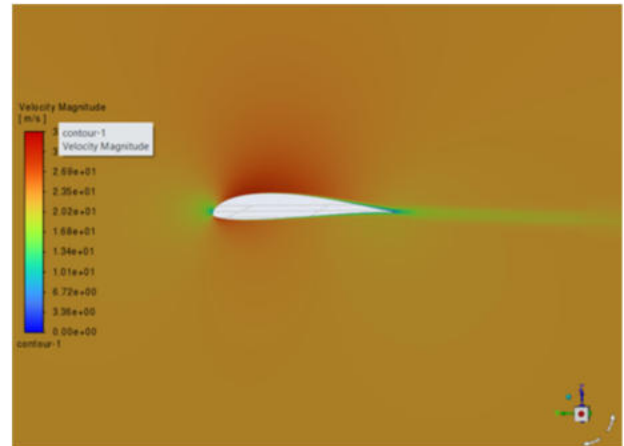


Figure 4.26: Wing velocity contour (lateral view)

The computed aerodynamic coefficients align with expected trends across mission segments. During takeoff conditions, lift coefficients range from approximately 0.82 to 1.25, reflecting increased camber and effective angle of attack due to deployment of flaps. The corresponding drag coefficients ( $\approx 0.26\text{--}0.39$ ) are higher due to both increased pressure drag and induced drag, which is typical for wings with plain flaps. In cruise conditions at moderate angle of attack and zero flap deflection, lift coefficients reduce to approximately 0.34–0.49 while drag coefficients drop significantly to around 0.045–0.063, leading to improved L/D ratio.

Table 4.17: CFD based wing aerodynamic parameters at takeoff and cruise

Mission	Case	AoA( $^{\circ}$ )	Flap ( $^{\circ}$ )	$C_L$	$C_D$
Mission 1	Takeoff	20	30	0.824	0.256
	Cruise	8	0	0.344	0.045
Mission 2	Takeoff	20	30	1.245	0.386
	Cruise	8	0	0.489	0.063
Mission 3	Takeoff	20	30	0.973	0.308
	Cruise	8	0	0.387	0.05

Variations among the missions are physically justified by differences in required lift levels and operating conditions. Missions requiring higher payload or lift naturally show higher  $C_L$  and  $C_d$ , while lighter or lower-lift missions exhibit reduced coefficients. The trends remain monotonic and aerodynamically consistent, which supports the reliability of the simulations.

#### 4.6 Estimated Aircraft Mission Performance

Puspak's performance parameters were calculated analytically using empirical methodologies from Roskam, with AVL [2] simulations utilized to verify aerodynamic coefficients.

Table 4.18: Preliminary design performance parameters

Performance Parameters	Mission 1	Mission 2	Mission 3
$C_{L_{max}}$	1.20	1.20	1.20
$C_{L_{cruise}}$	0.19	0.26	0.63
Weight (lbf)	8.80	9.36	11.00
W/S (lb/in sq)	0.01	0.01	0.02
e	0.90	0.90	0.90
Battery Weight (lbf)	1.51	1.19	1.51
$V_{cruise}$ (ft/s)	87.60	103.88	72.52
$V_{stall}$ (ft/s)	34.97	36.06	39.10
$V_{turn}$ (ft/s)	49.45	51.00	55.29
Turn Load Factor	2.00	2.00	2.00
Turn Radius (ft)	79.60	79.60	79.60
360 deg Turn time (s)	10.07	9.76	9.00
Scores Estimated	1	892	68

## 5. Detailed Design

The Detailed Design phase finalized Pushpak's structural, aerodynamic, and subsystem configurations to ensure optimal and reliable mission performance. Building upon the parameters established during Preliminary Design, the team may refine the airframe's structural architecture to a carbon fiber composite build to achieve significant weight reduction.

### 5.1 Dimensional Parameters

The characteristic dimensional parameters used for the design of Pushpak are listed in Table 5.1. Each subsystem listed is explored in detail in the following sections

**Table 5.1:** Dimensional Parameters

Wing		Motor	
Airfoil	SD7062	Model	T-MOTOR AM670
Span	5 ft	Effective KV	480
MAC	1.142 ft (0.384 m)	Max. Power	2700 W
Planform Area	812.3616 sq. in	Peak Current	110 A
AR	4.43	Internal Resistance	12 mΩ
Taper Ratio	0.5	Weight	0.9173 lb
Taper Position	1 ft (from center)	Propeller	
Static Margin	M1	23.83%	Manufacturer
	M2	22.53 %	Diameter
	M3	21.29%	Pitch
Fuselage		Avionics	
Total Length	56.082 in	Receiver	FlySky FS-iA10B
Nose Length	7.143 in	Servos	JR PROPO
Tail Length	5.795 in	ESC	T-MOTOR AM116A
Width	6.236 in	Fuse	Blade Style 100 A
Height	6.433 in	Battery	
Fuselage aft taper	10.255 deg	Propulsion	6S 4200 mAh
Tail			6S 3800 mAh
Airfoil	NACA0012	Avionics	
Horizontal Span	27.598 in	Passengers	
Horizontal root Chord	8.661in	Maximum Quantity	30
Horizontal tip Chord	5.1968 in	Total Weight	1.3125 lb
Vertical Span	11.4922 in	Cargos	
Vertical root Chord	8.661 in	Maximum Quantity	10
Vertical tip Chord	5.1968 in	Total Weight	3.75 lb
Planform Area	189.596 sq. in	Banner	
Incidence Angle	39.471361 deg	Dimensions	17 ft x 3.4 ft
Tail Arm	31.511 in	Deployed Distance from Aircraft	9.3 ft
		Material	Ripstop Nylon

## 5.2 Structural Characteristics

### 5.2.1 Layout and Design

The aircraft's structural layout was designed to manage critical flight forces by establishing direct load paths to the major load-bearing components. The loads can be categorized as follows:

**Inertial Loads:** These represent the forces acting on the aircraft structure due to motor thrust, reaction torque, and sustained vibrations at the maximum thrust condition. These loads are primarily handled by the fuselage structure, through two reinforced longerons from motor mount.

**Aerodynamic Loads:** These comprise the lift, drag, and moment forces generated by the lifting surfaces and the banner during flight. Primarily includes the significant parasite drag induced by the wing and towed banner. The wing structure, including the primary spars, ribs, and shear webbing manage these loads.

**Ground Loads:** These are the impact forces and taxiing loads transmitted through the undercarriage during landing at maximum aircraft weight. These loads are primarily handled by the landing gear structure and transferred to longerons through bulkheads from landing gear reinforcement.

### 5.2.2 Flight Envelope

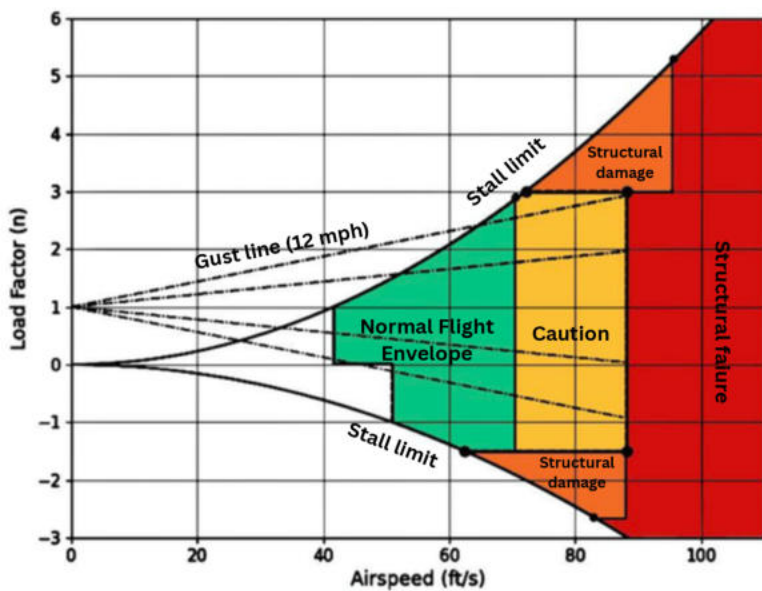


Figure 5.2: Flight Envelope of Pushpak for M2

## 5.3 System and Subsystem Design Implementation

The subsystems and components that make up the plane include the propulsion system, fuselage, motor mount, wing, empennage, banner deployment, banner release mechanism, passenger, cargo, landing gear, and avionics.

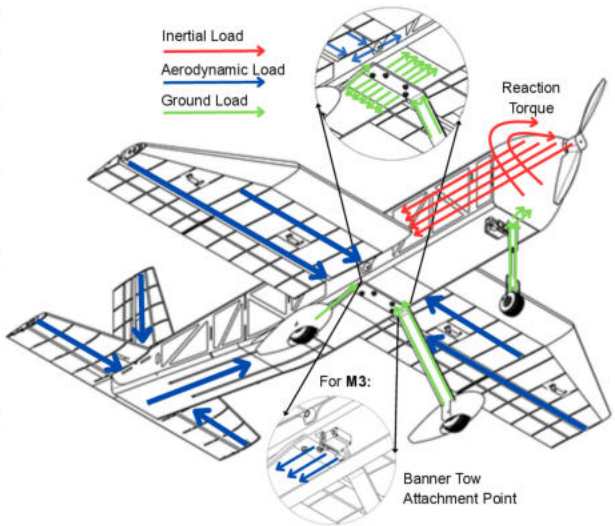


Figure 5.1: Aircraft Loads

The operating limits of the aircraft are defined by its aerodynamic and structural characteristics. Figure 5.2 displays these limits in a V-n diagram. The analysis utilizes CS-23/FAR-23 airworthiness standards [11], specifically examining the critical loading case of Mission 2. The maximum allowable load factor is limited by either the maximum lift coefficient to prevent stall or by the structural load limit of +3g and -1.5g. The never-exceed velocity is set to 25% higher than the maximum cruise velocity to avoid flutter and buffering. Furthermore, the analysis also includes gust load factors based on standard vertical gust wind 12 mph simulating wind conditions of Wichita. The analysis confirms that at Cruise Speed, the aircraft can withstand these gusts without exceeding the limit load factor.

### 5.3.1 Motor Mount Assembly and Nacelle

The propulsion system is mounted on the front of the fuselage using an firewall assembly (shown in Drawing package sheet 3), designed to distribute the thrust loads through the fuselage longerons and bulkheads, and mitigate vibrations. The assembly consists of a 0.16 in. thick bass plywood mounting plate with four holes to accommodate the fasteners for the motor. The mounting plate is mated orthogonally to a longitudinal torque box using T-slot joints to maximize its rigidity. By, extending the mounting structure aft, into the fuselage, the localized bending moments due to the overhang of the propulsion system are mitigated.

To prevent wood fibers from getting crushed and bearing failure occurring due to the high torque from the propulsion system, wide-area steel washers and nuts are used. The firewall assembly is further structurally coupled to the passenger deck, utilizing it as a horizontal shear web to increase torsional rigidity. To minimize the parasitic drag penalty caused by the bluff-body profile, the entire mounting assembly is enclosed inside a custom fabricated carbon fiber nacelle, optimized from CFD analysis. The nacelle is secured to the firewall periphery using four screws. It has a hinged hatch on the top surface to permit removal of the battery for inspection, maintenance and shipping purposes. The threaded fasteners interface with steel blind nuts embedded in the plywood bulkheads of the fuselage.



Figure 5.3: Nacelle

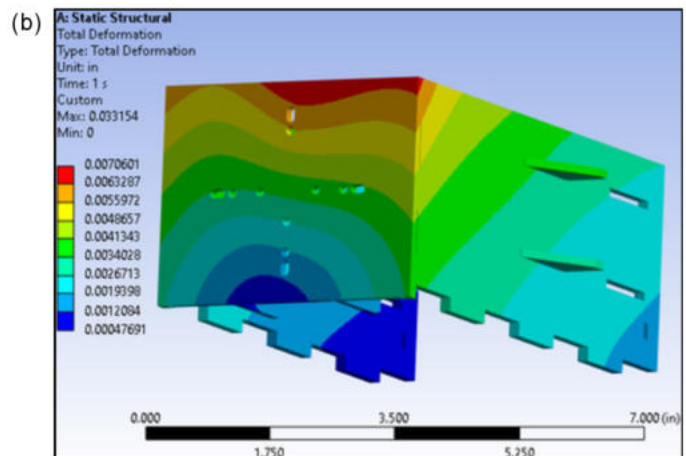
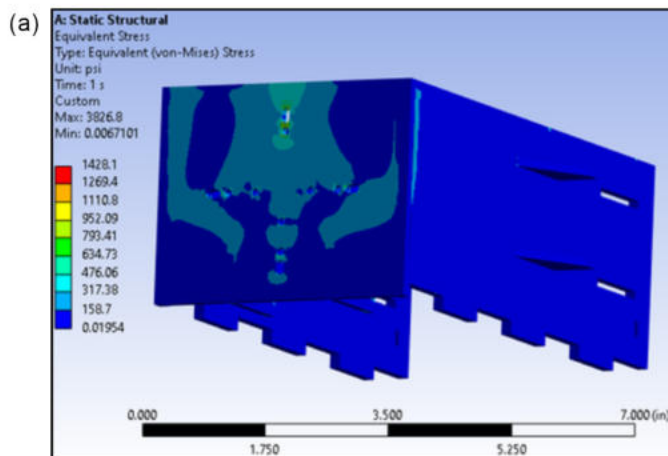


Figure 5.4: FEA of the motor mount assembly: (a) Stress (b) Deformation

A Finite Element Analysis (FEA) was conducted in ANSYS Workbench 2023 R2 [3] to validate the structural integrity of the motor mount and torque box assembly, with close attention to the stress concentrations at holes for the fasteners to ensure that bearing failure is prevented, as well as on the interlocking notch roots, where cleavage stresses are maximum. The carbon fiber nacelle was treated as a non-structural aerodynamic fairing and was excluded from the stiffness calculation. The bass plywood, birch plywood and balsa were modelled as orthotropic materials in accordance to the USDA Wood Handbook [12]. The assembly was tested under a combined load case, simulating a maximum throttle, pull-up maneuver at 3G. The results showed stress concentration at the fastener holes with maximum principle stress of 1428.62 psi, which is less than the breaking stress of bass plywood 8702.26 psi, giving a factor of safety of 6.1 which was believed to be excessive. This led to the conclusion that lightening holes could be cut into the torque box while maintaining sufficient FoS in the next iteration.

### 5.3.2 Fuselage

The fuselage is 56.082 in long and has a cross-section of 6.236 in x 6.433 in which tapers towards the tail. It is designed to accommodate the avionics, 30 passengers (ducks) on its upper deck, and 10 cargo units (hockey pucks) in the bottom cargo hold. From CFD analysis in Section 4.5.1 it was determined that though a rectangular cross section would increase the drag experienced by the aircraft, given the constrained budget, material availability and lack of experience, the benefits in design and construction of a simpler rectangular cross section would outweigh the benefits of a round cross section.

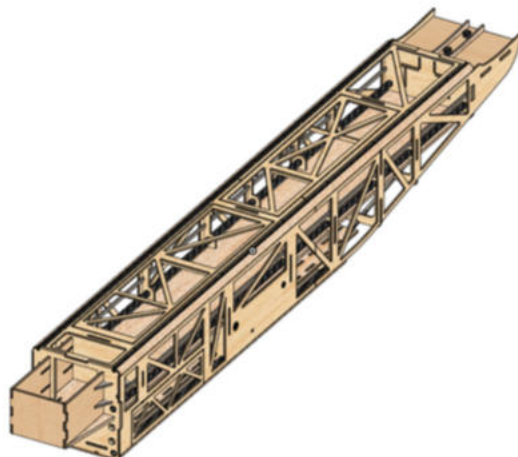


Figure 5.5: Fuselage Structure

The volume of the fuselage is divided by a rigid, continuous deck, made of composite sandwich of a 0.12 inch balsa core with carbon fiber face sheets, which was found to be lighter in weight than a birch ply platform of the same dimensions even with lightening holes cut into it. The deck has a vertical divider in the center joined to it using tab-and-slot joints as a rail for the duck restraint mechanism to clamp down on. For mission 3, a banner deployment and release mechanism is attached to the undersurface as described in Section 5.3.8. At the front of the fuselage is the motor mount assembly and the nacelle which integrates with the rest of the fuselage through the torque box. At the aft end of the fuselage is the empennage assembly, described in Section 5.3.4. The deck attaches to the rear bulkheads of the fuselage and has additional supports to mitigate bending due to the moments generated by the tail.

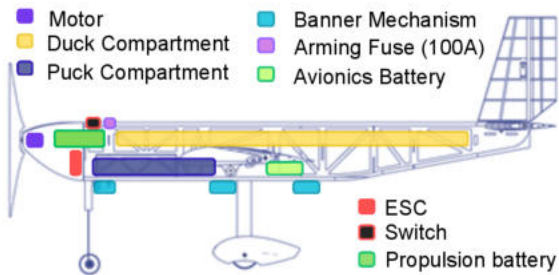


Figure 5.6: Volume Distribution Diagram of Pushpak

The fuselage utilizes a built up semi-monocoque construction designed to withstand 3G loading. The primary load bearing structure consists of 6 carbon fiber longerons (2 of which are 0.2 in x 0.2 in square pultruded carbon fiber rods and 4 round carbon fiber tubes with an outer diameter of 0.39 inch and thickness of 0.08 inch and 0.16 inch for 2 rods each) which also maintain the outer mold along with 0.2 in x 0.12 in balsa stringers. The longerons mainly take the tensile loads at the top of the fuselage and compressive loads at the bottom, particularly the impact of landing. Eight birch plywood bulkheads are used throughout the fuselage to distribute the loads from the longerons. The bulkheads near the motor mounting location, wing mounting location and tail mounting platform are reinforced by laminating two 0.12 inch thick birch plywood layers to handle thrust and empennage loads. The remaining 4 formers and the sidewalls are made of single layers of 0.12 inch thick birch plywood. The sidewalls use interlocking tab-and-slot joints to mate with the transverse bulkheads, ensuring a perfectly aligned assembly without the need of a separate jig.

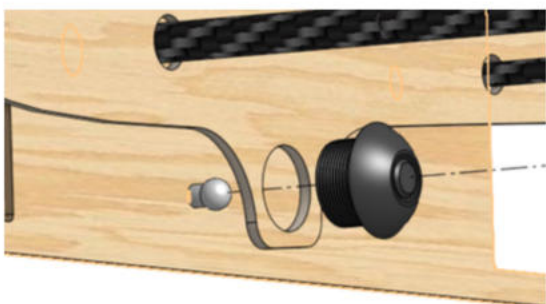


Figure 5.7: Quick Release Pin

Lightening holes in the sidewalls leave behind diagonal member, effectively transforming them into integral Warren trusses to carry shear forces between the formers. Wing integration is achieved by transverse telescopic carbon fiber tubes penetrating the sidewalls, allowing for rapid wing disassembly and compact transportation. These tubes are clamped to the passenger deck using custom fabricated glass fiber pipe clamps and the ribs at the wing root lock into to the side wall using quick release pins to prevent them from sliding out during flight.

The passenger deck interlocks with the bulkheads and formers as well as the torque box for the motor and the empennage, preventing any horizontal or vertical motion. The entire assembly is covered in a monocote skin to reduce skin friction drag. The floor of the fuselage is made in a similar manner to the passenger deck, with an additional layer of 0.12 inch birch plywood at the landing gear and wing mounting locations for reinforcement. The upper surface of the fuselage has 2 hatches, one ahead and one behind of the wing attachment location to allow quick and easy access to load the passenger ducks, along with another hatch in the side wall aft of the motor mount for loading the hockey pucks in a manner that minimizes the disturbance in the CG location between missions. The hatches utilize PVC hinges and are locked closed during flight using spring loaded screws inserted in the flaps which interface with t-nuts on the surface. FEA simulations were conducted to validate its structural integrity at 3G loads for M2 and 5G for M1 and M3 (Table 5.2) configurations. For the M3 analysis, the banner drag obtained from wind tunnel testing (refer to Section 8.1) was applied at the mounting point of the aircraft with a snatch factor of 2.0, in accordance to FAA AC 43.13-2B 12, Chap. 8) [13].

**Table 5.2:** Fuselage FEA Results

Loading Condition	FoS	Deflection (in)
M1 (5G)	5.23	0.03
M2 (3G)	5.34	0.04
M3 (3G)	5.34	0.05

### 5.3.3 Wing

The wing features a high-stiffness dual-spar, semi-monocoque construction with a planform which transitions from a rectangular inboard section of 15.08 inch chord length, to a tapered outboard section at 0.4 semi span. The airfoil is SD7062, selected based on the airfoil selection analysis done in Section 4.3.1. The 5-foot span is divided into two halves that mate to the fuselage center section to reduce the cost of long distance shipping. Bending loads are carried by two 0.08 inch thick carbon fiber round tubes of outer diameters 0.39 inch and 0.55 inch the front and aft of the wings respectively. These slide into telescopic carbon fiber tubes protruding from the fuselage at the wing roots for rapid assembly without compromising structural integrity by transferring root bending moments through the fuselage structure without inducing localized point loads on the skin. They are locked in place using quick release pins as described in Section 5.3.2.

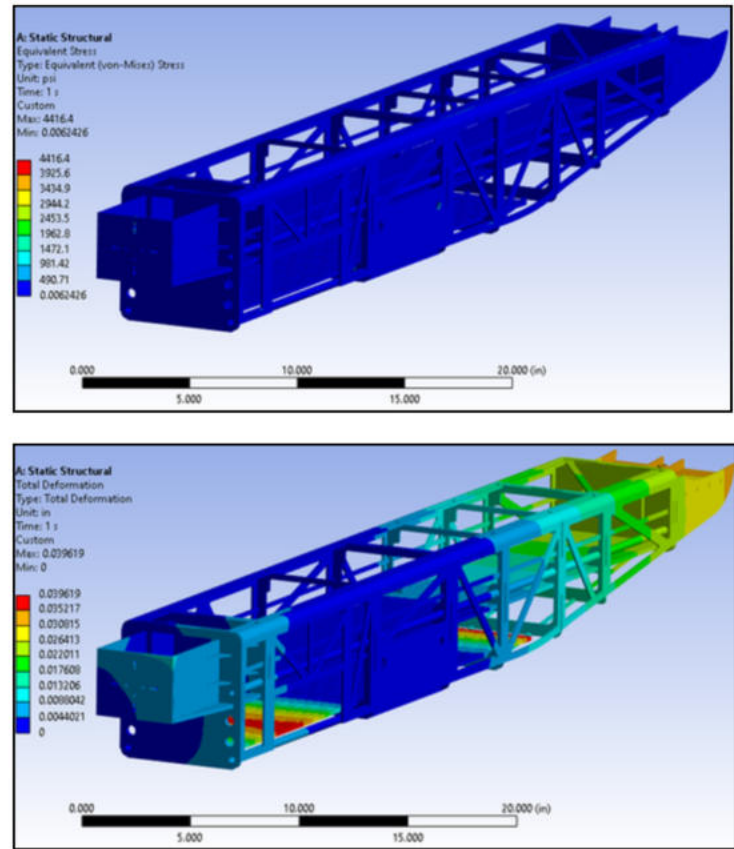


**Figure 5.8:** FEA results of the fuselage in M2 configuration under 3G loads showing stress and deformation

The FoS from the results was considered beyond ample to account for any material non-uniformities in the balsa, birch plywood and bass plywood and showed that the fuselage could handle more aggressive maneuvers without structural damage. However, this led to the conclusion that a significant portion of the birch ply structure of the fuselage could be replaced with bass plywood to reduce the weight of the structure while maintaining sufficient MOS.

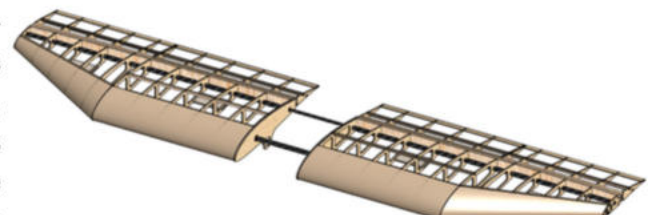


**Figure 5.9:** CAD model of the Wing

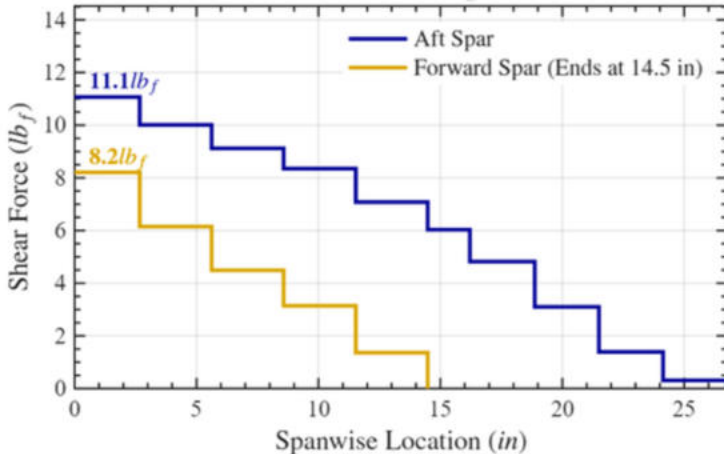


**Figure 5.10:** Wing Shear Force Diagram under 3G loads for M2 configuration

To reduce the weight of the wing while ensuring the same aerodynamic profile, the ribs were made of 0.12 inch medium density balsa to maintain the airfoil shape and prevent the skin from buckling, with 0.12 inch birch ply being used instead at high-stress hardpoints which include the wing root, wing tips and servo bays to prevent crushing under loads. A total of 11 such ribs of the SD7062 airfoil were used in each half of the wing. The entire wing is wrapped in a heat-shrunk Monocote covering serving as a skin with a 0.06 in balsa sheet underneath it at the leading edge for reinforcement and to increase the surface area for the adhesive of the film to act.

Pitch and roll authority are provided by simple flap and aileron surfaces, sized at 64.09 sq.in and 54.04 sq.in respectively on each side of the wing, from the stability and control analysis done in Section 4.3.2 and are constructed using a balsa skin supported by birch plywood ribs and birch stringers. To ensure robust hinge attachment, the wing trailing edge and control surface leading edges are reinforced with 0.39 inch thick balsa blocks contoured to wedges, providing an anchoring surface for the PVC hinges which allows for high deflection angles without mechanical interference. The servos for the control surfaces are mounted to custom composite hardpoints made of rectangular 0.12 inch balsa plates laminated with fiberglass.

These mounts are fitted into notches close to the wing undersurface between adjacent ribs. The balsa skin surrounding the attachment point of the plywood control horns is reinforced with a layer of carbon fiber to prevent them from getting ripped out or torn off.

$$\sigma = \frac{M \cdot y}{I} \quad \text{--- Equation 5.1}$$

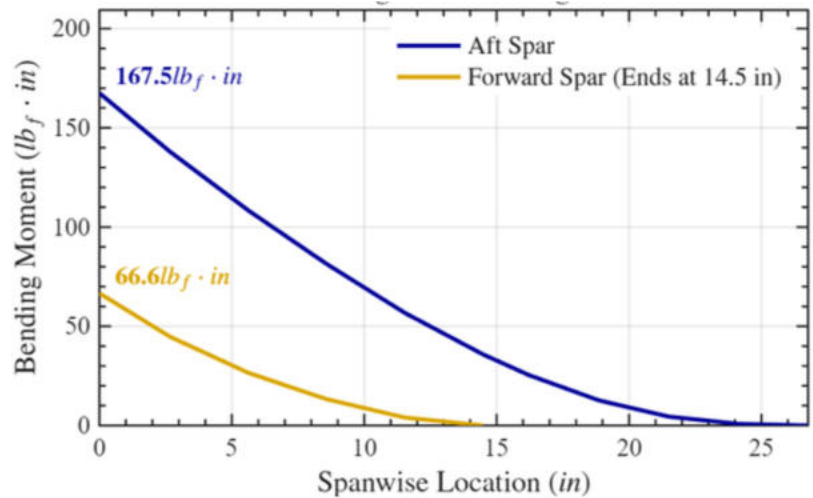


**Figure 5.11:** Wing Bending Moment Diagram under 3G loads for M2 configuration

**Table 5.3:** Wing FEA results

Loading Condition	FoS	Deflection (in)
M1 (5G)	1.67	1.3
M2 (3G)	1.77	1.22
M3 (5G)	1.61	1.34
GM Test	1.6	0.64

The structural sizing of the wing was driven by AVL[2] simulations. The wings were designed for a load case of 3G for the M2 requirements, with a conservative FoS of 1.5, establishing a 4.5G Ultimate Design Load for all failure analyses. Consequently, the Shear Force and Bending Moment Diagrams (Figure 5.10 and 5.11) were plotted at the 3G Limit Load for the M2 configuration and baseline sizing for the spars was calculated from the Euler-Bernoulli beam theory (Equation 5.1), the maximum allowable bending stress for CFRP being 87000 psi [14].

Final verification was done via Finite Element Analysis (FEA) at a 5G load for M1 and M3 and 3G load for M2 (Table 5.3), as well as a case in which the plane was lifted using its wing tips, in accordance with the ground mission testing requirements stipulated in the AIAA DBF 2026 rules [4] and Section 4.2.4. The simulations modeled the interaction between the carbon spars, the telescopic joiner, and the ribs. Results from the simulation confirmed that the dual-spar system successfully distributes bending stresses, with peak values in the carbon fiber components remaining well below the 87000 psi stress limit [14].

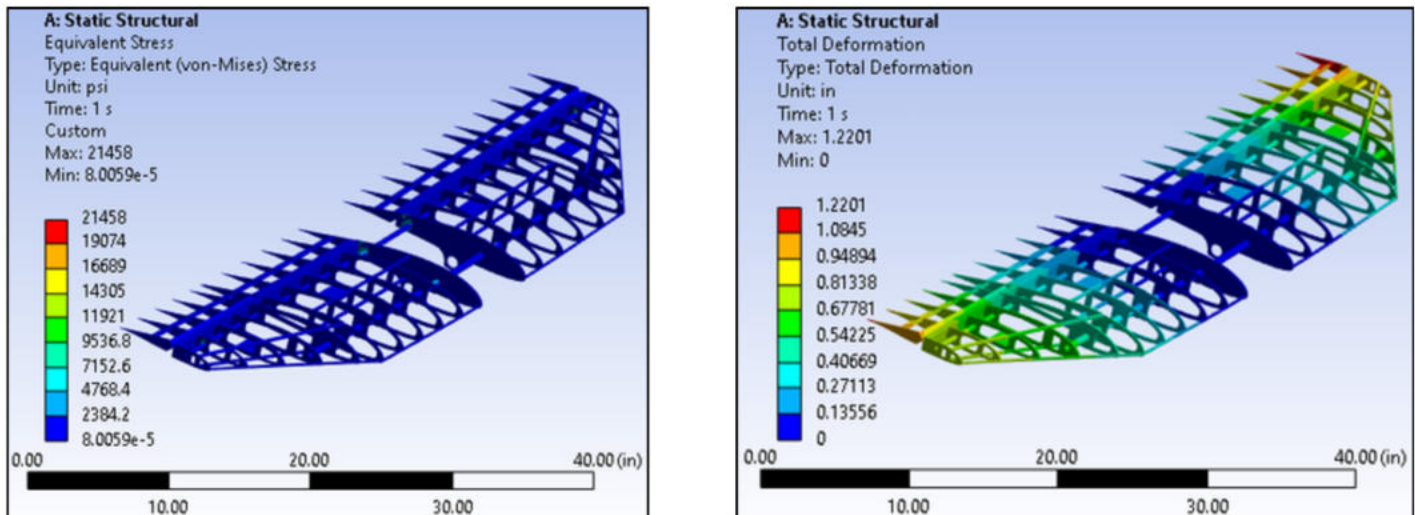


Figure 5.12: FEA results of the wing under 3G loads for M2 configuration of the fuselage

### 5.3.4 Empennage

The empennage features an inverted T-tail configuration, designed to prioritize ease of assembly and structural rigidity. The tapered vertical and horizontal stabilizers have a NACA 0012 airfoil and a mean aerodynamic chord of 6.89 in and 7.17 in respectively. Stabilizer and control surface sizing was done according to the tail authority analysis done in Section 4.3.2.3. A unified elevator surface was chosen to minimize weight by eliminating the need for a second servo. The architecture of the stabilizers and their control surfaces are similar to the wing in that they have birch ply ribs, carbon fiber spars (tubes of 0.472 in outer diameter and 0.039 in wall thickness) and, a 0.06 in balsa layer at the leading edge and a Monocote skin of the airfoil, whereas the control surfaces have birch ply ribs, pine wood stringer and 0.06 in balsa skin. Similar to the wing, the stabilizers have carbon fiber reinforced balsa mounts for the servos and the skin surrounding the control horns on the control surfaces are reinforced with a layer of carbon fiber bonded with epoxy to prevent them from getting torn off.



Figure 5.13: Empennage Assembly

The mid section of the horizontal stabilizer, where the vertical stabilizer mounts, is replaced with an extruded polystyrene foam (XPS foam) section with receiver tubes embedded in it for the spars of the vertical stabilizer to pass through. This provides a solid base for the vertical stabilizer to mount onto. As detailed in the fuselage section,

the horizontal stabilizer sits in a negative cut out of the airfoil at the aft platform of the fuselage. The ribs in contact with the side walls of the fuselage has extended tabs through which screws are inserted to fix the horizontal stabilizer in place.

The vertical stabilizer has two carbon fiber spars which protrude beyond the bottommost rib, pass through the receiver tubes of the horizontal stabilizer and tail mounting platform, and are fixed into place using transverse screws passing through them. The bottom part of the vertical stabilizer also has a contoured piece of XPS foam so that there are no gaps between it and the horizontal stabilizer. This effectively clamps the horizontal stabilizer down and also allows easy disassembly and reassembly for transport.

### 5.3.5 Main Landing Gear

The aircraft features a bow-type composite main landing gear chosen for its ability to dampen the impact of landing, and provide sufficient ground clearance for the propeller. It is 8.66 in tall and the wheel base is 18.50 in wide. It is mounted to the bottom surface of the fuselage, behind the CG of the aircraft for all three missions using M5 bolts. Wide area rubber washers are present between the landing gear and the fuselage to mitigate the large impulsive load during landings from being transmitted to the fuselage. Due a lack of experience of in-house composite manufacturing and limited time, the landing gear was commercially procured as a COTS component along with the fiber glass wheel fairings and rubber wheels.

The front landing gear consists of a carbon fiber shaft anchored to the fuselage base and the nose torque box. A spring steel frame extends from it to which the rubber wheel is mounted. This system was chosen to reduce the impact of landing.

FEA was conducted to analyze the suitability of the main landing gear. A conservative loading condition of 5G considering the MTOW weight of the aircraft was considered where the whole touchdown load was assumed to act on a single main wheel to investigate bad landing cases. The upper mounting face of the landing gear was set as fixed support in ANSYS to simulate a rigid fuselage attachment at the time of static structural analysis.

A carbon fiber composite having a breaking strength of 94,000 psi was used for the landing gear based on data sheet provided by the manufacturer. Results showed that the landing gear was suitable since the maximum von Mises stress was predicted to be 46,000 psi, resulting in a FoS of 2.04. The vertical deflection was 1.04 in which is less than the available ground clearance considering the propeller. A separate study of uniform landing case at a 5G load was also performed which showed a maximum von Mises stress of 21,207 psi and maximum vertical deflection of 0.72 in, giving a FoS of 4.43.

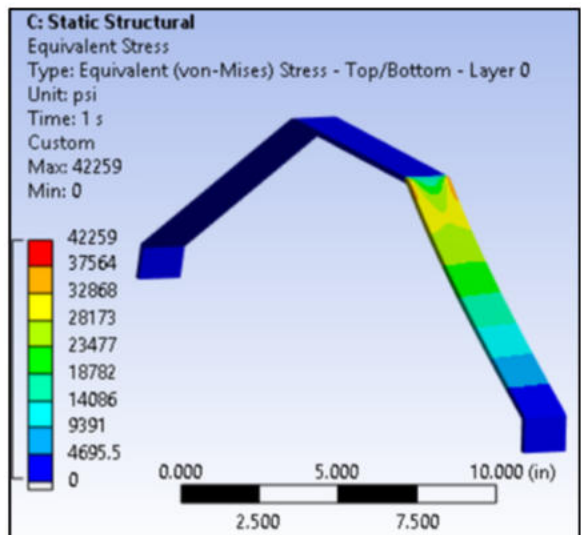


Figure 5.14: Main landing gear FEA showing stress under 5G load at MTOW

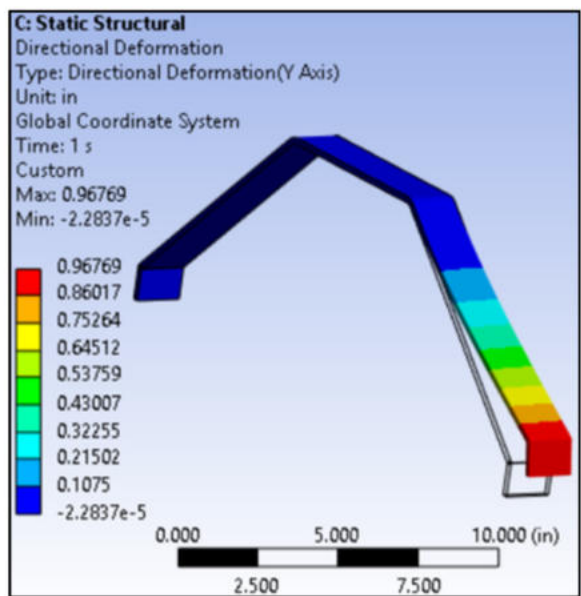


Figure 5.15: Main landing gear FEA showing vertical deflection under 5G load at MTOW

The passenger payload is configured in two forward-facing columns. The passenger compartment is fully isolated from other internal components using solid, fore and aft bulkheads. Loading is facilitated through the top access hatches of the fuselage.

The passenger restraint system was designed to securely accommodate passengers of varying sizes while minimizing loading time during GM. The core mechanism features a 'claw' bracket capable of securing four passengers simultaneously. Vertical constraint is provided by a locking pin that engages a serrated vertical rail integrated into the passenger deck. This multi-serrations allows the claw to be locked at adjustable heights to match specific duck geometries, effectively preventing upward movement or disengagement under negative-G maneuvers. The claw geometry was optimized for securely holding ducks of varying sizes, with a tight grip on the minimum width ducks according to the rules for AIAA DBF 2026 [4]. To ensure rapid manufacturability and minimize weight, the assembly is fabricated from 3D printed Polylactic Acid (PLA).



Figure 5.16: Passenger restraint mechanism

### 5.3.7 Cargo Restraint Mechanism



Figure 5.17: 3D printed hockey puck holder

The pucks will be loaded from the side access hatch of the fuselage into the cargo hold of the aircraft using 3D printed holders with PLA material in which a total of 10 pucks will be arranged in 5 compartments with stacks of two pucks each. The holders are designed to fit into the fuselage requiring a minimum-sized hatch, and are constrained from motion by the balsa decks above and below, and bulkheads in the front and back of the cargo hold. Once both holders are loaded and the hatch is closed.

### 5.3.8 Banner

For (M3), the aircraft is required to carry a banner in a stowed configuration, deploy it during flight, complete the required successful laps, and subsequently release the banner before performing a proper landing.

The tow release mechanism and fuselage hardpoint were sized in accordance with FAA AC 43.13-2B [13], designing for a limit load factor of 2.0 times the maximum measured banner drag from wind tunnel tests (refer to Section 8.1), to account for deployment snatch loads.

#### 5.3.8.1 Material

Based on the analysis in Section 3.4.2, Ripstop Nylon was selected as the final banner material. Ripstop Nylon showed significant structural strength and better fluttering behaviour, which directly improved the readability of the banner text during flight



Additionally, a nylon string with a diameter of 0.039 inch is selected to tow the banner. It is selected for high strength. The specific gauge was selected for its tensile strength and durability under continuous flight loads

Figure 5.18: Ripstop Nylon & Nylon String

### 5.3.8.2 Deployment Mechanism

The deployment system features a dual-point retention strategy to secure the Ripstop Nylon banner flush against the fuselage. The forward retention uses a high-torque MG 995 servo acting as a linear actuator, driving a locking rod through a custom green end-cap on the 0.39 inch hollow carbon fiber banner tube. This robust interface simplifies ground operations and withstands takeoff impacts. Complementing this is a rear claw mechanism actuated by a micro-servo near the tail, which grips the banner to prevent premature unfurling and serves as a pivot point during deployment to ensure the banner separates cleanly from the airframe.

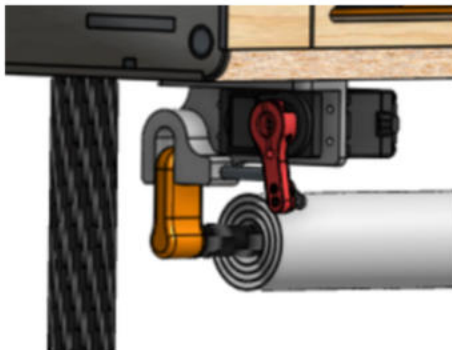


Figure 5.20: Deployment Cap for the banner



Figure 5.19: Linear Actuator System



Figure 5.21: 3D printed Claw for the banner

### 5.3.8.2 Release Mechanism

Distinct from retention, the release mechanism is positioned at the aircraft's Center of Gravity (CG) to manage the high dynamic loads of the towed banner without affecting flight stability. This system employs a second MG 995 servo driving a high-strength aluminum linear rod that anchors the towing tether loop. The aluminum construction is specifically selected to withstand the significant "snatch" impulse generated when the banner transitions to towed flight, ensuring the connection remains secure until the servo retracts for the final jettison prior to landing.

FEA was performed on the bass plywood reinforced base based on the drag values obtained from the wind tunnel testing (refer to Section 8.1) with a snatch factor of 2.0 [13] of the aircraft to determine whether it would experience bearing failure at the mounting holes of the tow hook. Results showed that the maximum von Mises stress of 55.92 psi which was well below the failure limit. It was deemed unnecessary to analyze the banner tow mechanism itself since it performed without failure in extensive wind tunnel testing for banner drag. Furthermore, the banner drag from wind tunnel testing, scaled by the snatch factor was less than the design limit of 11.24 lbf according to the manufacturer.

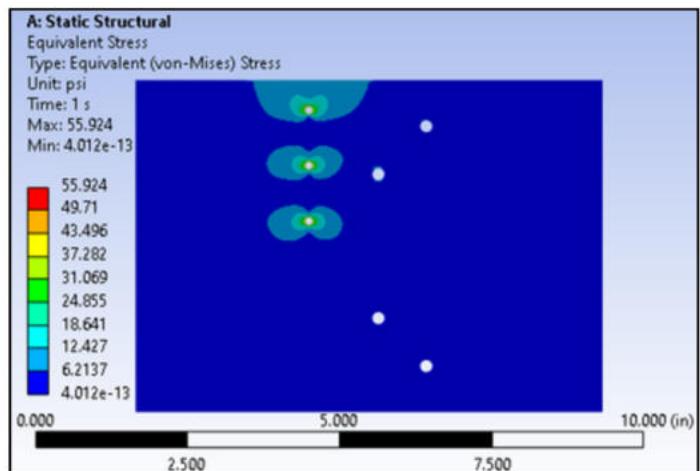


Figure 5.21: Reinforced Mounting Plate

### 5.3.9 Propulsion System

A detailed static thrust test campaign conducted with the T-Motor AM670 520KV demonstrated that the optimal motor-propeller configuration for both Mission 2 (M2) and Mission 3 (M3) is achieved using an 18x8 carbon-fiber propeller in combination with the manufacturer-recommended 116 A electronic speed controller (ESC).

This configuration provided the required thrust margins while maintaining acceptable electrical and thermal operating limits across the mission envelope. Battery consumption studies based on measured current draw and mission endurance requirements led to the selection of a 6S 3800 mAh LiPo battery for M2 and a 6S 4500 mAh LiPo battery for M1 and M3, allowing each mission to meet its energy requirements with adequate reserve. In accordance with competition safety guidelines, a 100 A inline fuse is installed between the battery and ESC, serving both as over-current protection and as an externally accessible arming plug.

### 5.3.10 Avionics

Figure 5.22 illustrates the wiring schematic of PUSHPAK, an emphasis was given on minimizing the wiring used and maintaining simplicity for faster replacement of components. An inline switch was inserted between the connection to the receiver (FSiA10B) and the avionics battery. RadioMaster TX16S was selected as the transmitter.

The torque requirements for all control surfaces were determined by calculating the aerodynamic hinge moment using maximum maneuver speed of 26.74 m/s for elevator, aileron and rudder and a specific flap extension velocity of 14.31 m/s to reflect realistic operational limits. Following Roskam's analytical methodology [9], the hinge moment coefficient  $C_h$  was derived from the slopes  $C_{ha}$  and  $C_{h\delta}$  corresponding to the SD7062 wing and NACA 0012 tail geometries. To incorporate linkage losses, a mechanical efficiency of 0.9 was incorporated.

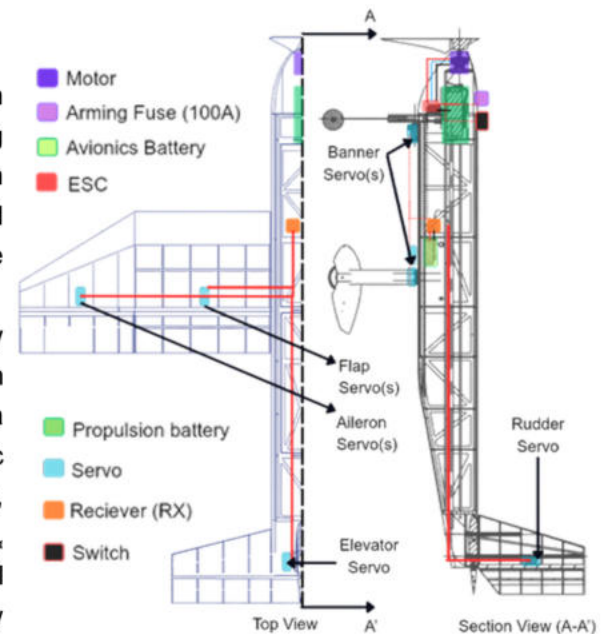


Figure 5.22: Wiring Diagram of Pushpak

A safety factor of 1.5 was used for primary light controls (aileron, elevator and rudder) and a factor of 2.0 was applied to the flap to compensate for the constant structural loads and friction association with high deflection extension.

Aerodynamic Hinge Moment:

$$H = q \cdot S_c \cdot c_c \cdot (C_{h\alpha} \alpha + C_{h\delta} \delta) \quad \text{--- Equation 5.2}$$

$$T_{\text{servo}} = \frac{q \cdot S_c \cdot c_c \cdot C_h \cdot L_{\text{arm}}}{\eta_{\text{linkage}} \cdot L_{\text{horn}}} \times SF \quad \text{--- Equation 5.3}$$

Table 5.5: Control Surface Servo Torque Sizing

Control Surface	Servo Used	Required Torque (oz-in)	Servo Torque (oz-in)
Elevator	JR PROPO S3911 2K V2(7.4 V)	187.40	208
Aileron	JR PROPO S3911 2K V2(6.6 V)	181.50	185.5
Rudder	JR PROPO S3415 2K JR	67.44	67.8
Flaps	PROPO S3415 2K	64.78	67.8

## 5.4 Weight and Mass Balance

Mass properties were obtained with CG locations measured from the nose using the body-axis coordinate system (X Forward, Z upward). The coordinate system used to model the CG is shown in Figure 5.23. Component weights and their XCG, ZCG positions were used to compute the total aircraft CG. Table 5.6 shows each component's mass and CG location with respect to this coordinate system. The empty aircraft (8.88 lb) sets the baseline CG near  $X \approx 2.0\text{--}2.2$  ft. Mission 2 (15.036 lb) shifts the CG slightly due to passengers and cargo while Mission 3 (11.208 lb) reflects the banner configuration. Ballast near  $X \approx 4.5$  ft was added to maintain CG within the required static margin.

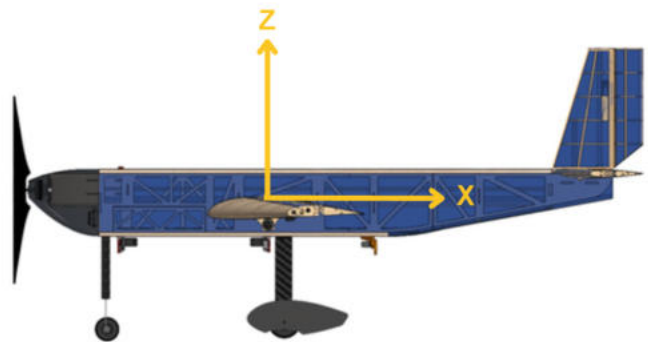


Figure 5.23: Aircraft Reference Axes

Table 5.6: Weight Balance

Category	Components	Weight (lb)	X-CG Location (in)	Z-CG location (in)
Structure	Nose Landing Gear	0.27	7.40	-8.37
	Main Landing Gear	1.247	20.95	-8.97
	Tail	0.419	54.49	2.96
	Wing	1.399	24.03	-1.98
	Fuselage	3.337	26.80	-1.21
	Aileron/Flap Servos	0.3	25.07	-2.45
	Rudder Servo	0.075	55.34	9.56
	Elevator Servo	0.075	54.70	1.70
	Banner Mech Linear actuator	0.298	9.20	-5.08
	Banner Mech. Claw Mechanism	0.078	32.82	-5.23
Empty Aircraft Structure	Structure (Str.)	7.117	26.94	-2.64
Propulsion	Propeller	0.066	-0.99	-0.07
	Receiver	0.003	24.02	-3.49
	T-Motor AM 670	0.937	1.08	-0.07
	ESC	0.273	6.24	-2.80
Battery	Main Battery	0.137	22.93	-0.55
	Avionics Battery	0.254	27.14	-3.31
Ballast	Ballast	0.331	53.99	0.01
Mission 1	Propulsion + Structure + Battery + Ballast	10.835	24.02	-2.15
Mission 2 Subsystems	Passengers (30)	1.312	29.79	-0.54
	Cargo (10)	3.751	25.99	-2.77
Battery	Main Battery	1.369	8.60	-0.48
	Avionics Battery	0.254	35.84	-3.31
Ballast	Ballast	0.331	54.19	0.02
Mission 2	Propulsion + Str. + M2 Subsys.+ Batt. + Ballast	15.471	24.35	-2.19
Mission 3 Subsystems	Banner	1.235	32.50	-6.57
Battery	Main Battery	1.369	16.36	-0.55
	Avionics Battery	0.254	26.02	-3.31
Ballast	Ballast	0.331	54.01	-0.06
Mission 3	Propulsion + Str. + M3 Subsys. + Batt. + Ballast	12.066	24.02	-2.62

## 5.5 Performance

### 5.5.1 Flight Performance

A point performance analysis was conducted to validate aircraft performance in all three missions. The key performance metrics are summarized in Table 5.7 and verified against propulsion data estimated using MotoCalc [7]. [15] was referred to perform the calculations.

The aircraft's stall speed,  $V_{stall}$ , was calculated for each mission weight using the maximum lift coefficient,  $C_{L_{max}}$ , ensuring a safe margin during all flight phases. Cruise speeds,  $V_{cruise}$ , were estimated based on the thrust-drag equilibrium for each mission, estimated using MotoCalc [7]. The maximum rate of climb,  $R/C_{max}$ , was determined by analyzing the excess power available, measured using  $k$  and  $C_{d0}$ , which is estimated using MotoClac.

Turn performance was analyzed assuming a steady, level turn. To determine the Turn Radius,  $R$ , and Time to turn, a limit load factor was assigned based on the maximum sustainable bank angle. Notably, the bank angle for Mission 3 is restricted to 55 deg to reduce the induced drag generated by the wings, preserving essential thrust to overcome the high parasitic drag of the deployed banner.

**Table 5.7:** Aircraft flight performance parameters for each mission

Performance Parameters	Mission 1	Mission 2	Mission 3
$C_{L_{max}}$	1.20	1.20	1.20
$C_{L_{cruise}}$	0.50	0.50	0.70
Weight (lbf)	10.98	15.30	12.21
W/S	0.01	0.02	0.02
e	0.90	0.90	0.90
Battery Weight (lbf)	1.62	1.62	1.62
Rate of climb (ft/s)	23.39	20.57	19.03
$V_{cruise}$ (ft/s)	62.81	70.54	51.01
$V_{stall}$ (ft/s)	36.94	43.61	38.96
$V_{turn}$ (ft/s)	88.83	99.76	63.62
Turn Load Factor	2.00	2.00	1.55
Turn Radius (ft)	70.77	89.25	67.84
360 deg Turn time (s)	7.08	7.95	8.00

A custom analytical performance model was developed to characterize equilibrium velocities across all missions. The thrust of the aircraft was plotted based on the static thrust and quadratic decay coefficients. This thrust profile was coplotted against the required total drag curves as shown in Figure 5.24. The maximum velocity is determined by finding the intersection between these curves. In mission 1, the aircraft flies in a clean configuration, achieving a baseline speed of 71 ft/s. Mission 2, the aircraft is heavily loaded, and the required lift is achieved by a maximum speed of 80 ft/s. In Mission 3, the large banner contributes to a large increase in parasite drag, limiting the maximum velocity to 55 ft/s, which remains well within the safe margin for towing.

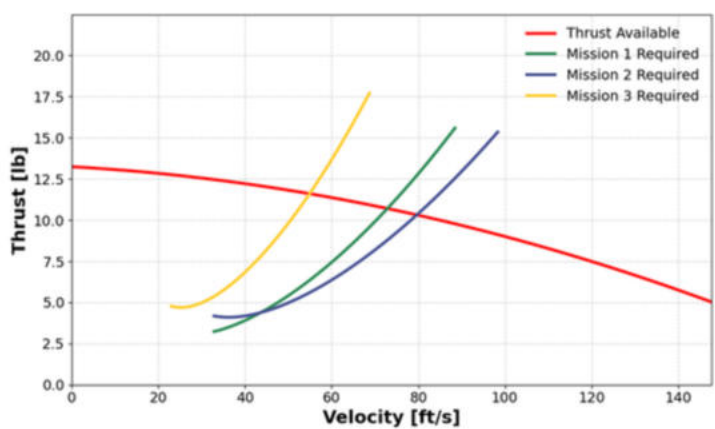


**Figure 5.24:** Thrust available and thrust required curves for each flight mission

### 5.5.2 Mission Performance

A time domain mission performance model in Figure 5.25 was developed to simulate the transient velocity response of the aircraft over the trajectory. Propulsion capability was first estimated using MotoCalc [7] to determine achievable cruise and turn speeds based on the selected motor-battery-propeller configuration. Instead of directly solving the nonlinear thrust-drag balance at every timestep, propulsion effects were embedded within a second-order velocity model which captures acceleration lag, aerodynamic resistance, and inertial response.

$$\ddot{V} + 2\zeta\omega_n \dot{V} + \omega_n^2 V = \omega_n^2 V_{cmd},$$

The natural frequency parameter represents effective thrust authority while the damping ratio governs smoothness of transitions between different speeds. Velocity and position are integrated simultaneously allowing mission time to emerge naturally from the aircraft's dynamic response.

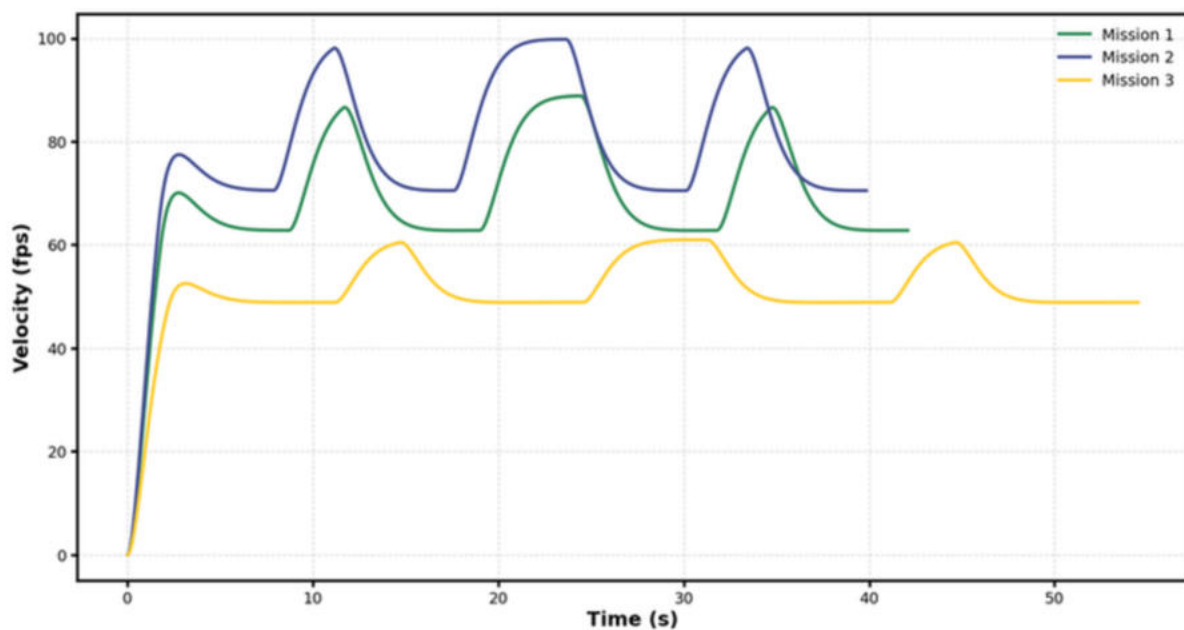
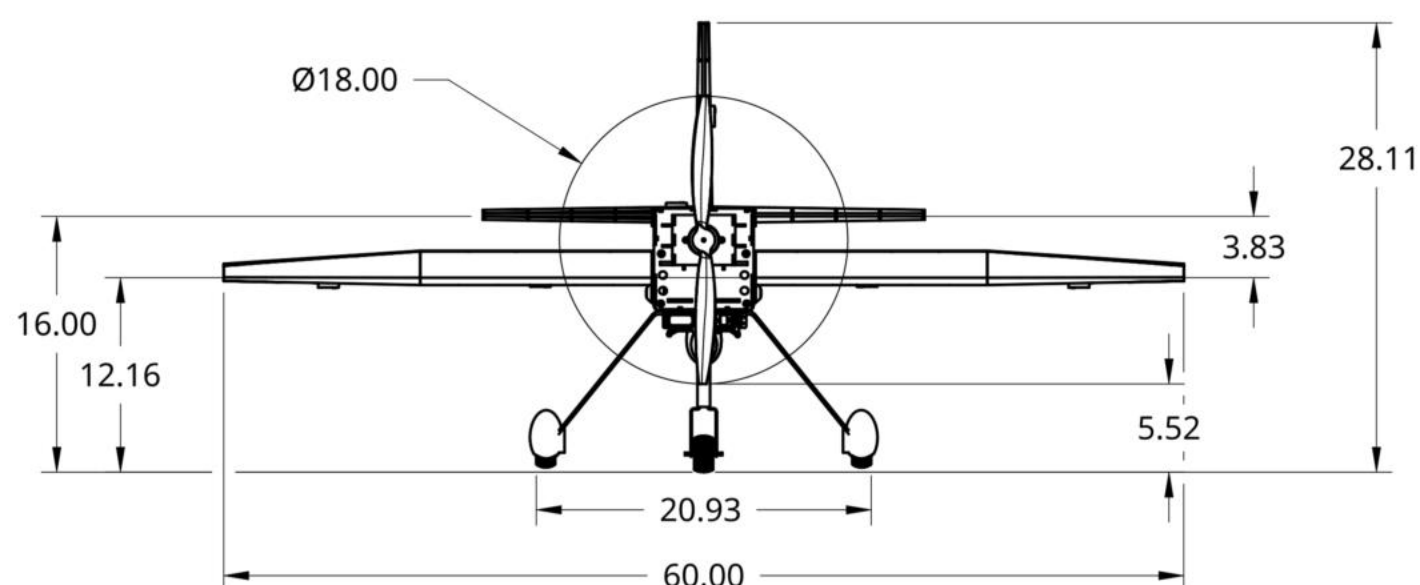
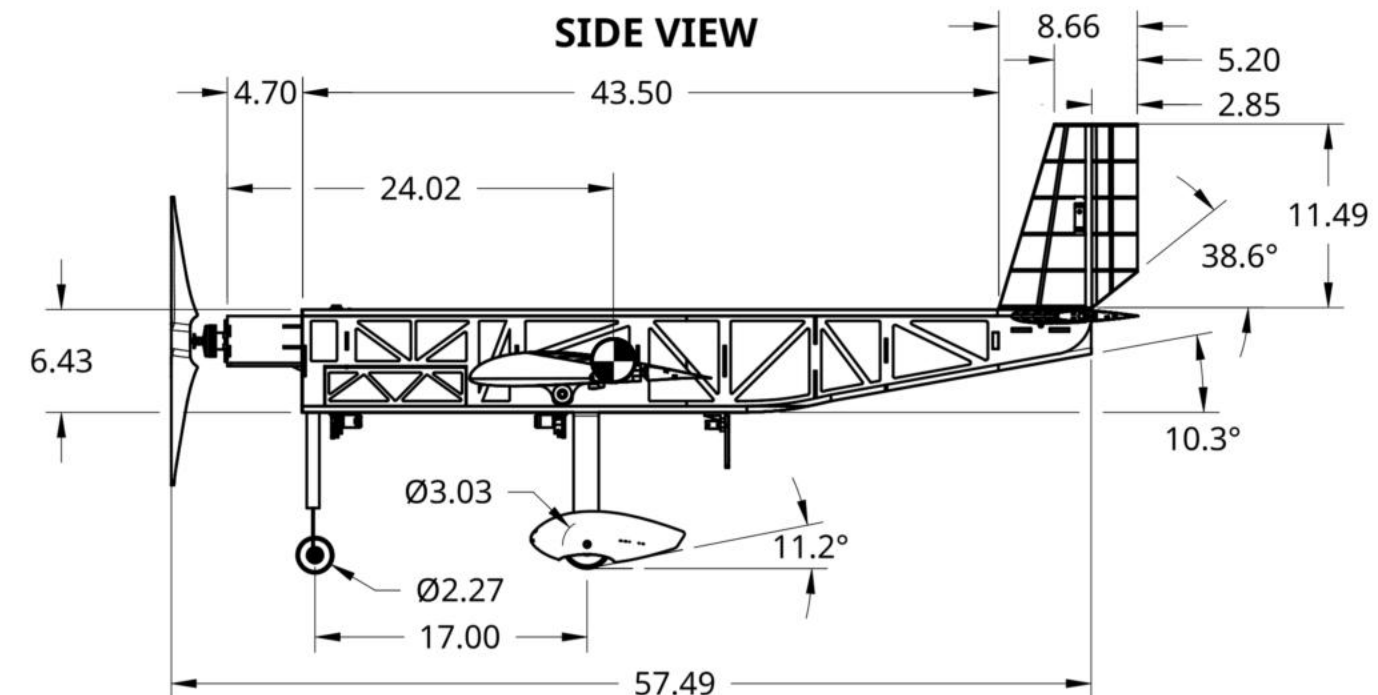
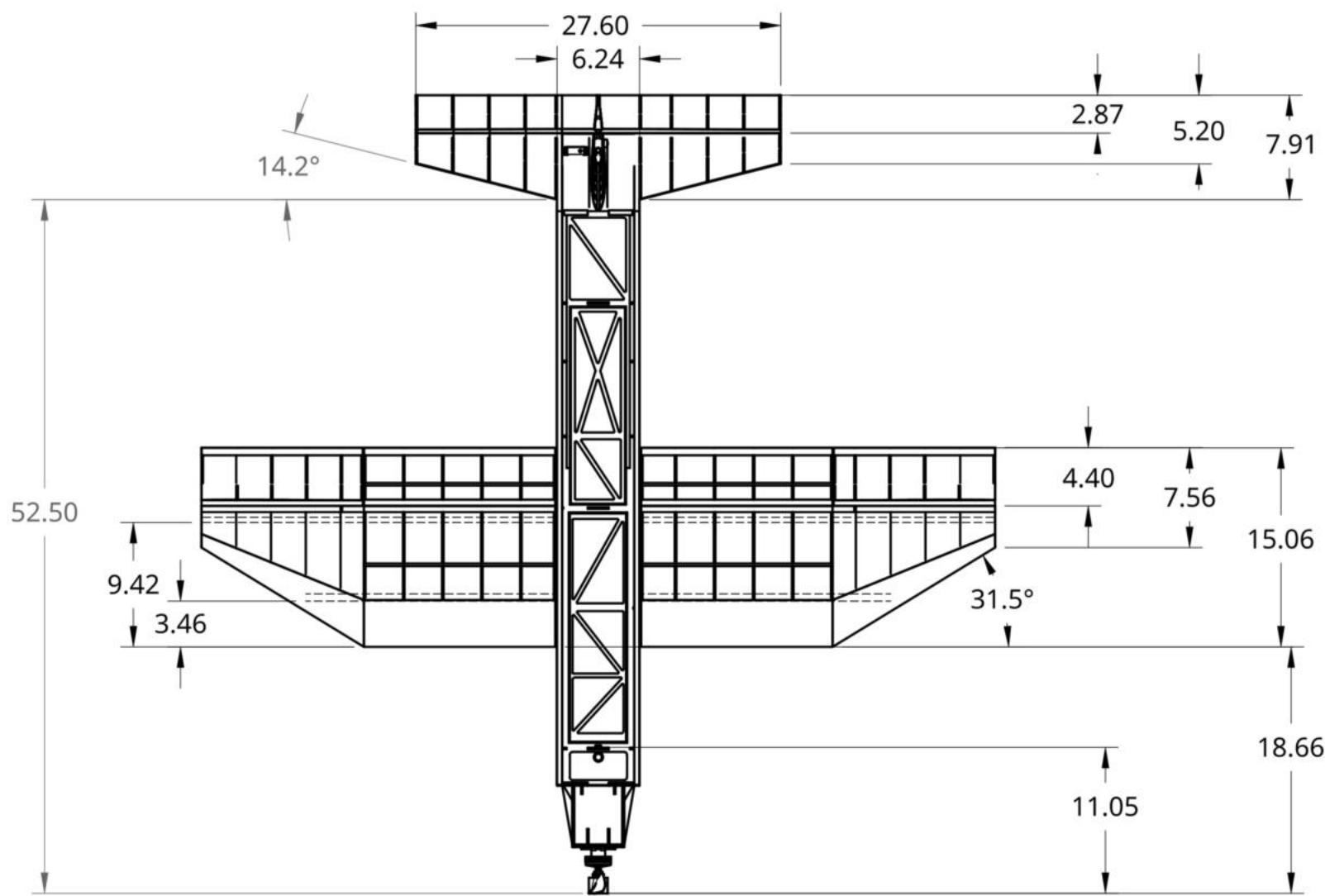


Figure 5.25: Mission Trajectory

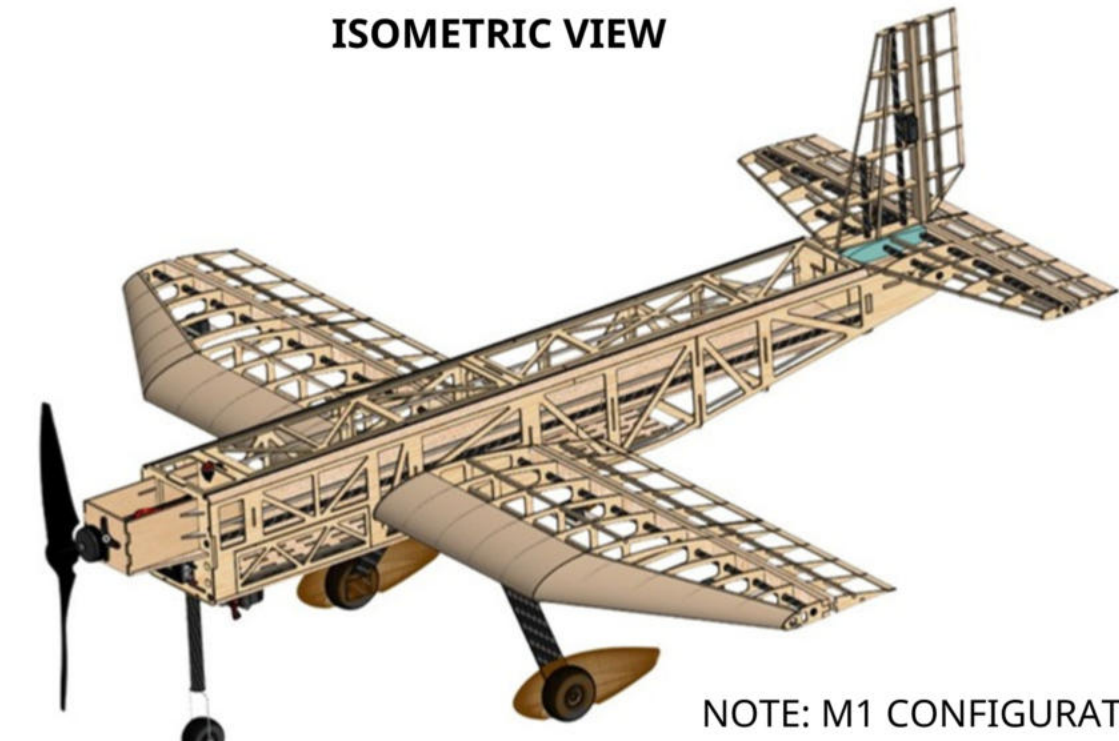
The trajectory is then divided into spatial segments consisting of straight, semi-circular and circular loops with speed commands schedules based on cumulative distance. To evaluate takeoff acceleration, maximum commanded velocity is applied during the initial 50 ft runway segment and the achieved velocity is compared against a safety threshold of  $1.2V_{stall}$ . During the straight segments, cruise speed is commanded while turn speed is commanded in curved segments to reflect increased load demand. This model enables consistent comparison between three missions, highlighting fundamental differences in acceleration capability, stall margin and overall trajectory feasibility.

### 5.6 Drawing Package

The following drawing package includes a dimensional 3-view, aircraft overview, structural layout, and mission layout. All drawings were made using Onshape.

**FRONT VIEW****SIDE VIEW****TOP VIEW**

COVERING FILM AND BALSA SKIN OMITTED FOR CLARITY

**ISOMETRIC VIEW**

NOTE: M1 CONFIGURATION

**Aerial Robotics Kharagpur**

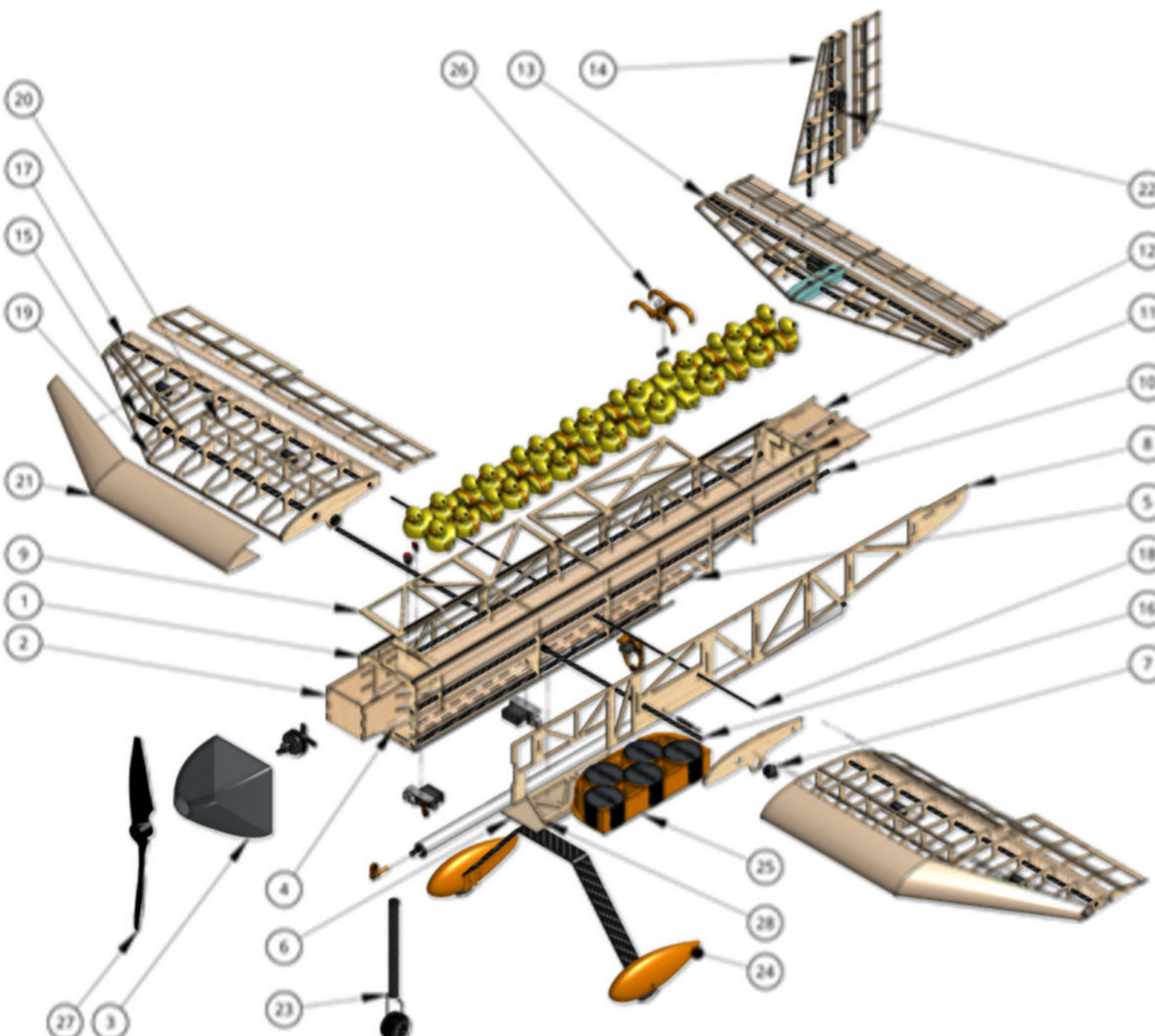
2026 Indian Institute of Technology Kharagpur "PUSHPAK"

UNLESS OTHERWISE  
SPECIFIED, ALL DIMENSIONS  
ARE IN INCHES

SIZE: <b>B</b>	DRAWING NO. <b>AIRCRAFT 3-VIEW</b>	REV. <b>1</b>
SCALE: 1:12	DRAWING PACKAGE	SHEET 1 OF 4

ITEM NO.	PART DESCRIPTION	MATERIAL	QTY
1	Fuselage Bulkheads	Birch Ply	8
2	Motor Mount	Aeroply	1
3	Nose Cone	Carbon Fibre	1
4	Duck Platform	Carbon Fibre, Balsa	1
5	Puck Platform	Carbon Fibre, Balsa	1
6	Landing Gear base plate	Aeroply	1
7	Wing Mount Pins	Aluminium	2
8	Fuselage Wing Side Panels	Birch Ply	2
9	Fuselage Top Hatch Panels	Birch Ply	2
10	Fuselage Longerons	Carbon Fibre	4
11	Fuselage Stringers	Carbon Fibre, Birch Ply	4
12	Tail Mount Base Plate	Aeroply	1
13	Horizontal Stabilizer	Balsa, Carbon Fibre, Birch Ply, XPS foam	1
14	Vertical Stabilizer	Balsa, Carbon Fibre, Birchply	1
15	Wing Main spar	Carbon Fibre	1
16	Wing Telescopic tube - Main	Carbon Fibre	2
17	Wing Auxilliary Spar	Carbon Fibre	1
18	Wing Telescopic tube - Auxilliary	Carbon Fibre	2
19	Wing Ribs	Birch Ply	22
20	Wing Stringers	Birchply, Balsa	20
21	Wing Leading Edge	Balsa	2
22	Servo mount Plate	Carbon Fibre + Balsa	9
23	Front Landing Gear	Aluminium, Carbon Fibre, Rubber	1
24	Wheel Pants	Fibreglass	2
25	Puck Restraint Mechanism	PLA	1
26	Duck Restraint Mechanism	PLA	1
27	Propeller	Carbon Fibre	1
28	Fuselage Side Hatch Panels	Birch Ply	1

COVERING FILM AND BALSA SKIN OMITTED FOR CLARITY



NOTE: M2 + M3 CONFIGURATION



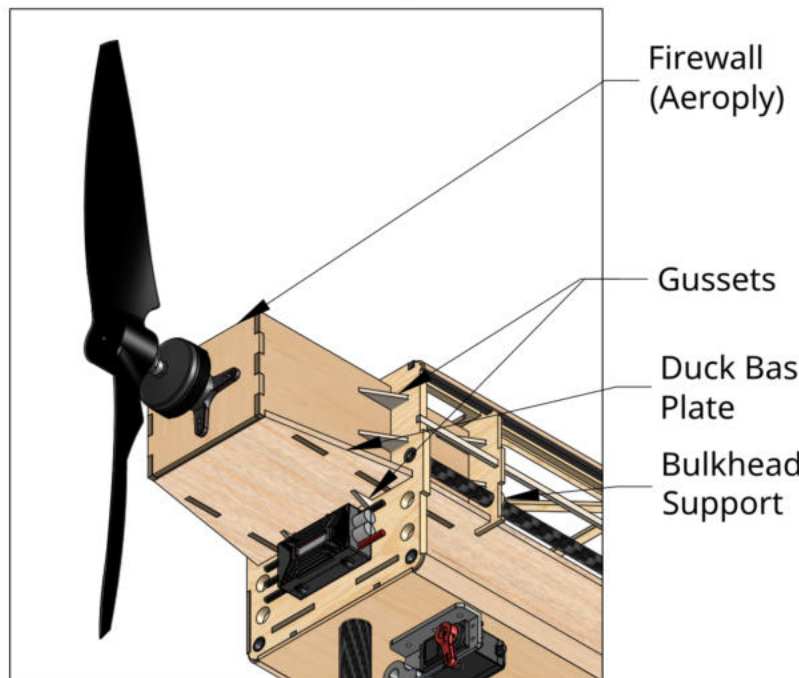
**Aerial Robotics Kharagpur**

2026 Indian Institute of Technology Kharagpur "PUSHPAK"

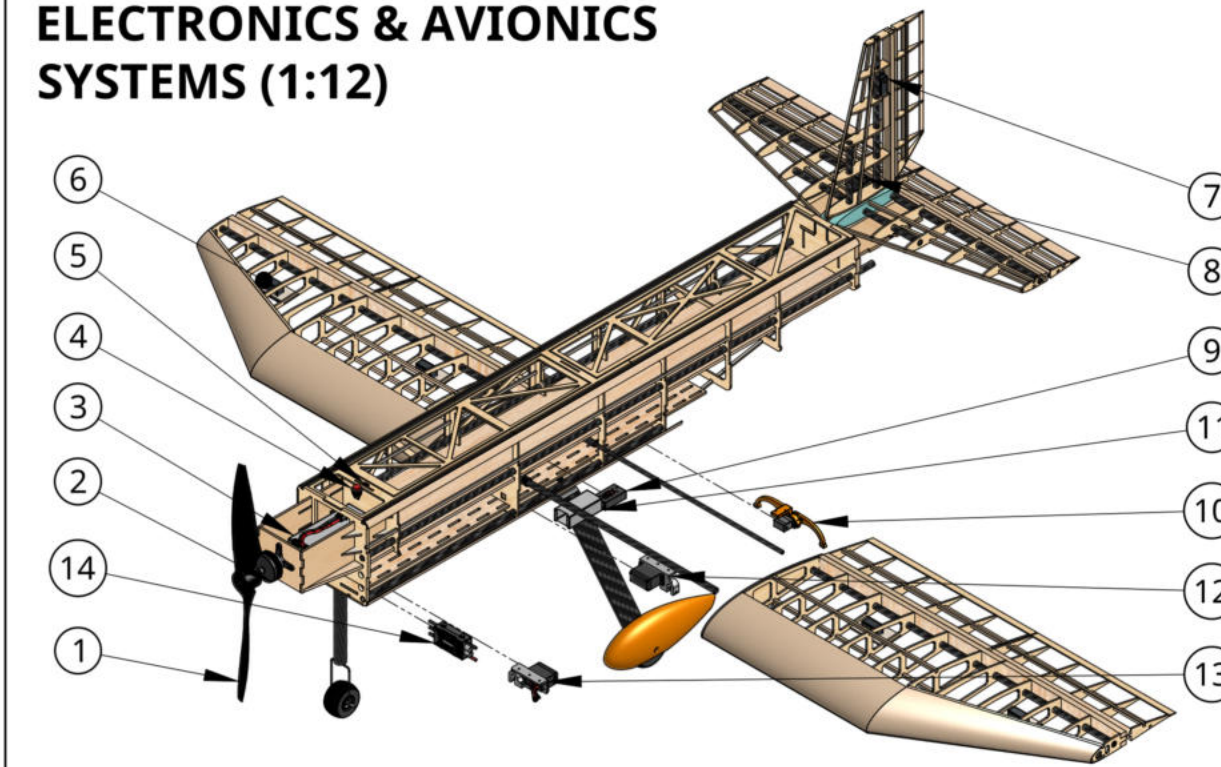
SIZE: <b>B</b>	DRAWING NO. <b>AIRCRAFT OVERVIEW</b>	REV. <b>1</b>
SCALE: 1:11	DRAWING PACKAGE	SHEET 2 OF 4

PASSENGER-CARGO AND BANNER ARE  
NOT FLOWN IN SAME MISSION

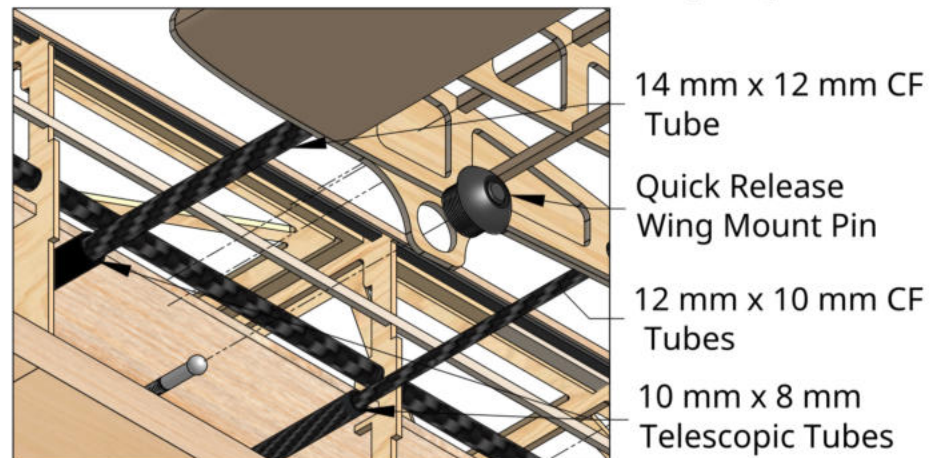
## MOTOR MOUNT (1:4.8)



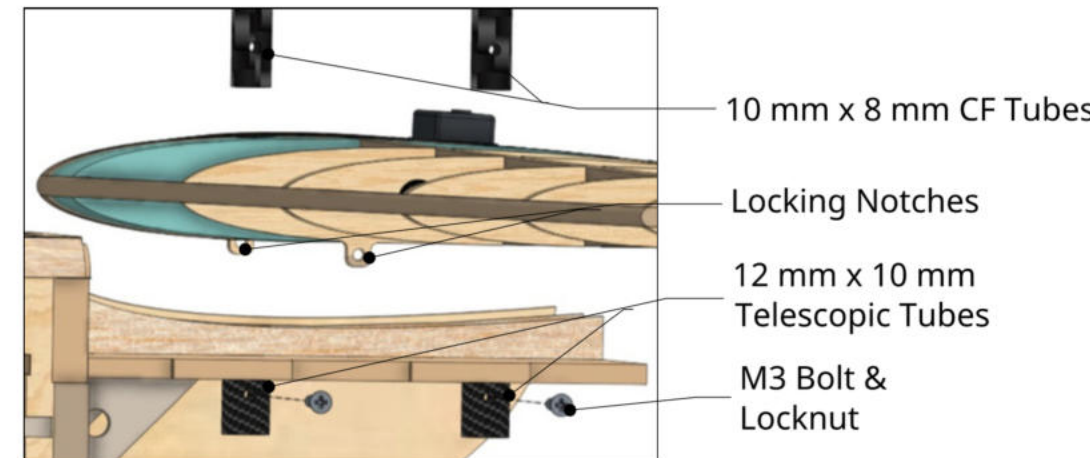
## ELECTRONICS & AVIONICS SYSTEMS (1:12)



## WING MOUNT MECHANISM (1:3)



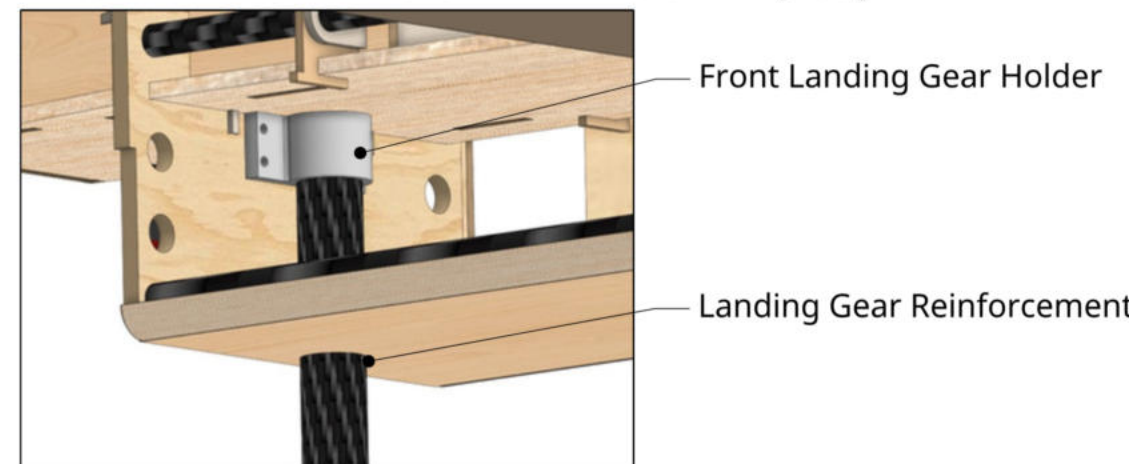
## TAIL MOUNT MECHANISM (1:3)



## MAIN LANDING GEAR MOUNT (1:3)



## FRONT LANDING GEAR MOUNT (1:3)



## ITEM NO.

ITEM NO.	DESCRIPTION	QTY
1	Propeller	1
2	Motor	1
3	Propulsion Battery	1
4	Kill Switch	1
5	Fuse 100 A	1
6	Wing Servo	4
7	Vertical Stabilizer Servo	1
8	Horizontal Stabilizer Servo	1
9	Receiver	1
10	Deployment Mechanism 2	1
11	Avionics Battery	1
12	Release Mechanism	1
13	Deployment Mechanism 1	1
14	ESC	1

## NOTE:

1. M1 CONFIGURATION
2. COVERING FILM AND BALSA SKIN OMITTED FOR CLARITY
3. UNLESS OTHERWISE SPECIFIED, DIMENSIONS ARE IN INCHES



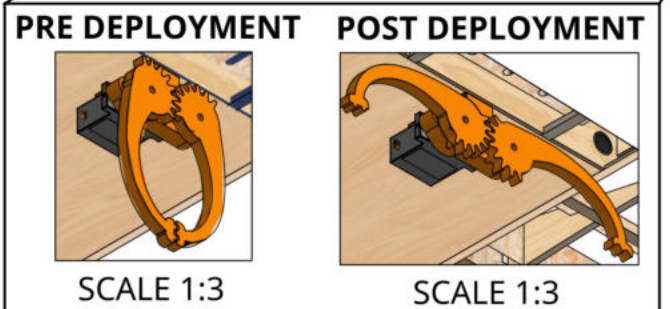
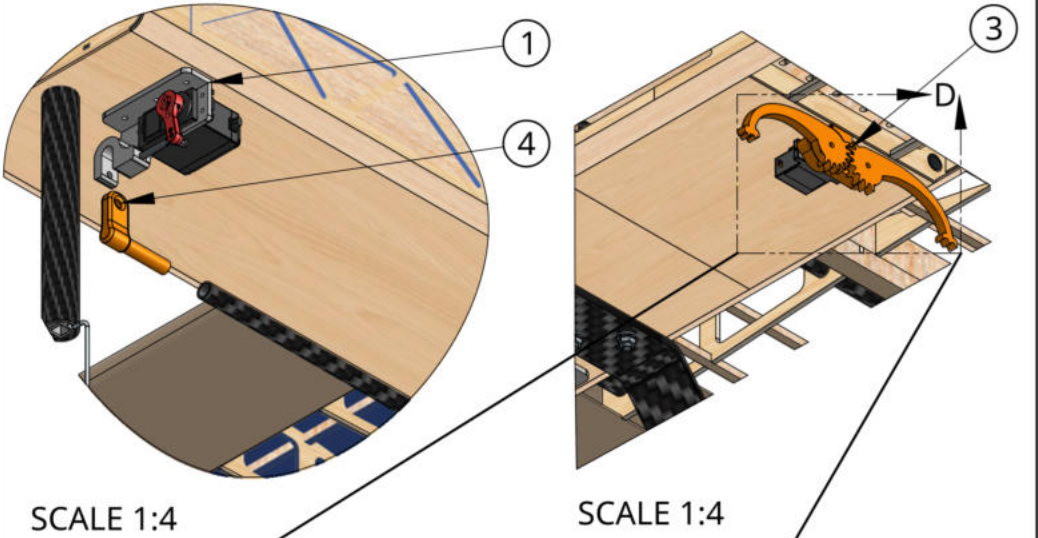
Aerial Robotics Kharagpur

2026 Indian Institute of Technology Kharagpur "PUSHPAK"

SIZE: B DRAWING NO. SYSTEM LAYOUT REV. 1

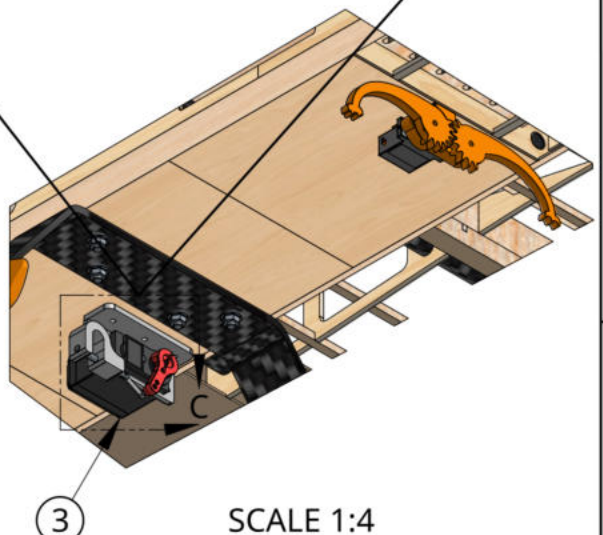
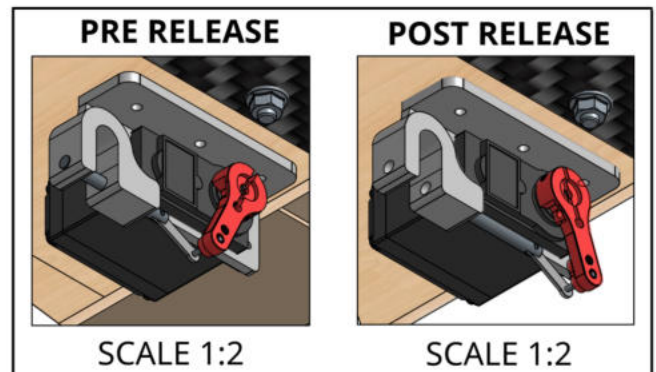
SCALE: AS NOTED DRAWING PACKAGE SHEET 3 OF 4

## BANNER DEPLOYMENT MECHANISM (M3)



ITEM NO.	DESCRIPTION	MATERIAL
1	Linear Actuator-1	Aluminium
2	Linear Actuator-2	Aluminium
3	Banner Claw Mechanism	PLA
4	Banner Rod Attachment	PLA

## BANNER RELEASE MECHANISM (M3)



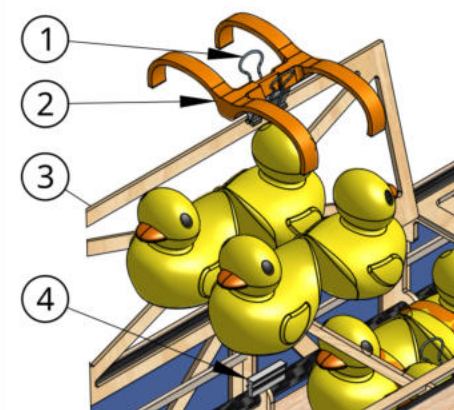
## BANNER LAYOUT (M3)



COVERING FILM AND BALSA SKIN OMITTED FOR CLARITY

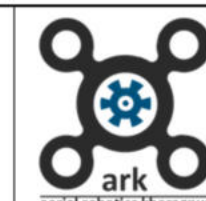
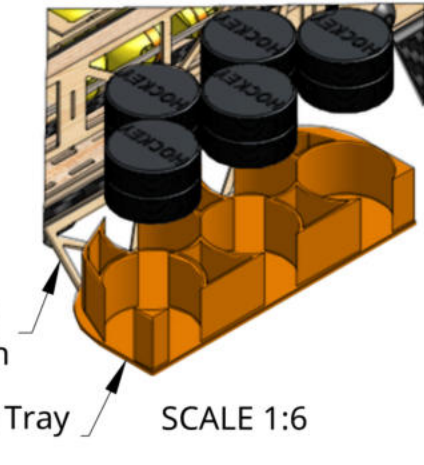
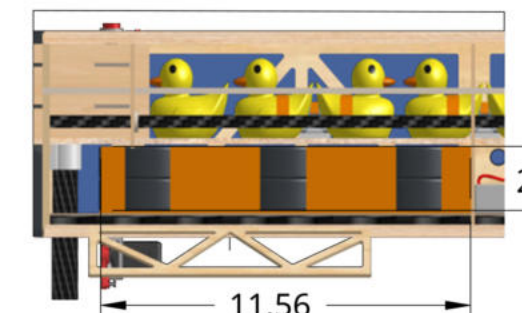
UNLESS OTHERWISE  
SPECIFIED, ALL DIMENSIONS  
ARE IN INCHES

## PASSENGER RESTRAINT MECHANISM (M2)



ITEM NO.	DESCRIPTION	MATERIAL
1	Clip for securing ducks	Plastic
2	Duck Restraint Clamp	PLA
3	Duck Hatch	Birch Ply
4	Duck Restraint Rail	PLA

## PUCK RESTRAINT MECHANISM (M2)



Aerial Robotics Kharagpur

2026 Indian Institute of Technology Kharagpur "PUSHPAK"

SIZE:	DRAWING NO.	REV.
B	MISSION LAYOUT	1
SCALE: AS NOTED	DRAWING PACKAGE	SHEET 4 OF 4

## 6. Manufacturing Plan

### 6.1 Available Manufacturing Processes

#### 6.1.1 Laser Cutting

Laser cutting was used to manufacture the ribs from aircraft-grade plywood because it allows thin sheets to be cut accurately while preserving detailed geometries. The method is well-suited to producing repeatable parts with tight tolerances. Cutting paths were arranged using vector ordering to reduce production time and improve workflow efficiency.



**Figure 6.1:** Laser Cutter

Additive manufacturing was employed for components that required complex internal features and tight geometric control. Polymer materials such as PLA provided sufficient design flexibility for these applications. Parts, including the duck and puck decks, the banner deployment and release system, and molds for composite fabrication, were produced using 3D printing to accommodate their intricate shapes. The banner release mechanism was also evaluated through prototype testing, where it demonstrated consistent and reliable operation.

A practical limitation during production was access to a dependable, high-quality 3D printer, as machine availability was shared across multiple departments within the institute. Fabrication was ultimately carried out using a Bambu Lab P1S printer, which met the required print quality and repeatability for the final parts.

#### 6.1.3 Composite Manufacturing

Composite materials are widely used in aerospace structures because they provide high strength at low weight and can sustain loads with some flexibility before failure. Producing reliable composite parts, however, requires a controlled workflow that includes proper mold preparation, wet layup, and vacuum bagging, with curing carried out under controlled conditions to reach the desired properties. These steps demand time, care, and material resources, and typical lead times can extend to several weeks, which limits how quickly design changes can be implemented.

In our case, composite fabrication also presented a learning challenge. The team did not begin the project with prior hands-on experience in this area, so the required processes were learned and practised during the build phase. Considerable effort went into developing workable procedures and avoiding common layup defects so that the final parts were suitable for flight use.

#### 6.1.4 Heated Monocote Cover Film

The finished airframe was covered with Monocote, a heat-shrink film commonly used on wooden model aircraft. The covering seals the open balsa structure and forms a smooth outer surface, which helps keep the airflow clean over the wing and fuselage. When properly tensioned, the film also adds noticeable torsional rigidity to the wings by tying the structure together.

Applying the film requires careful temperature control. Since it tightens as heat is applied, the shrinking must be done gradually and uniformly to avoid twisting or distorting the lightweight framework. Because the material is thin, the surface was inspected regularly during handling and operation to reduce the chance of punctures and to preserve the finish.



**Figure 6.2:** Monokote Cover Film

### 6.1.5 Wooden and Foam Construction

The core fuselage was constructed mainly from balsa, birch plywood, and bass plywood. These wood types were selected for their desirable characteristics of strength, cost efficiency, and weightlessness. Balsa was utilised for its low density and speed of replacement, while bass plywood gives much-needed reinforcement in high-stress regions. The skin was constructed using 0.06 in balsa by dampening and bending it to the desired shape. Laser cutting was used for the fabrication of birch and bass plywood wood to ensure high dimensional accuracy and speed of production. Extruded Polystyrene Foam (XPS) was used in very few places, like the central portion of the horizontal stabiliser, where there are carbon fiber rods that form a crucial part of the tail mounting mechanism.

### 6.2 Composite Material Selection

A material and layup trade study was carried out to select suitable configurations for ribs and local reinforcements. Laminates were compared using qualitative rankings for strength, weight, stiffness, and cost so that structural capability could be balanced against mass limits. Since each component carries load differently, the objective was to arrive at practical layups for each application rather than adopt a single solution across the aircraft.

For reinforcements, sandwich constructions with fiberglass skins and lightweight cores were examined. Layups aligned at 0° to the wood grain provided good strength along the grain direction but offered limited resistance across it, whereas ±45° orientations distributed loads more evenly and improved transverse and shear performance. This trend is reflected in Table (insert table number). Although XPS and Depron cores reduced weight, they were rated lower where bond reliability and localised compressive strength were important, which influenced the final selections.

Table 6.1: Composite Selection Process

Reinforcements	Layup Configuration			Parameters				Total
	No. of layers (per side)	Orientation of layers (degrees)	Core material	Strength (0.35)	Weight (0.2)	Stiffness (0.35)	Price (0.1)	
Reinforcements	2	0	Balsa (3 mm)	4	2	4	2	3.4
	1	0	Depron	1	5	1	5	2.2
	2	0	XPS	2	4	2	4	2.6
	1	0	Balsa (3 mm)	3	3	3	3	3
	2	45	Balsa (3 mm)	5	2	5	2	4.1
	2	0,45	Balsa (3 mm)	5	2	5	2	4.1
	1	45	Balsa (3 mm)	3	3	3	3	3

For the separation plate and other high-load reinforcements, double fiberglass layers on both sides at 45° orientation were selected. Although this configuration adds weight, strength and damage tolerance were prioritised in these regions to ensure structural reliability.

For wing skins, a balsa sheet was retained as the primary skin material due to its low mass and adequate baseline stiffness. Where additional strength is required, the skin can be reinforced with a single fiberglass layer applied directly onto the balsa using a wet layup process. This configuration serves as a practical strengthening option by improving load transfer and overall structural integrity without a significant weight penalty.

In order to reduce prototyping costs, it was decided to first manufacture all composite parts such as the nacelle and the passenger platform with glass fiber instead of carbon fiber for the first iteration. The final iteration will use carbon fiber.

## 6.3 Selected Manufacturing Processes

### 6.3.1 Fuselage

The fuselage comprises bulkheads laser-cut from 0.12 in birch plywood, which are interconnected by a lightweight truss structure made of birch plywood to achieve weight reduction while preserving longitudinal and torsional stiffness. The bulkheads transfer structural loads to the longerons and the plate (the primary load-bearing structures), which are constructed from carbon fiber and aero plywood. All structural components are bonded using an epoxy-based adhesive to ensure load transfer continuity and structural integrity.



**Figure 6.3:** Fuselage construction of Pushpak V1

This internal framework is subsequently covered with a 0.06 in balsa wood skin, which is bonded using cyanoacrylate (CA) glue to provide a smooth external finish. A composite sandwich consisting of 2 layers of fiberglass oriented at 45 degrees to the balsa grain is used for the base plate of the fuselage and the motor mount due to its high strength-to-weight ratio (refer to Section 6.2).

### 6.3.2 Aerodynamic and control surfaces

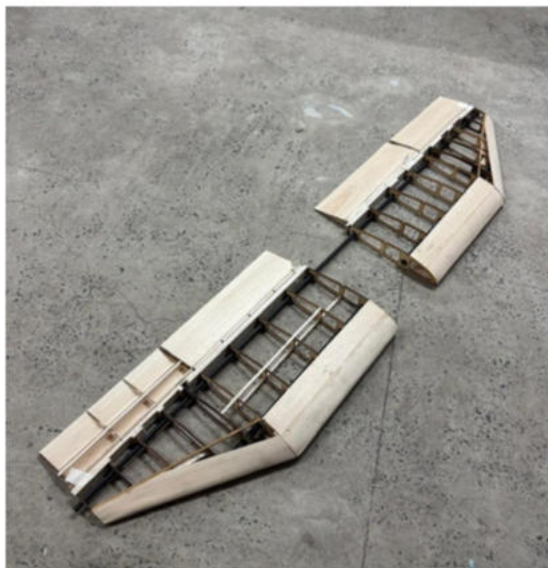


**Figure 6.4:** Wing construction of Pushpak V1

The wing, horizontal stabiliser, and vertical stabiliser structures are composed of ribs made from a balsa-fiberglass reinforced composite, interconnected by two primary carbon fiber spars and several pine wood stringers. All control surfaces follow a similar structural approach, with pine wood stringers forming their main load-carrying members. Regions accommodating the hinges are locally reinforced using 4 layers of 0.12 in balsa wood to withstand concentrated loads. The servo mounts are made using the composite sandwich (refer to Section 6.2). All structural components are bonded using a combination of epoxy-based adhesive and CA glue. The resulting internal framework is then covered with 0.06 in balsa wood and covered by a heated Monocote film. To improve the strength, the wing can be further reinforced with a single layer of fiberglass added by the wet layup method on the balsa skin directly to ensure effective load transfer and overall structural integrity.



**Figure 6.5:** Landing gear (COTS)

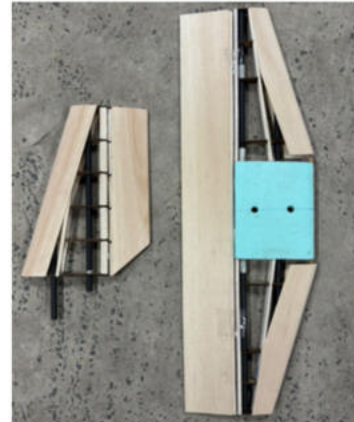


**Figure 6.6:** Tail construction of Pushpak V1

### 6.3.3 Landing gear

The landing gear, wheels and wheel fairings is procured externally as COTS parts due to the team's limited experience with composites. In order to withstand impulsive loads, it is integrated with the fuselage using the glass fiber composite plate (refer to section 6.2)

### 6.3.4 Nacelle

The mold for the nacelle was 3D printed and sanded to remove any surface irregularities (refer to Section 6.1.2). Once the desired surface finish was achieved, a wet layup process was carried out using 3 layers of plain weave fiberglass of 80 gsm areal density. To improve the strength, a similar layup can be performed using carbon fiber.

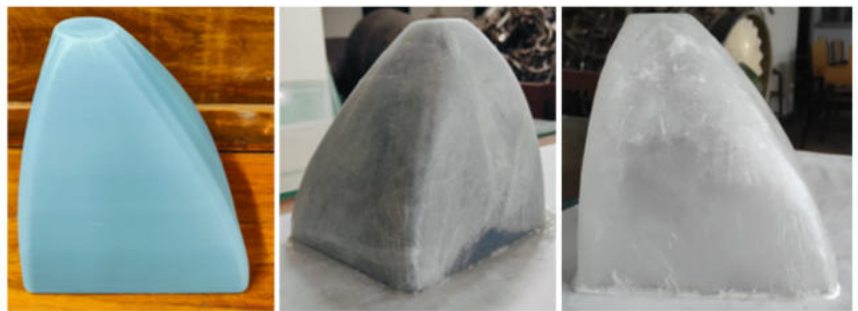


Figure 6.7: Fiberglass wet layup process carried out for the nose of Pushpak V1

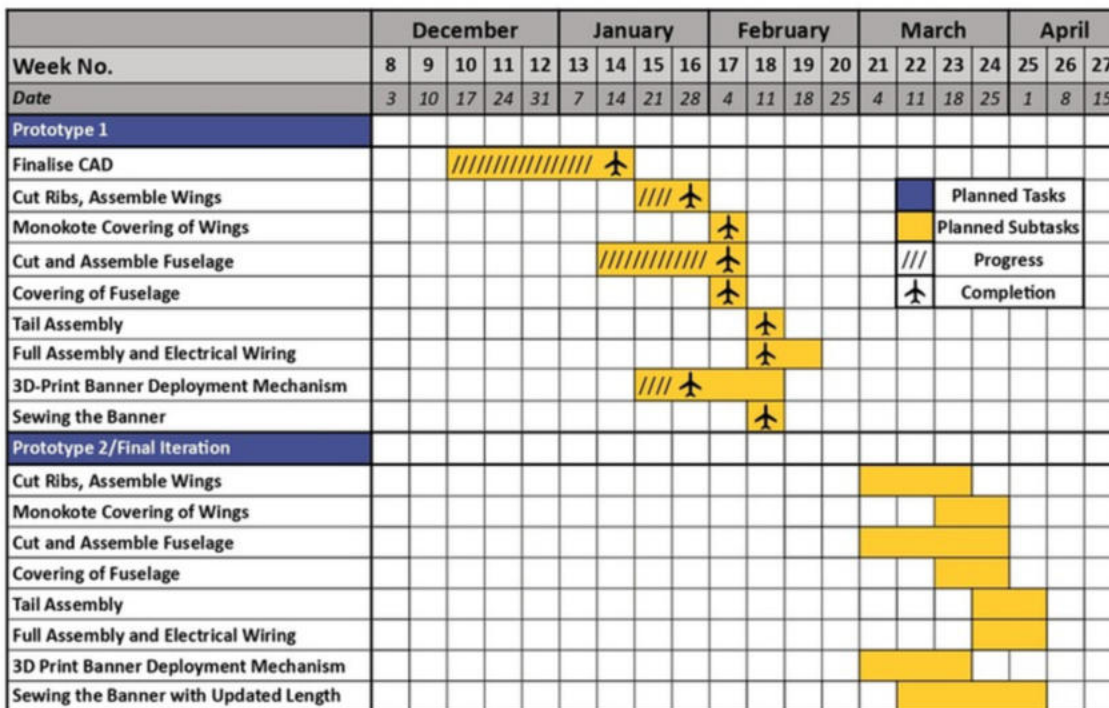
Table 6.2: Manufacturing Processes Selected for Various Parts

Component	Material	Technique
Fuselage	Birch Plywood	Laser Cutting
Wing		
Horizontal Stabilizer	Carbon Fiber, Birch Plywood, Pine Wood	Laser Cutting, Balsa Moulding
Vertical Stabilizer		
Skin	Balsa, Monokote Film	Balsa moulding, Hot Iron
Spars		
Landing gear	Carbon fiber	COTS
Separation plate	Fiberglass, Balsa	
Nose	Fiberglass	Composite manufacturing
Banner mechanism	PLA, Aluminium	3D Printing

### 6.4 Manufacturing Timeline

The manufacturing process began with a focus on CAD and the theoretical design. By the second week of January, manufacturing of Pushpak V1 was started, while simultaneously testing the propulsion system. Pushpak V1 was completed by the 2nd week of February, which gave us a few valuable days to test it as a proof of concept. Further planned schedules are as depicted in the Gantt chart.

Table 6.3: Manufacturing Schedule



## 7. Testing Plan

Table 7.1 presents the structured testing timeline from December to April. Propulsion testing began in December, followed by ground mission testing in mid-January and structural testing in the last week of January. Banner drag and deployment/release mechanism testing were conducted through late January and early February, leading into flight testing in early February, with the banner mechanism validated on a pre-made RC aircraft. Testing with Pushpak V1 (prototype 1) is currently ongoing, and the final iteration testing phase is planned for March and early April.

Table 7.1: Testing Schedule

	December					January					February					March				April		
Week No.	8	9	10	11	12	13	14	15	16	17	18	19	20	21	22	23	24	25	26	27		
Date	3	10	17	24	31	7	14	21	28	4	11	18	25	4	11	18	25	1	8	15		
Subsystem Testing																						
Propulsion System																						
Structural Testing																						
Ground Mission																						
Banner Drag																						
Banner Deploy/Release mechanism																						
Flight Testing																						
Banner Mechanism, Pre-made RC Plane																						
Prototype 1: No Payload /Banner	■																					
Prototype 1: With Payload and Banner	■																					
Final Iteration: No Payload /Banner	///																					
Final Iteration: With Payload and Banner	■	■																				
						Planned Tasks																
						Planned Subtasks																
						Progress																
						Completion																

### 7.1 Banner Drag - Wind Tunnel Testing

Aerodynamic testing was conducted to measure and understand the drag characteristics of banners. The primary test variables included banner length (l<sub>b</sub>) and freestream velocity (V). The resulting data was used to compute the drag coefficient ( $C_d$ ) and analyze its variation with Re, as shown in Figure 8.1. The experiments were conducted in an industrial wind tunnel. A pre-calibrated load cell, was mounted on a stool to measure axial drag force.

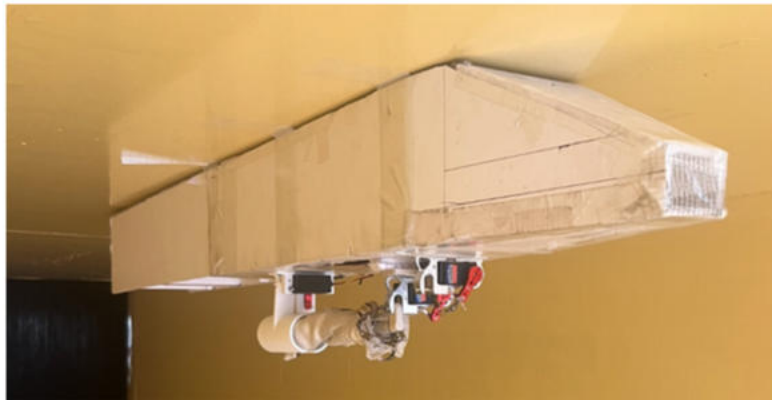
The banner was tethered directly to the load cell and aligned with the flow direction. Readings were recorded using a camera mounted on the roof of the wind tunnel for post-processing and analysis. The objective of this study was relative drag characterization rather than absolute high-fidelity drag measurement.



Figure 7.1: Wind tunnel testing of banner setup with drag force measurement using load cell

## 7.2 Banner Deployment and Release Mechanism Feasibility

To assess the feasibility of banner deployment mid-flight, a prototype release mechanism was fabricated and tested in the wind tunnel. The setup consisted of a depron fuselage with the deployment and release system, capable of deploying a rolled-up banner. Multiple combinations of claw and leading-edge holding mechanisms were evaluated to identify the most reliable configuration. This setup was used to explore the effects of towing line length and optimal banner folding for smooth deployment. This test confirmed both the mechanical reliability of the release mechanism of banner deployment from a moving vehicle.



**Figure 7.2:** Prototype banner deployment mechanism mounted for wind tunnel testing

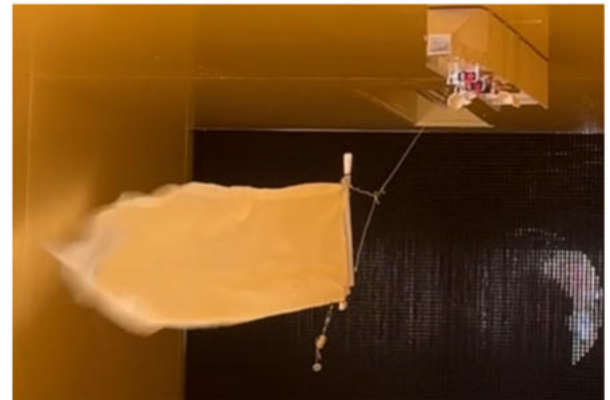


**Figure 7.3:** Deployment phase of banner release in wind tunnel, demonstrating extension and stabilization during freestream exposure

To validate the Banner Release Mechanism, the MG995 linear actuator was tested under a static load by attaching a 2.0 kg weight to the towing wire. The mechanism successfully executed the release without stalling or structural deformation, confirming the system's ability to maintain precise control over the actuation under mission-representative tension. This result provides confidence that the assembly can reliably deploy the banner despite the impulsive loads encountered during pickup and flight.

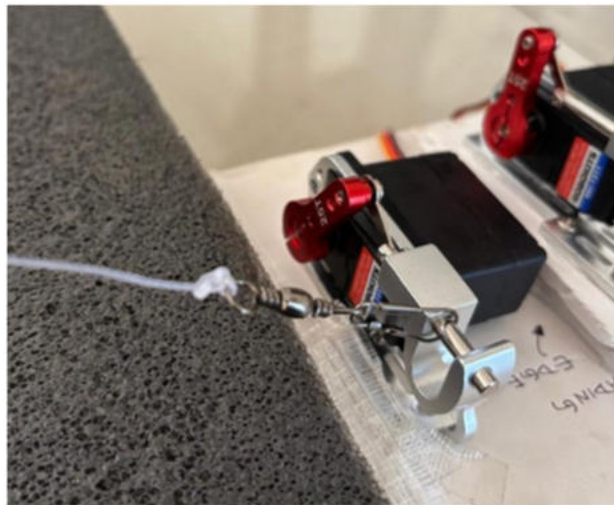


**Figure 7.4:** Linear Actuator Load Test

### 7.3 Propulsion System Testing

A static thrust test stand was built which utilizes a rig that includes an aluminum cantilever rigidly fixed to a stationery workbench. A load cell was attached at the free end of the cantilever to measure thrust as shown in Figure 7.4. An Arduino Uno was used to monitor the load cell and interface with a laptop. Additional circuitry using an op-amp was utilized to track the throttle level of the motor under operation.



Figure 7.4: Static Thrust Stand Rig

A high precision watt-meter recorded the current, voltage and power drawn while a digital laser tachometer recorded the RPM of the motor. The rig was used to perform static thrust tests and the data obtained was used to make design choices for identifying the ideal propulsion package.



Figure 7.5: Tested Propellers

Six different propellers were chosen for static thrust testing. These tests were performed with a newly bought 4500 mAh 6S Lithium ion battery initially at 100%. The tests were conducted for throttle of 100%, and endurance is the time taken to drain the battery from 100% to 50% capacity at 100% throttle. The best propeller in terms of maximum endurance, reasonable battery heating, and optimum thrust requirement was hence chosen. Along with this, two popular battery types, Lithium Polymer (LiPo) and Lithium Ion (Li+) were selected for finding which one has a better performance under the given constraints. For 6S batteries of the same capacity for both materials were tested for maximum thrust, endurance, battery heating, power and various throttle.

### 7.4 Wing and Fuselage Structural Testing

The wing load test was conducted to validate the structural integrity of the aircraft under a loading condition equivalent to the maximum mission weight, representing the most critical bending case expected in flight. The wing was supported at the start of the taper section to focus the stress on the primary central load-bearing spar and the wing-fuselage junction. In the first stage, a 4.41 lb ballast was applied as a safety precaution to verify the initial elastic response and ensure the integrity of the fiberglass-reinforced joints. Following the successful initial validation, the load was increased to a final ballast of 14 lb, distributed across the center of the wing to engage both the primary carbon fiber and secondary balsa spars equally.



Figure 7.6: Wing Load Test 4.41 lb



Figure 7.7: Wing Load Test 14 lb

No signs of local buckling or material distress were observed, satisfying the structural requirements. During testing, the wing-fuselage interface was identified as the most critical structural region due to stress concentration at the joint. To mitigate this, the joint was reinforced using fiberglass layups, improving load transfer and overall stiffness at the root. Subsequent evaluation confirmed a substantial increase in joint rigidity, providing high confidence against structural failure under mission loading conditions.



**Figure 7.8: Pushpak V1 Assembly**

## 7.5 Checklist

Table 7.2 shows the checklist that is to be followed by the team for the safety and security of the crew during preflight, in-flight and post-flight operations.

**Table 7.2: Flight Checklist**

Flight Briefing			
Date, Time & Location		Payload Configuration	
Pilot		Total Weight	
Flight Objective			
Ground Inspection			Taxi and Before Takeoff
Fuselage		Brief	<input type="checkbox"/>
Wing Mount	<input type="checkbox"/>	Kill Switch	<input type="checkbox"/>
Tail Mount	<input type="checkbox"/>	Fuse	<input type="checkbox"/>
Landing Gear	<input type="checkbox"/>	Control Surface Actuation	<input type="checkbox"/>
Hatches Secured	<input type="checkbox"/>	Control Surface Rates	<input type="checkbox"/>
Avionics		Thrust Test	<input type="checkbox"/>
All Vehicle Wiring Secured	<input type="checkbox"/>	Wind and Weather Check	<input type="checkbox"/>
Control Surfaces	<input type="checkbox"/>	Taxi	<input type="checkbox"/>
Control Horns and Push Rods	<input type="checkbox"/>	Runway Clearance	<input type="checkbox"/>
Propulsion		Pilot Ready To Rock	<input checked="" type="checkbox"/>
Propeller Condition	<input type="checkbox"/>	M2	
Propeller Direction	<input type="checkbox"/>	Ducks Restraint	<input type="checkbox"/>
Propeller Mount	<input type="checkbox"/>	Pucks Restraint	<input type="checkbox"/>
Motor Mount and Firewall	<input type="checkbox"/>	M3	
Pre-Flight Inspection		Banner Rolling & Securing	<input type="checkbox"/>
Kill Switch	<input type="checkbox"/>	Banner Deployment	<input type="checkbox"/>
Fuse	<input type="checkbox"/>	Banner Release	<input type="checkbox"/>
Weight	<input type="checkbox"/>	Post-Flight Inspection	
CG location	<input type="checkbox"/>	Kill Switch, Fuse & Battery Disarm	<input type="checkbox"/>
Avionics Battery Connection	<input type="checkbox"/>	Aircraft & Payload Condition	<input type="checkbox"/>
Telemetry and Range Check	<input type="checkbox"/>	ESC and Motor Temperature	<input type="checkbox"/>
Propulsion Battery Connection	<input type="checkbox"/>	Debrief	<input type="checkbox"/>

## 8. Performance Results

### 8.1 Aerodynamics of Banner

The measured drag data was used to compute the banner drag coefficient  $C_d$  across a range of  $Re$  relevant to in-flight conditions. The variation of  $C_d$  with  $Re$  is shown in Figure 8.1.

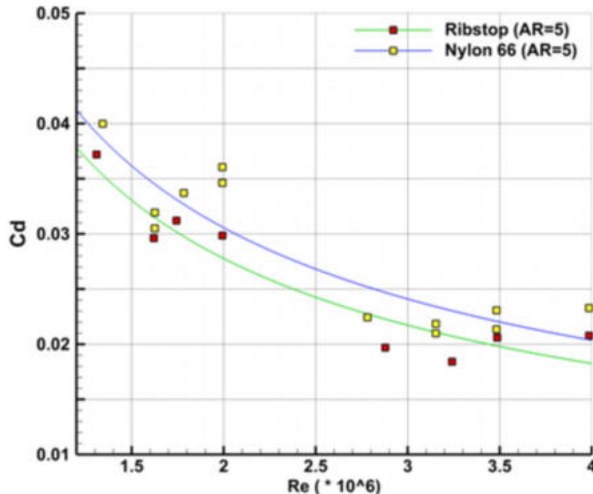


Figure 8.1: Variation of  $C_d$  with  $Re$  for Ripstop, Nylon 66

As seen in the  $C_d$ - $Re$  plot, both materials exhibit a similar decreasing trend in drag coefficient with increasing Reynolds number. Ripstop nylon shows consistently better aerodynamic performance than Nylon 66. Despite this reduction, the measured  $C_d$  values for the two materials remain within the same order of magnitude, converging near the operational Reynolds number range, which matches literature [16]. Therefore, selecting a banner solely based on marginal differences in  $C_d$  does not directly result in an additional lap within the fixed mission window. Consequently, material selection was driven primarily by structural strength and fluttering behaviour. Experimental observations showed that ripstop nylon was superior to Nylon 66 in these respects, leading to improved text readability; hence, it was selected as the final banner material.

$C_d$  error percentage exhibits a noticeable decay as Reynolds number increases, stabilising around  $Re \approx 3 \times 10^6$ . This behaviour aligns with known fluid-structure interaction dynamics: at lower Reynolds numbers ( $Re < 3 \times 10^6$ ), banner oscillations were observed to have larger amplitudes and lower frequencies, resulting in greater flow separation and energy dissipation, hence higher drag. As Reynolds number increases ( $Re > 3 \times 10^6$ ), oscillation frequency increases while amplitude reduces, leading to lower unsteady wake losses and reduced time-averaged drag. The observed decrease in  $C_d$  error percentage therefore confirms the reduction in fluttering intensity and indicates increasingly stable aerodynamic behaviour within the operational regime.

### 8.2 Banner deployment and feasibility tests

Wind tunnel trials revealed that improper wire sizing and coiling caused deployment failure. Replacing the original longitudinal support with a micro-servo claw and refined folding technique provided a lighter, more reliable solution. While increasing leading-edge weight improved stability and reduced spin, it required careful balancing against increased drag and structural strain. Ultimately, these tests were crucial to finalizing the mechanism and ensuring flight safety. These refinements successfully mitigated previous deployment risks, allowing for high-confidence flight operations in the final mission configuration.

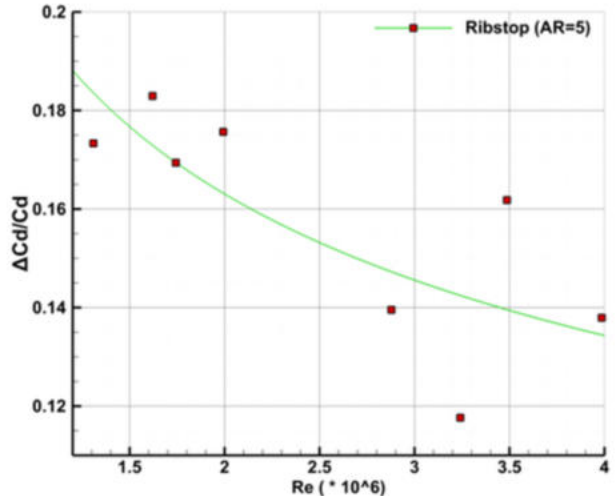


Figure 8.2: Relative variation in drag coefficient ( $\Delta C_d / C_d$ ) with Reynolds number for Ripstop Nylon, indicating reduced oscillatory drag at higher  $Re$

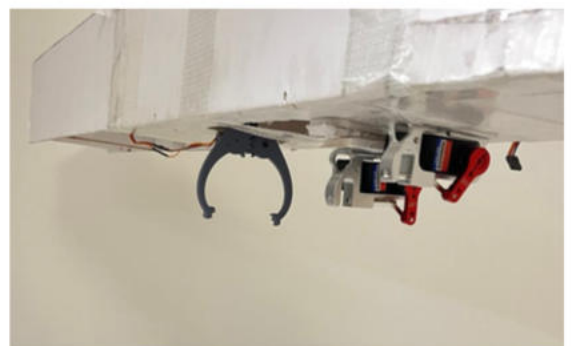


Figure 8.3: Final claw-based release mechanism integrated onto the prototype fuselage

### 8.3 Propulsion System

To ensure the credibility of calculated performance parameters from MotoCalc [7], the MotoCalc [7] data was compared with static thrust test data for Li+ battery and 18x8 carbon fibre propeller. Static thrust of the system is plotted against the current drawn for both the experimental data and the MotoCalc [7] data. The MotoCalc [7] data seems to overpredict the static thrust generated for the same current drawn. This also occurs due to heating losses, but the maximum relative error found was less than 10%. Thus, it can be concluded that MotoCalc [7] calculations are credible.

The battery testing aimed at understanding the difference in the performance of a LiPo and a Li+ battery. The power drawn for different throttle settings by each battery has been plotted in Figure 8.5. This test was conducted with the same T-Motor AM670 520KV and 18x8 Carbon Fibre Propeller. Specific performance parameters are tabulated in Table 8.1. From the analysis of the performance parameters, it is preferable to use the LiPo battery for all the missions due to their relatively higher current provided, thrust, and less heating compared to Li+ battery.

The propellers were compared over various parameters tabulated in Table 8.1. The static thrust generated by each propeller is plotted against the current drawn. For the graph, the battery chosen was Li+ battery and the motor was T-Motor AM670 520KV. For propellers of dimensions 18x8 but different materials, it can be observed that the thrust produced by the APC propeller is relatively high but it has a very poor efficiency based on the power drawn by it from the battery and the endurance of the system with APC propellers. Wooden propellers produce lower thrust but have slightly higher efficiency than the APC propellers.

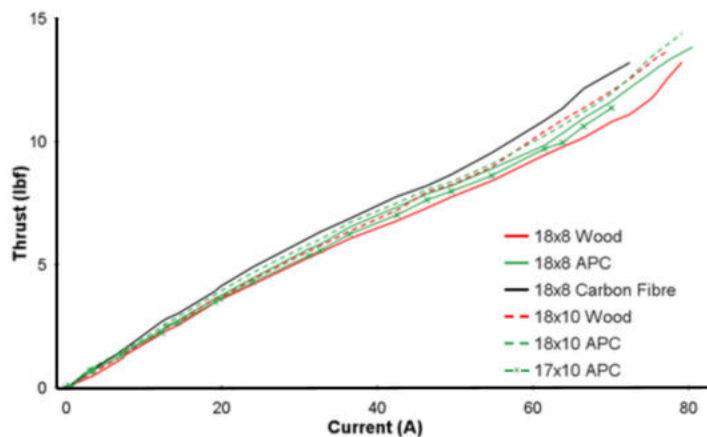


Figure 8.6: Thrust v/s Current

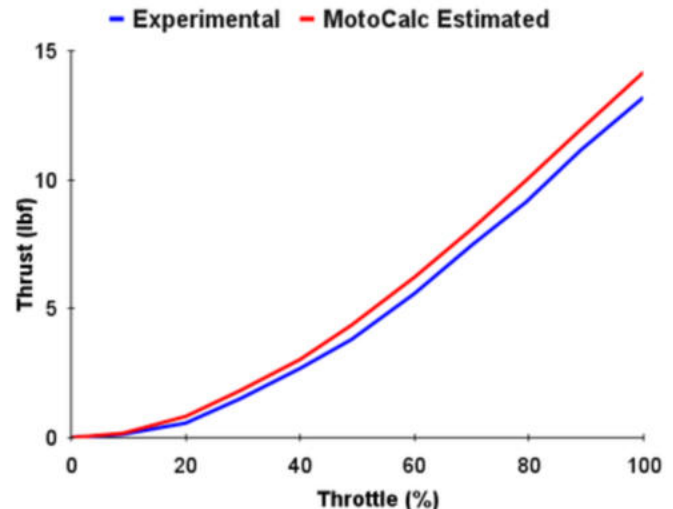


Figure 8.4: Thrust v/s Throttle for 18x8 CF

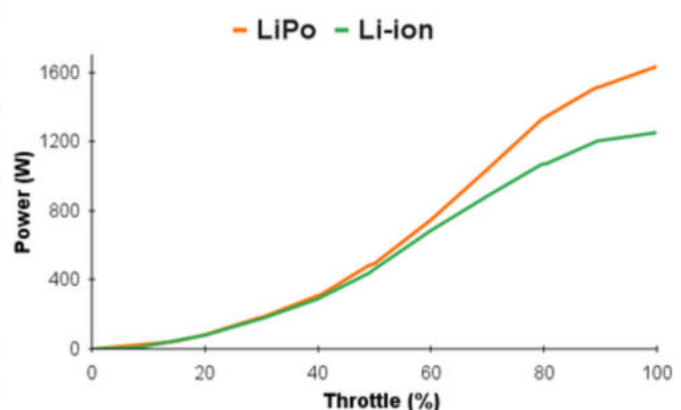


Figure 8.5: Power v/s Throttle for different batteries

Table 8.1: Battery Performance Table

Parameter	LiPo	Li+
Max Power Draw (in W)	1,632.90	1,251.00
Endurance at Full Throttle (in s)	96	110
Max RPM	7,946	7,296
Max Current Draw (in A)	85.16	72.44
Max Thrust (in lbf)	15.80	13.20

Very clearly, the 18x8 carbon fibre propeller outperforms the other propellers. It is also way lighter than the other propellers. Moreover, the endurance of the 18x8 carbon fibre propeller is much higher than the others, which gives a relative measure of the efficiency of the propellers. Hence, due to its light weight, high efficiency, and high thrust-to-current rating, the carbon fibre propeller is an ideal choice for the propulsion system for all missions.

**Table 8.2:** Propeller Performance Comparison

S. No	Propeller	Weight (in oz)	Max Thrust (in lbf)	Max Endurance (in s)	Max Power Draw (in W)	Battery Heating Level
1	18x8 Carbon Fiber	1.06	13.20	110	1251.00	Low
2	18x8 Wood	3.03	13.22	84	1259.50	Moderate
3	18x10 Wood	2.61	13.88	72	1285.00	Very High
4	17x10 APC	2.47	11.56	80	1296.00	High
5	18x8 APC	3.07	13.84	70	1364.50	Very High
6	18x10 APC	3.10	14.39	63	1402.50	Very High

#### 8.4 Structural Testing

The structure maintained consistent elastic behavior throughout the loading sequence, with no observable permanent deformation, joint separation, or localized failure. The fiberglass-reinforced wing-fuselage interface effectively redistributed stresses and improved joint stiffness, performing reliably under the full 14 lb test load. Overall, the test results validate the robustness of the load path and provide strong confidence in the aircraft's structural integrity for sustained operational use.

**Table 8.3:** Mass Comparison

Subsystem	CAD Estimated Mass (lb)	Actual Mass (lb)
Fuselage	3.34	1.98
Wing	1.4	1.28
Vertical Stabiliser	0.12	0.18
Horizontal Stabilizer	0.29	0.39
Nacelle	0.15	0.2
Landing Gear	1.25	0.43
Wheel	0.17	0.17
Wheel Pant	0.09	0.09
<b>Total Mass</b>	<b>6.81</b>	<b>4.72</b>

**Figure 8.7:** Full Structural Assembly

## 9. Bibliography

- [1] IEEE: [2] S. J. Miley and S. M. Higgins, "Aerodynamic drag of streamers and flags," Dept. of Aerospace Engineering, Texas A&M Univ., College Station, TX, Rep., 1984
- [2] Drela, M., and Youngren, H., *Athena Vortex Lattice (AVL)*, Version 3.40, Massachusetts Institute of Technology, Cambridge, MA.
- [3] Dehausse, A., *XFLR5*, Version [6.61], retrieved [23 Nov. 2025], 2026. <https://www.xflr5.tech>
- [4] AIAA DBF Organizing Committee, "2025-26 Design, Build, Fly Rules," American Institute of Aeronautics and Astronautics, Reston, VA, 2025.
- [5] Mark Drela, QPROP, 1.22, Cambridge, MA, 2007.
- [6] Glauert, H., "The Airscrew: Momentum Theory," *The Elements of Aerofoil and Airscrew Theory*, 1st ed., Cambridge University Press, Cambridge, UK, 1926, pp. 199-207.
- [7] Capable Computing, Inc., MotoCalc, 8.09, Kitchener, ON, Canada, 2021.
- [8] Roskam, J., *Airplane Design, Part II: Preliminary Configuration Design and Integration of the Propulsion System*, DARcorporation, Lawrence, KS, 1997, Chap. 8, "Class I Method for Empennage Sizing and Disposition and for Control Surface Sizing and Disposition," pp. 187–212.
- [9] Roskam, J., *Airplane Design, Part VI: Preliminary Calculation of Aerodynamic, Thrust and Power Characteristics*, DARcorporation, Lawrence, KS, 2004, Chaps. 3–4 and Sec. 10.4, pp. 13–49, 463–485.
- [10] ANSYS Inc., *ANSYS Workbench*, 2023 R2, Canonsburg, PA, 2023.  
ANSYS Inc., *ANSYS Workbench*, 2024 R1, Canonsburg, PA, 2024.
- [11] Sóbester, A., *Aircraft Design Recipes in Python (ADRpy)*, Version 0.2.6, GitHub Repository, <https://github.com/sobester/ADRpy>
- [12] Forest Products Laboratory, "Wood Handbook: Wood as an Engineering Material," General Technical Report FPL GTR-282, U.S. Department of Agriculture, Forest Service, Madison, WI, 2021.
- [13] Federal Aviation Administration, "Acceptable Methods, Techniques, and Practices - Aircraft Alterations," Advisory Circular 43.13-2B, Washington, D.C., 2008.
- [14] ACP Composites, Inc., "Mechanical Properties of Carbon Fibre Composite Materials," Livermore, CA, 2025
- [15] Pamadi, B. N., *Performance, Stability, Dynamics, and Control of Airplanes*, American Institute of Aeronautics and Astronautics, Reston, VA, 1998, Chap. 2, "Aircraft Performance," pp. 67–164.
- [16] IEEE: [1] S. F. Hoerner, Fluid-dynamic drag: Practical information on aerodynamic drag and hydrodynamic resistance. Midland Park, NJ: Hoerner Fluid Dynamics, 1965
- [17] The MathWorks Inc., *MATLAB*, R2025b, Natick, MA, 2025.
- [18] Autodesk Inc., *Fusion*, San Francisco, CA, 2025.
- [19] PTC Inc., *Onshape*, Boston, MA, 2025.
- [20] eCalc, eCalc.ch, Switzerland, retrieved Jan 06, 2025. <https://www.ecalc.ch>
- [21] Niță, M., and Scholz, D. , "Estimating the Oswald Factor from Basic Aircraft Geometrical Parameters," Deutscher Luft- und Raumfahrtkongress 2012 , DocumentID: 281424, 2012. [https://www.fzt.haw-hamburg.de/pers/Scholz/OPerA/OPerA\\_PUB\\_DLRK\\_12-09-10.pdf](https://www.fzt.haw-hamburg.de/pers/Scholz/OPerA/OPerA_PUB_DLRK_12-09-10.pdf)
- [22] Lennon, A., "Basics of R/C Model Aircraft Design: Practical Techniques for Building Better Models, Model Airplane News," Air Age Publishing, Ridgefield, CT, 1996, pp..
- [23] Sadraey, M. H., "Aircraft Design: A Systems Engineering Approach," 1st ed., Wiley, Hoboken, NJ, 2012  
Güzelbey, İ. H., Eraslan, Y., and Doğru, M. H., "Numerical Investigation of Different Airfoils at Low Reynolds Number in Terms of Aerodynamic Performance of Sailplanes by Using XFLR5," Karadeniz Fen Bilimleri Dergisi, Vol. 8, No. 1, 2018, pp. 47–65. <https://doi.org/10.31466/kfbd.423932>.
- [24] Massachusetts Institute of Technology, "11.7 Performance of Propellers," Thermodynamics and Propulsion Course Notes. <https://web.mit.edu/16.unified/www/FALL/thermodynamics/notes/node86.html>